Reconstructing Magnetic Fields of Spiral Galaxies from Radiopolarimetric Observations

Universiteit Leiden
The Netherlands

ISBN: 978-94-6259-819-5
Printed by Ipskamp Drukkers

Cover graphic design by Bertram Zantinge.
Cover concept by author.

Front Cover: Molen De Put, Leiden, front-side. M51 appears in the background sky with its radio image in polarized intensity projected on the water's surface.
Original optical image of M51 is from the Hubble Space Telescope with additional processing by Robert Gendler. The polarized intensity radio image is from Fletcher et al. (2011) and the Atlas of Galaxies (MPIfR, Bonn).
Back Cover: Molen De Put, Leiden, back-side, with an inset scene from Museum De Lakenhal, Leiden. NGC 6946 appears in the background sky.
Original image of NGC 6946 is from the Subaru Telescope (NAOJ) and Robert Gendler with additional processing by Robert Gendler.

Reconstructing Magnetic Fields of Spiral Galaxies from Radiopolarimetric Observations

Proefschrift

ter verkrijging van
de graad van Doctor aan de Universiteit Leiden,
op gezag van de Rector Magnificus prof. mr. C. J. J. M Stolker,
volgens besluit van het College voor Promoties
te verdedigen op donderdag 17 december 2015
klokke 15:00 uur

door

Carl Shneider

geboren te Brooklyn, New York, USA
in februari 1984

Promotiecommissie

Promotor:	Prof. dr. H. J. A. Röttgering	
Co-promotor:	Dr. M. Haverkorn	Radboud Universiteit Nijmegen
Overige leden:	Prof. dr. H. Falcke	Radboud Universiteit Nijmegen
	Dr. M. R. Hogerheijde	
	Prof. dr. K. Otmianowska-Mazur	Jagiellonian University, Poland
	Prof. dr. P. van der Werf	

"Ideals are like stars; you will not succeed in touching them with your hands. But like the seafaring man on the desert of waters, you choose them as your guides, and following them you will reach your destiny."

— Carl Schurz

Table of Contents

1 Introduction **11**

1.1 Prelude . . . 11
1.2 The interactive ISM . . . 12
1.2.1 Turbulent energy spectrum . . . 14
1.3 Magnetic field classification . . . 16
1.4 Synchrotron radiation . . . 16
1.4.1 Radio observables . . . 17
1.4.2 Polarization . . . 19
1.5 Current status of magnetic field knowledge in spiral galaxies . . . 20
1.5.1 Spiral galaxies seen face-on . . . 21
1.5.2 Spiral galaxies seen edge-on . . . 22
1.6 This thesis . . . 23

2 Power spectra of synchrotron radio observables with Faraday effects and turbulent magnetic field **29**

2.1 Introduction . . . 30
2.2 Model description . . . 32
2.2.1 Random magnetic field . . . 33
2.2.2 Correlation method . . . 34
2.2.3 Stokes parameters . . . 35
2.2.4 Angular power spectrum . . . 36
2.3 Results . . . 36
2.3.1 Dependence on magnetic field spectral index . . . 41
2.3.2 Dependence on other input parameters . . . 43
2.4 Discussion . . . 44
2.5 Summary and conclusions . . . 45

3 Depolarization of synchrotron radiation in a multilayer magneto-ionic medium **49**
3.1 Introduction . . . 50
3.2 Method . . . 52
3.2.1 Regular, isotropic turblent, and anisotropic turbulent . . . 52
3.2.2 Projection from galaxy-plane to sky-plane coordinates . . . 53
3.3 The complex polarization . . . 54
3.4 Wavelength-independent depolarization . . . 57
3.5 Wavelength-dependent depolarization . . . 58
3.5.1 Differential Faraday rotation . . . 58
3.5.2 Internal Faraday dispersion . . . 59
3.5.3 External Faraday dispersion . . . 60
3.5.4 Depolarization from DFR with IFD . . . 61
3.6 Modeling example: application to M51 . . . 62
3.6.1 Generalized opaque-layer approximation . . . 67
3.7 Discussion and conclusions . . . 70

3.A Derivation of wavelength-independent depolarization equations for standard and equipartition scalings of emissivity . . . 72
3.B Symmetries and equation properties . . . 75
3.C General expression for wavelength-dependent depolarization for a three-layer system . . . 76

4 Constraining regular and turbulent magnetic field strengths in M51 via Faraday depolarization **79**
4.1 Introduction . . . 80
4.2 Observational data . . . 81
4.3 Model . . . 81
4.3.1 Regular field . . . 81
4.3.2 Turbulent field . . . 82
4.3.3 Densities . . . 84
4.3.4 Depolarization . . . 84
4.4 Procedure . . . 86
4.5 Results . . . 89
4.5.1 Two-layer model . . . 89
4.5.2 Three-layer model . . . 92
4.5.3 Robustness of results . . . 94
4.6 Discussion . . . 95
4.7 Conclusion . . . 97

5 A 3D magnetic field model for NGC 6946 **101**
5.1 Introduction . . . 102
5.2 Observational data . . . 104
5.3 Model . . . 105

5.3.1 Magnetic field . . . 105
5.3.2 Densities . . . 107
5.3.3 Stokes parameters . . . 109
5.3.4 Simulated Volume . . . 109
5.4 Method . . . 110
5.4.1 Goodness of fit . . . 112
5.5 Results . . . 113
5.5.1 Sensitivity to input parameters . . . 114
5.6 Discussion . . . 114
5.7 Summary and conclusions . . . 118
5.8 Future work . . . 119

Nederlandse Samenvatting **123**

English Summary **129**

Acknowledgements **135**

About the Author **141**

1

Introduction

> "The argument in the past has frequently been a process of elimination: one observed certain phenomena, and one investigated what part of the phenomena could be explained; then the unexplained part was taken to show the effects of the magnetic field. It is clear in this case that, the larger one's ignorance, the stronger the magnetic field."
>
> — Lodewijk Woltjer, Remarks[1] on the Galactic Magnetic Field, 1967.

1.1 Prelude

Galactic magnetic fields have come a long way; from being avoided for their complexity or naively invoked to explain cosmic phenomena, they are now established as a major and ubiquitous constituent of galaxies and form part of the broader, rapidly expanding field of Cosmic Magnetism. In fact, in the fast approaching era of 'mega-telescopes', ***magnetism*** is explicitly named as key science for the current LOw Frequency ARray (LOFAR) and future Square Kilometre Array (SKA) radio telescopes. It is Radio Astronomy that reveals the nature of magnetic fields in the cosmos as most of the tracers of cosmic magnetism lie in the radio domain. For example, the already operational Karl G. Jansky Very Large Array (VLA), LOFAR, and Atacama Large Millimeter/submillimeter Array (ALMA) are all able to provide detailed characterization of magnetic fields. The SKA with its two precursors, the Australian Square Kilometre Array Pathfinder (ASKAP) and the Meer ('more of') Karoo Array Telescope (MeerKAT), will provide unprecedented sensitivity and resolution, thereby revolutionizing the study of magnetic fields not only in our own

[1] Proceedings from IAU Symposium no. 31 held in Noordwijk, Netherlands.

Galaxy but also in external galaxies, the intracluster medium (ICM), and the intergalactic medium (IGM).

Although magnetic fields do not sculpt the dynamics of galaxies on the whole, they carry significant energy, not only in galaxy disks but also in galaxy halos (Haverkorn & Heesen 2012), and exert influence on virtually all astrophysical processes in the interstellar medium (ISM) (Ferrière 2001; Landecker 2012; Haverkorn 2014) and, consequently, influence galactic evolution.

Detailed knowledge of galactic magnetic fields is beneficial for ISM and star formation studies, as a significant foreground for studies of the Cosmic Microwave Background (CMB) B-mode polarization, the Epoch of Reionization (EoR), and magnetization of the cosmic web, and for tracing the arrival directions of Ultra high energy Cosmic Rays (UHECRs).

In the next section, the key constituent interactions in the ISM are presented and discussed. This is followed by a discussion of the energy spectrum of turbulence and the classification of magnetic fields according to field types. The synchrotron radiation mechanism is subsequently discussed followed by radio observables and polarization. Finally the current status of magnetic field knowledge is addressed, including the inferred dominant magnetic field modes in galaxy disks and halos, and the contribution of this thesis to galactic magnetism is summarized.

1.2 The interactive ISM

The ISM is broadly composed of gas, magnetic fields, cosmic rays (CRs), and dust. The gaseous phase of the ISM is classically composed of four phases, either ionized or neutral (for a review see Ferrière (2001)). The neutral phases are the Cold and Warm Neutral Media (CNM and WNM) and consist of atoms (predominantly hydrogen and helium with traces of metals) and molecules. The ionized phases are the Warm and Hot Ionized Media (WIM and HIM). In this thesis, the WIM is the relevant gas phase; ionized gas at a temperature of $\sim$ 8000 K and density 0.1 cm^{-3} (Tielens 2005), volume filling factor of $f_{\rm V}$ $\sim$ 20% and mass filling factor of $f_{\rm m}$ $\sim$ 10%. The WIM is very inhomogeneous and almost fully ionized ($\sim$ 0.9). Ionizing photons from O stars are the main source of ionization of the WIM. There are low-density channels that enable these ionizing photons from the O stars in the stellar disk to travel from the disk to far above the galactic mid-plane. This results in a large scale height of the WIM of about 1 kpc. The ionized gas is tightly coupled to the magnetic field and motions of the plasma can function to regenerate the large-scale magnetic field, converting kinetic energy into magnetic energy. Such a mechanism is known as a dynamo.

CRs are comprised of relativistic electrons (CREs), protons, and atomic nuclei, which have a power-law energy spectrum ranging from (at least) 10^{10} eV to $\sim 10^{20}$ eV. A slight break in the spectral slope occurs at about $10^{17.5}$ eV, thought to coincide with a transition from lower-energy Galactic CRs to higher-energy extragalactic CRs. These high-energy CRs can not be of Galactic origin since their Larmor radius exceeds the thickness of the Galaxy disk which allows them to immediately escape from the Milky Way. CREs

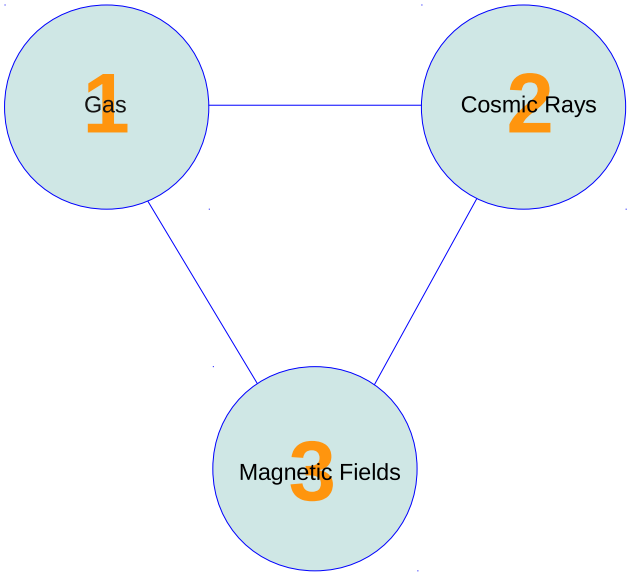

Figure 1.1: The ISM network described by gas, cosmic rays, and magnetic fields. The connecting edges denote bidirectional interaction.

spiraling around Galactic magnetic field lines emit synchrotron radiation detectable in the radio regime. In this way, CRs diffuse through the ISM with a diffusion coefficient given as the ratio of the mean-free path traveled by a CRE from its origin in the plasma to its synchrotron lifetime.

In the ISM, the energy densities of the turbulent gas, thermal gas, magnetic field and cosmic ray electrons are all on the order of ≈ 1 eV cm^{-3} (Hennebelle & Falgarone 2012), implying that all these processes are dynamically important and provide significant feedback on each other. We now provide examples of the feedback functionality of these three components as it operates in the ISM, shown schematically in Fig. 1.1.

1 → 2:
CRs are accelerated in astrophysical shocks found in objects such as supernova remnants (SNRs) through Fermi acceleration as proposed by E. Fermi in 1949. Acceleration continues as long the magnetic field is able to contain the CRs within the shocked region.

1 → 3:
At the same time, turbulent motions also amplify and distort magnetic fields and enhance magnetic diffusion. Plasma motions on a sufficiently large scale actuate the $\alpha - \omega$ (alpha-omega) dynamo (Parker 1955). The weight of the ordinary matter serves to confine the magnetic fields.

2 → 1:
CRs heat dense interstellar clouds that are too dense for photons to penetrate. They also drive galactic winds (Breitschwerdt et al. 1991, 1993). Also, the interaction of CRs with interstellar gas and dust produces gamma rays.

2 → 3:
CR driven dynamo (Parker 1992; Hanasz et al. 2004; Kulpa-Dybeł et al. 2015) and CR pressure inflates buoyant loops of magnetic fields via the Parker instability (magnetic buoyancy instability) (Parker 1966).

3 → 1:
Magnetic fields affect charged particles via the Lorentz force and can accelerate charged particles to high energies. They couple with both charged and neutral particles, via ion-neutral collisions, except for the densest parts of molecular clouds (Ferrière 2001), participate in gas dynamics, regulate cloud collapse and the subsequent onset of star formation, and affect motions of supernova remnants and bubbles (e.g., see Wolleben et al. (2010); Iacobelli et al. (2013)).

3 → 2:
Magnetic fields regulate the energy and distribution of CR; they affect CR diffusion length and diffusion time scales (Beck 2004). The diffusion coefficient varies with magnetic field strength and the field's degree of ordering. For example, Mulcahy et al. (2014) suggest that the CRE diffusion coefficient in M51 could be lower than in the Milky as a result of M51 having a stronger and possibly more turbulent magnetic field. Moreover, magnetic fields both decelerate CR, causing energy loss through emission of synchrotron radiation and accelerate CR via the mechanism of Fermi acceleration.

1.2.1 Turbulent energy spectrum

Turbulence is a property of a random, (fluid) flow characterized by spectral energy transfer that proceeds through non-linear, multi-scale interactions. In fact, from the electron density power spectrum of the WIM, turbulence in the WIM spans at least 10 decades of scale from 10^{-3} AU $\lesssim l \lesssim$ 100 pc (Armstrong et al. 1995).

The magnetized, multi-phase ISM is randomly stirred on the largest scales, most vigorously by old SNRs in the disk and by superbubbles and Parker instability in the halo, as shown by Mao et al. (2015) for M51. SNe input 10^{51} ergs (10^{44} J) per event resulting in an expanding SNR. After $\approx$ 1 Myr, the SNR's expansion speed has reduced to the ISM sound speed of $c_s \approx 10$ km s^{-1}, the size of the SNR has reached 50 – 100 pc at pressure balance, and SN shell merger with the ISM has commenced.

Although a gross simplification of the actual turbulence in the ISM, which requires a detailed description of the astrophysical plasma, magnetohydrodynamics (MHD) can be used as a clean dynamical theory to treat non-relativistic and slowly varying motions

(on time scales much longer than the inverse of the plasma frequency) of the highly-conducting plasma. This plasma is assumed to be subject only to the action of mechanical and magnetic forces. As magnetic fields are stretched and bent by the turbulent motions in the ISM, they resist deformation via magnetic tension. Thus, from the combined action of the turbulent advection of the magnetic field and the field's back reaction, a statistically steady state of (incompressible) MHD turbulence can be assumed to arise which is then characterized by a power-law energy spectrum (Schekochihin & Cowley 2007).

Three main regimes for this energy-spectrum hold:

1. Integral scale: The driving force of turbulence injects energy and momentum into the largest eddies (cells) comparable to the object size. Turbulent motions decay at the turnover time of the largest eddy.

2. Inertial range: An energy cascade ensues, subject to inertial forces, with energy progressively removed from larger eddies (small k) and deposited at small eddies (large k) where k is the wavenumber ($2\pi/l$). Kinetic energy is conserved (does not dissipate). The energy transfer rate proceeds independently of k, with the eddies unaware of either the driving force or of dissipation. There is thus a power law dependence of $E(k)$ on k which translates to a linear relationship in $\log E(k)$ vs $\log k$.

3. Dissipation scale: Energy is transferred to heat by viscous forces, marking the end of the inertial range.

As proof of the necessity for dynamo action in the ISM, we briefly consider the fundamental MHD equation which describes the time evolution of the magnetic field as

$$\frac{\partial \mathbf{B}}{\partial t} = \nabla \times (\mathbf{v} \times \mathbf{B}) + \eta \nabla^2 \mathbf{B}, \tag{1.1}$$

where $\mathbf{B} = \overline{\mathbf{B}}$ is the total magnetic field set equal to the large-scale field (having assumed the absence of a turbulent magnetic field), $\mathbf{v}$ is the mean velocity, and where η is a constant *Ohmic* magnetic diffusivity depending only on the temperature of the plasma. Moreover, $\eta \propto \sigma^{-1}$, where σ is the electric conductivity. First, consider the idealized case of infinite conductivity, with $\eta = 0$ in the above equation. This yields the so-called ideal MHD equation. The ideal MHD equation describes the 'frozen-in' limit of Eq. (1.1) as a result of magnetic fields moving perfectly with the fluid[2]. As an order of magnitude estimation, the ideal MHD equation can be rewritten as $\tau \approx l/v$ for some characteristic time τ, length l, and velocity v. For $l \sim 100$ pc and velocity equal to c_s, the ideal MHD limit then implies that it would take $\tau \approx 10$ Myr for turbulence to develop in the ISM. Next, without loss of generality, let us assume that the ISM is a static plasma ($\mathbf{v} = 0$) so that only the second term on the right hand side of Eq. (1.1) remains. Thus, we have that $\tau_{\rm diff} \approx l_{\rm diff}^2/\eta$ with a characteristic diffusion time $\tau_{\rm diff}$ and diffusion scale $l_{\rm diff}$. Assuming that charge

[2]Described by Alfvén in 1942 and therefore known as Alfvén's theorem of flux freezing.

Table 1.1: Nomenclature used to describe the three magnetic field types along with a physical basis for these respective fields.

Field type	Regularity	Degree of ordering	Scale	Example causes
Mean, average $\overline{\mathbf{B}}$	regular, uniform	coherent (ordered)	large-scale, global	dynamo action
Anisotropic $\mathbf{b}_{\mathrm{A}}$	random, turbulent, tangled	ordered	small-scale	compression or shear
Isotropic $\mathbf{b}_{\mathrm{I}}$	random, turbulent, tangled	disordered	small-scale	supernovae

separation in the plasma is negligible and that ions and electrons both have a temperature of 10^4 K, yields $\eta \approx 10^7$ cm^2 s^{-1}. Now, with $l_{\mathrm{diff}} \approx 500$ pc for a galactic disk thickness, $\tau_{\mathrm{diff}} \approx 10^{27}$ yr, a time much longer than the age of the universe of 13.7 Gyr. In the real ISM, however, the diffusivity is strongly affected by the turbulent motions of the plasma resulting in the η in Eq. (1.1) being replaced by an isotropic *turbulent* magnetic diffusivity given by $\eta_{\mathrm{turb}} = {}^1\!/_3\, l_{\mathrm{diff}}\, c_s \approx 10^{26}$ cm^2 s^{-1}. This yields a large-scale magnetic field decay time of $\tau_{\mathrm{diff}} \approx 5 \times 10^8$ yr or about ${}^1\!/_{20}$ of the galactic lifetime. Since magnetic fields are indeed observed in galaxies, this, in turn, necessitates dynamo action in the ISM.

1.3 Magnetic field classification

Magnetic fields can be classified according to three distinct field types as described in Table 1.1 and illustrated in Fig. 1.2. Mean or regular fields have sizes of the spiral arms and arise from large-scale motions of the plasma (e.g., differential rotation as part of a dynamo), that drag the essentially 'frozen-in' field lines along. Isotropic turbulent fields, on the other hand, have directions which are completely random. These are fields tangled by supernovae and other outflows such as stellar winds and protostellar outflows. When isotropic turbulent magnetic fields are compressed or sheared by gas flows, they obtain a preferred overall orientation, but with directions remaining frequently reversed on small scales. The circular turbulent cells of the isotropic turbulent field in Fig. 1.2 indicate that the field equally correlates with all spatial directions while the elliptical turbulent cells of the anisotropic turbulent field reflect a stronger spatial correlation along a particular direction.

1.4 Synchrotron radiation

Synchrotron radiation is one of the best tracers of the magnetic field because it is produced throughout the galaxy on account of the Lorentz force. Synchrotron radiation that arises from relativistic cosmic ray electrons is highly linearly polarized, non-thermal continuum emission with flux at cm and m (radio) wavelengths. The ensemble of gyrating cosmic ray electrons in the plasma is assumed to have an isotropic velocity distribution and to

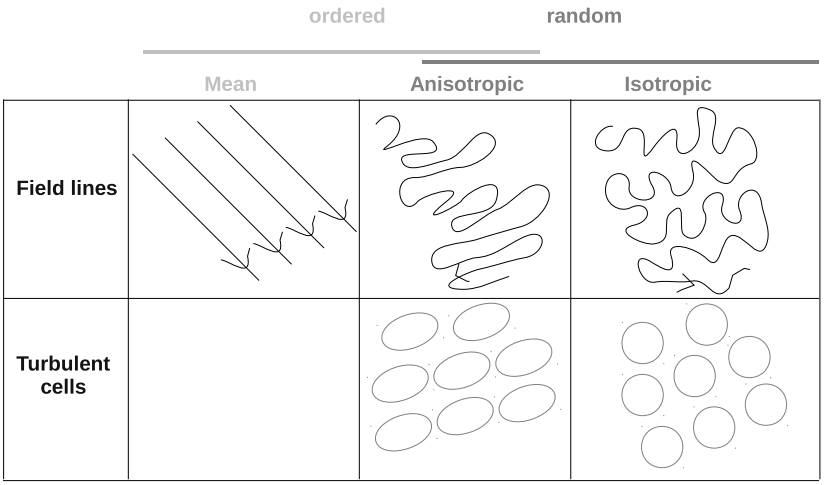

Figure 1.2: Illustrations of field lines and turbulent cells corresponding to the three magnetic field types.

follow a power law energy distribution within a prescribed energy interval. The intensity of synchrotron emission is a measure of the number density of cosmic ray electrons (in the relevant energy range) and of the strength of the total magnetic field in the plane of the sky[3] as illustrated in Fig. 1.3. Furthermore, Fig. 1.3 shows that the signal detected by the radio telescope at a particular wavelength comes from the polarized electric field which serves as a measure of the strength of $B_\perp$. The intrinsic polarization angle is, therefore, perpendicular to the local magnetic field orientation in the sky plane with the electromagnetic wave oscillating along the plane of the E-vector while propagating along $B_\parallel$. Consequently, to indicate the orientation of the headless B-vectors of polarized emission in polarized radio emission maps, the polarization angle of the polarized electric field is rotated by 90°.

1.4.1 Radio observables

Information on magnetic fields, thermal electron density distribution, and cosmic ray electron density distribution is encoded in radio observables. The total synchrotron intensity (Stokes I) is the total synchrotron radiation energy emitted per unit time from the volume enclosed by the telescope beam cylinder. Stokes Q and Stokes U and the polarized intensity (P), with $P = \sqrt{Q^2 + U^2}$, are observables that describe the polarization of the synchrotron radiation. As an example, Fig. 1.4 shows I and P radio synchrotron maps of M51 along with an optical image indicating the B-vectors of polarized emission. To explicitly show how these observables are affected by Faraday rotation it is handy to con-

[3]This is to say that the perpendicular ($B_\perp$) and parallel ($B_\parallel$) to the line-of-sight components of the total magnetic field lie in the sky plane.

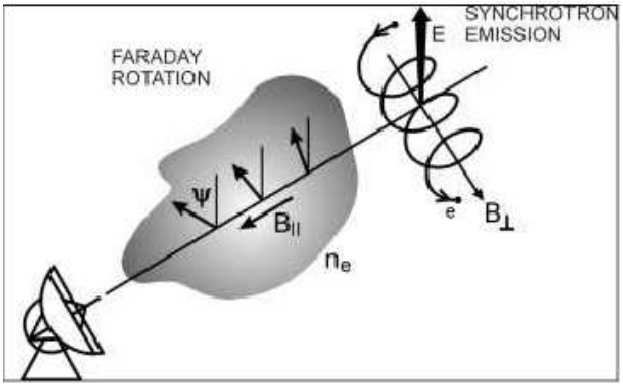

Figure 1.3: Synchrotron emission and Faraday rotation, reproduced from Beck & Wielebinski (2013).

sider the expression for the complex linear polarization of synchrotron emission ($\mathcal{P}$) given by

$$\mathcal{P} = p \exp(2\,\mathrm{i}\,\Psi),$$

where $p = P/I$ is the polarization fraction and Ψ is the observed polarization angle. Faraday rotation causes the intrinsic polarization angle Ψ_0 to rotate along the line of sight as a function of observing wavelength λ as

$$\Psi = \Psi_0 + \mathrm{RM}\,\lambda^2. \tag{1.2}$$

The rotation measure (RM) is given by

$$\left(\frac{RM}{\mathrm{rad\ m^{-2}}}\right) = 0.81 \int_{source}^{\mathrm{telescope}} \left(\frac{n_\mathrm{e}}{\mathrm{cm^{-3}}}\right)\left(\frac{\overline{B}_\parallel + b_\parallel}{\mu\mathrm{G}}\right)\left(\frac{dl}{\mathrm{pc}}\right),$$

where n_e is the thermal electron density, $\overline{B}_\parallel$ is the parallel component of the regular field along the line of sight, $b_\parallel$ is the parallel component of the turbulent field along the line of sight, and dl is an incremental distance along the line of sight from the synchrotron source to the telescope.

With the assumptions pertaining to cosmic ray electrons in Section 1.4, the maximum intrinsic polarization degree p_0 only depends on the spectral index (γ) of the cosmic ray electrons as (Le Roux 1961)

$$p_0 = \frac{\gamma + 1}{\gamma + 7/3}.$$

For typical values of the spectral index γ for spiral galaxies, $p_0 \approx 73\% - 75\%$. However, the actual observed degree of polarization is much lower due to depolarization.

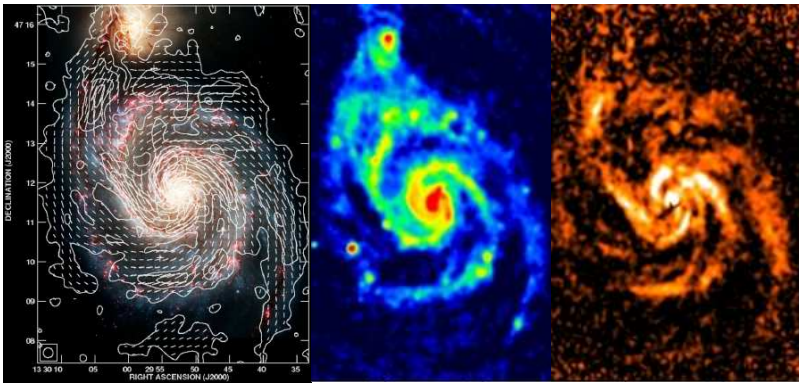

Figure 1.4: All three panels show M51. (Left) Polarized intensity (P) contours are overlaid on a Hubble Space Telescope optical image. Also featured are headless B-vectors of polarized emission with magnitude proportional to the polarized intensity. The polarized radio emission is observed at λ 6.2 cm with 15″ resolution using the VLA and Effelsberg radio telescopes. (Center) Total intensity (I) at λ 6.2 cm at a 8″ resolution. The color scale is in mJy/beam with red indicating higher flux densities per synthesized beam. (Right) Polarized intensity observed at the same wavelength and resolution as the total intensity but now with white indicating higher flux density. All three panels adopted from Fletcher et al. (2011) and the Atlas of Galaxies (MPIfR Bonn) available at http://www.mpifr-bonn.mpg.de.

1.4.2 Polarization

We consider how the distinct magnetic field types, discussed in the preceding section, affect the observed polarization. A starting scenario is to assume a magnetized medium that is devoid of thermal electrons. The variation in intrinsic polarization angle along the line of sight only occurs when a turbulent magnetic field is present as shown by Fig. 1.5. The variation is strongest for a purely isotropic random field and decreases when a regular field is added to this random field as the regular field serves to bring about more order as also shown by Fig. 1.5. As a consequence of the cumulative addition of polarization vectors along the line of sight, a purely mean field preserves the original polarization (no depolarization) while an isotropic random field basically destroys all polarization (complete depolarization). An anisotropic field yields polarization between these two extremes. This is a wavelength-independent depolarization effect as the intrinsic polarization angle is an intrinsic property of the magnetic field configuration.

We now consider thermal electrons in addition to the cosmic ray electrons in the magneto-ionic medium. Now, instead of only having emission along the line of sight, thermal electrons Faraday rotate the E-vector of polarized emission as shown in Fig. 1.3. Consequently, this Faraday rotation gives the strength of $B_{\parallel}$, if the thermal electron density distribution along the line of sight is known, and the direction of $B_{\perp}$. This is a wavelength-dependent effect which increases at longer observing wavelengths.

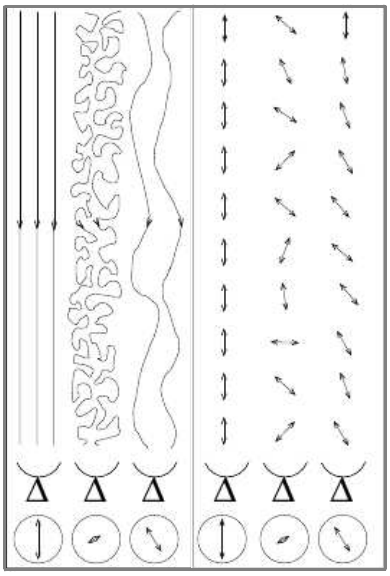

Figure 1.5: Polarization from the different magnetic field types, reproduced from Haverkorn, M. (2002). The three different lines of sight in the left hand panel describe situations with a regular field, an isotropic random field, and a combination of a regular and isotropic random field, respectively. The double-arrowed lines in the right hand panel represent the polarization vector at points along these lines of sight. The two groups of schematics at the bottom of each of the two panels represent the radio telescope and the resulting strength and direction of the measured polarization along the whole line of sight.

1.5 Current status of magnetic field knowledge in spiral galaxies

Our vantage point from within the Milky Way disk, near the Galactic mid-plane[4], allows for the study of magnetic fields in discrete objects on parsec (pc) and sub-parsec scales as well as large-scale field reversals along the Galactic radius. In the Galactic disk, the outer scale of fluctuations has a scale of $\lesssim$ 10 pc in the spiral arms and $\lesssim$ 100 pc in the interarm regions as measured from observations of *RM* by Haverkorn et al. (2008). However, the nature of the Galactic Center magnetic field (Ferrière 2009), the global azimuthal structure of the Galactic field (Men et al. 2008), and the number and locations of large-scale field reversals is still under debate (Haverkorn 2015). Observations of external (face-on) spiral galaxies provide 'zoomed-out' portraits of possible configurations for the Galactic magnetic field.

Magnetic fields in galaxies typically have micro-Gauss (μG) field strengths. The to-

[4]We are situated in the Orion-Cygnus arm and are currently at a height of 6 – 28 pc above the galactic plane (Joshi 2007).

tal magnetic field tends to be strongest in the inner few hundred parsecs of the galactic center region with an estimated range of field strengths from several tens of μG to as high as several milli-Gauss (mG). With the exception of starburst galaxies, whose nuclear starburst regions have some of the strongest total fields on account of intense star formation rates (SFRs) and SN rates (Beck 2009), high field strengths at the galactic center are thought to arise from a regular vertical field pervading the intercloud medium[5] (Ferrière 2011) as a result of dynamo action and/or from extreme turbulent activity in the galactic nucleus (Boldyrev & Yusef-Zadeh 2006). The concentration of molecular gas in a thin sheet parallel to the galactic plane, known as the central molecular zone (CMZ), may also compress regular magnetic fields to yield such high values, as is the case in the Milky Way. Assuming equipartition between magnetic field and cosmic ray energy densities, Niklas & Beck (1997) inferred an average total magnetic field strength of $9 \pm 3\,\mu$G for a sample of 74 spiral galaxies. Total magnetic field strengths of $10 - 15\,\mu$G are typical of 'grand-design' spiral galaxies with high SFRs such as M51 (Fletcher et al. 2011) and NGC 6946 (Beck 2007). The strength of the ordered magnetic fields in spiral galaxies are typically $1 - 5\,\mu$G but can be higher in grand-design spiral galaxies perhaps as a result of a more efficient galactic dynamo. In the spiral arms, the regular field is weaker and the turbulent field is stronger, probably due to star-forming processes and expansion of SNRs tangling the field (Beck 2001). Moreover, the strength of the ordered field (regular field plus anisotropic turbulent field) is at least five times weaker than the observed field strength of the isotropic turbulent field in the spiral arms (Beck & Wielebinski 2013). In between the spiral arms the regular field may be much stronger than the turbulent field and sometimes forms so called 'magnetic arms' as in NGC 6946 (Beck et al. 1996). In these interarm regions, the strength of the ordered field is about half to twice the strength of the disordered field (Beck & Wielebinski 2013). In general, the strength of the ordered field in the halo is comparable to the strength of the regular field in the disk (Krause 2014).

1.5.1 Spiral galaxies seen face-on

Observations of face-on spiral galaxies show a large-scale spiral field along the disk plane that is aligned with the spiral arms. The two most common magnetic field configurations observed are in fact the two lowest modes most easily excited by a galactic dynamo. These are the axisymmetric mode and the bisymmetric mode shown in Fig. 1.6. Higher modes may also be present but would have small amplitudes. Possible modes of magnetic fields in the halo are the symmetric, 'quadrupolar', or even-parity field and the anti-symmetric, 'dipolar', or odd-parity field as shown in Fig. 1.7. In the following, we refer to the vertical and horizontal magnetic field components as poloidal and toroidal, respectively. The symmetric field in the left-hand panel of Fig. 1.7 has a reversal in the direction of the poloidal component across the galactic plane and a toroidal component whose direction is the same above and below the plane. The anti-symmetric field in the right-hand panel of Fig. 1.7 has a poloidal component that runs through the galactic plane and a toroidal component that reverses directions above and below the plane. The actual mechanisms governing the

[5] Composed of the WNM, WIM, and HIM.

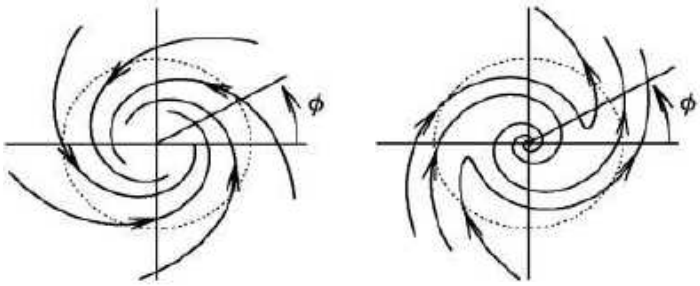

Figure 1.6: Illustration of axisymmetric and bisymmetric regular magnetic field configurations in the disk, respectively, reproduced from Widrow (2002).

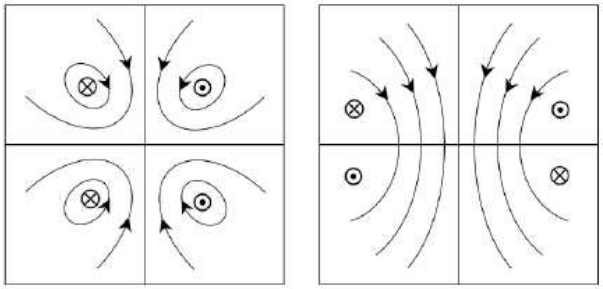

Figure 1.7: Illustration of symmetric and anti-symmetric regular magnetic field configurations in the halo reproduced from Haverkorn (2014).

structure of magnetic fields in galaxy halos still remains to be better understood.

Beck & Wielebinski (2013) provide a comprehensive compilation of magnetic field structure in both the disk and halo of spiral galaxies in their "catalog of radio polarization observations of nearby galaxies".

1.5.2 Spiral galaxies seen edge-on

In the Krause (2014) sample of 11 nearby edge-on galaxies of different Hubble type and covering a wide range in SFR, a disk-parallel field near the disk plane is observed which fans out from the disk at large vertical distances. Vertical field components that form an 'X-shape' pattern are observed in the halo. An outflow from the disk, such as a galactic wind, that transports the magnetic field from the disk to the halo may cause this morphology. A galactic dynamo may also be involved.

1.6 This thesis

In this thesis we reconstruct properties of magnetic fields in the disks and halos of spiral galaxies by means of the polarization of synchrotron radiation. Specifically, we use the polarization fraction as a diagnostic. The goal of this research project has been to infer the structure of the magnetic field across various angular scales in our own Galaxy (Chapter 2) and the strength and structure of the magnetic field in the disk and halo of external galaxies (Chapters 3 - 5) from the WIM phase of the ISM.

The main scientific objectives along with the areas to which this thesis has contributed to can be summarized as follows:

Chapter 2

Investigation of the spatial scales of polarization structures in terms of the energy distribution of the magnetic field in the Milky Way using statistical methods. The power spectra of diffuse synchrotron polarized intensity have been studied by a number of radio polarization surveys at various Galactic longitudes and latitudes, observing wavelengths, and angular scales (Haverkorn et al. 2003; Stutz et al. 2014). However, the interpretation of the values of these power spectra is complicated by the dependence of the radio observables on the magnetic field, outer scale of turbulence, thermal electron density distribution, cosmic ray electron density distribution, and path length.

Chapters 3 & 4

Development of methodology for describing the cumulative effects of various depolarization mechanisms and subsequent application of methodology to constrain magnetic field strengths in the spiral galaxy M51. Previous depolarization models have treated depolarization as arising solely from Faraday rotation. Furthermore, it has been customary to define RM by a simple linear relationship between polarization angle change with the square of the observing wavelength as $RM = d\Psi/d\lambda^2$ based on Eq. (1.2). However, if synchrotron emission and the Faraday-rotating medium are mixed or alternating along the line of sight, this simple linearity no longer holds. This probably applies to the majority of Faraday rotation measurements of the diffuse synchrotron emission in galaxies.

Chapter 5

Examination of a physically motivated 'X-shape' regular magnetic field model for constraining magnetic field strength and structure in the spiral galaxy NGC 6946. Traditionally, dipole and quadrupole magnetic fields have been used to model the magnetic field in the halo. The dipole and quadrupole magnetic fields are the second and third terms, respectively, representing the total magnetic field in a multipole expansion[6] in powers of inverse radial distance for a spherically symmetric

[6]The first term of the multipole expansion is zero as there are no magnetic monopoles.

object. This expansion assumes that the magnetic field can be represented as the gradient of a scalar magnetic potential resulting from having zero current. With zero current, there is no force to act on the magnetic field. Although the halo is an almost spherical rotating body, the galaxy encloses an interstellar plasma which enables cross-field electric currents to flow, making the magnetic field generally not force-free, and, thereby, causing departures from the pure dipole and quadrupole geometries. This necessitates consideration of more complex geometries.

In Chapter 2, statistically independent realizations of physical 3D random magnetic fields with prescribed power spectra are generated. The properties of this random field are assumed to reproduce some of the observed properties of turbulence in the ISM. The turbulence is assumed to be purely isotropic and representative of a high galactic latitude environment. These magnetic field 'cubes' are then used to simulate radio observables of Stokes I, Q, U, and polarized intensity P at several physically motivated observing wavelengths together with varying parameters of cosmic ray electron density, outer scale of fluctuations, and integrated path length. Subsequently, the angular power spectrum (APS) prescription of Haverkorn et al. (2003) is used to measure the statistical angular (auto)correlations for each of these resulting radio observables. The spectral indexes of the observables are α_I, α_Q, α_U, α_P, respectively. Two aspects in particular contribute to the novelty of our approach: (1) we use the recent method of Stepanov et al. (2014) to search for imprints of point-wise equipartition and pressure equilibrium between cosmic ray electrons and local magnetic field energy density on the power spectra of radio observables and (2) we simulate a realistic cone-like field of view with diverging sight lines as expected from radio sources that are at most only at a few kpc distance. We find that α_I traces the underlying magnetic field power spectrum but that it may not be possible to use α_I to identify the actual magnetic field power spectrum due to measurement uncertainties. We also find that α_Q, α_U, and α_P can not be used to determine the magnetic field power spectrum since a wide range of values arise from a single underlying magnetic field power spectrum on account of a degenerate dependence on the parameters described above. Furthermore, assumptions of equipartition/pressure equilibrium do not affect the polarization spectral indices but do have an effect on the amplitude of the power spectrum. An interesting further prediction of our model is that the power spectra of Q, U, and P may have a frequency dependent break whose angular scale depends on parameters of the turbulence and hence can be a useful diagnostic in establishing turbulence parameters. This is necessary to consider as a frequency dependent break has been traditionally interpreted in the literature as evidence for a non-singular turbulent power spectrum whereas in our models it arises from a single turbulent power spectrum. Moreover, flat or inverted power spectra at low frequencies ($\leq$ 200 MHz) are obtained which could be detected with LOFAR and MWA.

In Chapter 3, we develop an analytical framework for treating depolarization arising from the superposition of all three distinct magnetic field types occurring along the line of sight. We account for the combined action of wavelength-dependent and wavelength-independent synchrotron depolarization mechanisms in a face-on galaxy, modeled as a synchrotron-emitting and Faraday-rotating multilayer magneto-ionic medium.

In particular, we are able to probe the different depolarization effects of the two distinct types of turbulent magnetic field which was previously a black-box with previous approaches in the literature. Subsequently, as a proof-of-concept, a small-region case study is performed in the grand-design, face-on spiral galaxy M51. This allows for a direct statistical comparison with the observed polarization maps at the observing wavelengths. Seventeen distinct model types are constructed, comprised of all possible combinations of a regular, isotropic turbulent, and anisotropic turbulent magnetic fields in each of the disk and halo. Although we only had three observing wavelengths to work with, our approach was able to reduce the original pool of the 17 distinct model types to a smaller subset of models that all required the presence of turbulent magnetic fields in both the disk and the halo. Such models are a natural next step in complexity (Heald et al. 2014), indicative of the type of investigations that can be performed with large samples of galaxies observed with wideband, multichannel polarization capability such as with the upcoming SKA.

In Chapter 4, we apply the developed methodology to the entire M51 galaxy. We assess the robustness of our approach via a bootstrap technique. Assuming independence of magnetic field strengths on azimuth provides sufficient constraints to gauge the regular and turbulent magnetic strengths. We find that a model with all three field types in the disk and a regular plus isotropic turbulent field in the halo fits best to the data. Furthermore, the total magnetic field strength and the regular and turbulent magnetic field strengths in the disk are all several times higher than in the halo. Values of magnetic fields are in agreement with those previously inferred in the literature which gives confidence to our methodology. Moreover, our multilayer approach confirms the result from previous literature that the far-side of the halo is completely depolarized and does not contribute to depolarization.

In Chapter 5, we construct a so called 'X-shape' magnetic field, as a model for the regular field in the almost face-on spiral galaxy NGC 6946. This field is divergence-free by construction and, thus, physical. An X-shape magnetic field gives rise to an X-shape polarization pattern, typically observed in edge-on spiral galaxies, and is thought to be common in spiral galaxies. The global 3D magnetic field morphology of the best-fit model is explicitly shown along with this model's predicted average magnetic field strength which is consistent with earlier estimates in the literature. Our model requires additional complexity to fit the data well.

Bibliography

Armstrong, J. W., Rickett, B. J., & Spangler, S. R. 1995, ApJ, 443, 209

Beck, R. 2001, Space Sci. Rev., 99, 243

Beck, R. 2004, Ap&SS, 289, 293

Beck, R. 2007, A&A, 470, 539

Beck, R. 2009, Astrophysics and Space Sciences Transactions, 5, 43

Beck, R., Brandenburg, A., Moss, D., Shukurov, A., & Sokoloff, D. 1996, ARA&A, 34, 155

Beck, R. & Wielebinski, R. 2013, Magnetic Fields in Galaxies, ed. T. D. Oswalt & G. Gilmore, 641

Boldyrev, S. & Yusef-Zadeh, F. 2006, ApJ, 637, L101

Breitschwerdt, D., McKenzie, J. F., & Voelk, H. J. 1991, A&A, 245, 79

Breitschwerdt, D., McKenzie, J. F., & Voelk, H. J. 1993, A&A, 269, 54

Ferrière, K. 2009, A&A, 505, 1183

Ferrière, K. 2011, in IAU Symposium, Vol. 271, IAU Symposium, ed. N. H. Brummell, A. S. Brun, M. S. Miesch, & Y. Ponty, 170–178

Ferrière, K. M. 2001, Reviews of Modern Physics, 73, 1031

Fletcher, A., Beck, R., Shukurov, A., Berkhuijsen, E. M., & Horellou, C. 2011, MNRAS, 412, 2396

Hanasz, M., Kowal, G., Otmianowska-Mazur, K., & Lesch, H. 2004, ApJ, 605, L33

Haverkorn, M. 2014, ArXiv e-prints

Haverkorn, M. 2015, in Astrophysics and Space Science Library, Vol. 407, Astrophysics and Space Science Library, ed. A. Lazarian, E. M. de Gouveia Dal Pino, & C. Melioli, 483

Haverkorn, M., Brown, J. C., Gaensler, B. M., & McClure-Griffiths, N. M. 2008, ApJ, 680, 362

Haverkorn, M. & Heesen, V. 2012, Space Sci. Rev., 166, 133

Haverkorn, M., Katgert, P., & de Bruyn, A. G. 2003, A&A, 403, 1045

Haverkorn, M. 2002, PhD thesis, Leiden University, The Netherlands

Heald, G., Beck, R., de Blok, W. J. G., et al. 2014, in Proceedings of Advancing Astrophysics with the Square Kilometre Array (AASKA14). 9 -13 June, 2014. Giardini Naxos, Italy., 106

Hennebelle, P. & Falgarone, E. 2012, A&A Rev, 20, 55
Iacobelli, M., Haverkorn, M., & Katgert, P. 2013, A&A, 549, A56
Joshi, Y. C. 2007, MNRAS, 378, 768
Krause, M. 2014, ArXiv e-prints
Kulpa-Dybeł, K., Nowak, N., Otmianowska-Mazur, K., et al. 2015, A&A, 575, A93
Landecker, T. L. 2012, Space Sci. Rev., 166, 263
Le Roux, E. 1961, Annales d'Astrophysique, 24, 71
Mao, S. A., Zweibel, E., Fletcher, A., Ott, J., & Tabatabaei, F. 2015, ApJ, 800, 92
Men, H., Ferrière, K., & Han, J. L. 2008, A&A, 486, 819
Mulcahy, D. D., Horneffer, A., Beck, R., et al. 2014, A&A, 568, A74
Niklas, S. & Beck, R. 1997, A&A, 320, 54
Parker, E. N. 1955, ApJ, 122, 293
Parker, E. N. 1966, ApJ, 145, 811
Parker, E. N. 1992, ApJ, 401, 137
Schekochihin, A. A. & Cowley, S. C. 2007, Turbulence and Magnetic Fields in Astrophysical Plasmas, ed. S. Molokov, R. Moreau, & H. K. Moffatt (Springer), 85
Stepanov, R., Shukurov, A., Fletcher, A., et al. 2014, MNRAS, 437, 2201
Stutz, R. A., Rosolowsky, E. W., Kothes, R., & Landecker, T. L. 2014, ApJ, 787, 34
Tielens, A. G. G. M. 2005, The Physics and Chemistry of the Interstellar Medium
Widrow, L. M. 2002, Reviews of Modern Physics, 74, 775
Wolleben, M., Fletcher, A., Landecker, T. L., et al. 2010, ApJ, 724, L48

2

Power spectra of synchrotron radio observables with Faraday effects and turbulent magnetic field

C. Shneider, M. Haverkorn, A. Fletcher

Astronomy & Astrophysics, 2015
To be submitted

Abstract

We simulate a typical high Galactic latitude interstellar medium (ISM) environment with characteristic regular $B = 3\,\mu$G and turbulent $b = 6\,\mu$G magnetic field strengths and both thermal and cosmic ray electron densities. The solenoidal, random Gaussian magnetic field has a tunable spectral index α_b. We observe this synchrotron emitting and Faraday rotating magneto-ionic medium at a frequency of 350 MHz over a generic path length of 1 kpc with a realistic cone-like field of view which is integrated along the line of sight to yield Stokes I, Q, U, and P maps with power spectra over a multipole range of $150 \leq \ell \leq 1000$. A power spectrum analysis PS(ℓ) is performed on the resulting maps for physically motivated values of α_b. We find that

total synchrotron intensity is a good tracer of the spectral index of the turbulent magnetic field whereas spectral indices of polarized intensity and of the Stokes parameters cannot be used as these depend degenerately on many factors characterizing the medium. We find a frequency dependent break in the polarized intensity and Stokes parameters which occurs at smaller angular scales for lower frequencies.

2.1 Introduction

Efforts to characterize the turbulent magneto-ionic medium of our Galaxy from synchrotron radio emission and its linear polarization spanning centimeter to meter wavelengths, originate from the Wieringa et al. (1993) discovery of small scale structure in this emission at 325 MHz using the Westerbork Synthesis Radio telescope (WRST). The production of synchrotron radiation throughout the Galactic volume and its depolarization (Burn 1966; Sokoloff et al. 1998, 1999, and Chap. 3 of this thesis) by the intervening plasma - the interstellar medium (ISM) - along essentially every line of sight through the Galaxy, provides information on the spatial distribution of the thermal and cosmic ray electron densities and strength of Galactic magnetic fields. This information is also important for cosmic microwave background (CMB) polarization B-mode detection (Carretti et al. 2010), for high-resolution extragalactic observations with the SKA (Sun & Reich 2009), as well as epoch of reionization (EoR) studies (Jelić et al. 2008).

At wavelengths of just a few centimeters, the measured (diffuse) polarization directly traces the magnetic field in the emitting region because Faraday rotation is negligible whereas at longer wavelengths additional information on magnetic field structure and electron density along the entire line of sight is obtained. Faraday rotation refers to the rotation of the intrinsic polarization vector from its angle, on emission, by an amount proportional to the square of the observing wavelength. The proportionality constant is the rotation measure (*RM*)

$$RM = 0.81 \int_{\text{source}}^{\text{observer}} n_{\text{e}} \; (B_{\parallel} + b_{\parallel}) \; dl,$$

which is comprised of the thermal electron density n_{e} (cm^{-3}), the regular $B_{\parallel}$ and random $b_{\parallel}$ components of the magnetic field (μG) directed along the line of sight, and the path length (pc) through the ionized ISM. Owing to the presence of both regular and random Galactic magnetic field components in the disk and halo together with thermal and cosmic ray electrons, Faraday rotation causes depolarization by differential Faraday rotation (DFR) (also known as depth depolarization) and depolarization by Faraday dispersion (FD) (also referred to as beam depolarization).

Consequently, a subset of existing radio polarization surveys, ranging from several hundred MHz to a few GHz frequencies and covering many different parts of the sky at various spatial and angular scales, have been analyzed using power spectra (PS), angular power spectra (APS), and structure functions SFs in order to parametrize structure in radio maps of total synchrotron intensity I, Stokes parameters Q and U (or in CMB studies,

the E- and B- modes, respectively (Tucci et al. 2002)), and polarized intensity P. PS use a (planar) fast Fourier transform (FFT) on a Cartesian grid, APS use a spherical harmonic expansion on a spherical grid, and SFs are a measure of autocorrelation used to study random processes whose power spectra are given by a power law (Simonetti et al. 1984) and do not require a regular grid of data points as do both PS and APS (Haverkorn et al. 2003). Haverkorn et al. (2003) also studied both power spectra and structure functions of diffuse polarization in the Galaxy from *RM* maps. Most of these surveys focus on low Galactic latitudes although there is observational evidence for significant *RM* structure at high Galactic latitudes ($b \sim 71°$) at low frequencies (315−388 MHz) (de Bruyn et al. 2006) and possibly at high frequencies (1.4 GHz) from simulations of (Sun & Reich 2009). Significant magnetic field strengths are also present in the Galactic halo (Haverkorn & Heesen 2012). For a compilation and application of PS, APS, and SFs to these various surveys see Stutz et al. (2014, and refs. therein) and Haverkorn et al. (2003). Present surveys with the Low Frequency Array (LOFAR) such as the Multifrequency Snapshot Sky Survey (MSSS) (Heald & LOFAR Collaboration 2014), surveys by the Murchison Widefield Array (MWA) (Bowman et al. 2013), and future surveys such as by the Square Kilometre Array (SKA) will be able to reveal polarized structure at frequencies as low as several tens of MHz making detailed study of the Galactic halo at low frequencies possible.

However, the interpretation of the values of the power spectra of I, Q, U, P and *RM* is still uncertain. The difficulty comes from the dependence of these observables on magnetic field structure and direction, thermal electron density distribution and path length. The magnetic field fluctuations are coupled to the thermal electron fluctuations which follow a power law extending over ten orders of magnitude (Armstrong et al. 1995; Chepurnov & Lazarian 2010). From here on, α_X represents the angular power spectral index of a parameter X. A given angular scale θ, measured in degrees, is related to the multipole number ℓ that would be obtained by a spherical harmonic transform of spherically gridded data, through the relation $\ell \approx 180°/\theta$ (Haverkorn et al. 2003; Stutz et al. 2014). Spectral indices of polarized intensity vary widely ($0.7 \lesssim \alpha_\mathrm{P} \lesssim 3$) for $\ell \approx 10$ to $\ell \approx 6000$ among surveys at different frequencies and Galactic longitude and latitude (Haverkorn et al. 2003). La Porta & Burigana (2006) find $1 \leq \alpha_\mathrm{P} \leq 1.5$ at 408 MHz to $2 \leq \alpha_\mathrm{P} \leq 3$ at 1.4 GHz for $10 \leq \ell \leq 100$. However, Stutz et al. (2014) showed that at the single frequency of 1.4 GHz, α_P also shows variations from about 0.7 to 4 along the Galactic plane for $\ell \approx 60$ to $\ell \approx 10^4$. α_P varies with Galactic latitude, tracing the disk, halo, and disk-halo transition but no correlation with Galactic longitude is found (Stutz et al. 2014; Haverkorn et al. 2003). α_I is dominated by large scale structure and varies in roughly the same range as α_P with $0.4 \lesssim \alpha_\mathrm{I} \sim 2.2$ or ~ 3.0 but $\alpha_\mathrm{I} \simeq 0$ where extragalactic point sources dominate (Baccigalupi et al. 2001; Bruscoli et al. 2002). La Porta et al. (2008) find $2.5 \leq \alpha_\mathrm{I} \leq 3$ for $\ell \lesssim 200$. Observationally, there is no clear relationship between α_I and α_P (Baccigalupi et al. 2001). Many interferometric surveys do not have reliable α_I due to missing large scale variation in I but do have reliable α_P. Furthermore, power spectral indices of Stokes parameters Q and U are found to strongly correlate with α_P (Stutz et al. 2014, see Fig. 8).

As a first-approach to the problem of interpreting the broad range of observed power spectral indices, our aim is to discern trends between the power spectral index of the tur-

bulent magnetic field α_b and the power spectral indices of the parameters of synchrotron radiation $\alpha_{\rm I}, \alpha_{\rm Q}, \alpha_{\rm U}$, and $\alpha_{\rm P}$ in the context of a generalized high Galactic latitude environment. In this chapter, polarized structure is produced in numerical models by having an isotropic turbulent (random) magnetic field with a non-zero energy spectrum dominate over the regular field throughout the entire synchrotron emitting and Faraday rotating volume. The regular field is separately oriented parallel and then perpendicular to the line of sight. We also determine the effect on the power spectral indices $\alpha_{\rm I}, \alpha_{\rm Q}, \alpha_{\rm U}$, and $\alpha_{\rm P}$ caused by incorporating assumptions of point-wise equipartition/pressure equilibrium between cosmic ray electrons and local total magnetic field and likely level of anti-correlation between cosmic ray electron density and magnetic energy density into our models.

In Sect. 2.2 we describe the physical model chosen for the Galactic ISM, the modeling of magnetic field configurations, the correlation of cosmic ray electron density with the magnetic energy density, and arrive at synthetic maps of the Stokes parameters from independent realizations using diverging lines of sight with subsequent angular power spectrum analysis performed on these maps. We present and discuss results in Sections 2.3 and 3.7 and finally present conclusions in Section 2.5.

2.2 Model description

We consider the Galactic ISM at typical high Galactic latitudes, with short 1 kpc and 2 kpc sight lines, in order to avoid influence from discrete objects such as H II regions, which are concentrated in the disk, and model a synchrotron emitting and Faraday rotating, magneto-ionic medium. Since we are interested in small scale structure in polarization caused by both depth depolarization and beam depolarization we choose a low 'observing' frequency of 350 MHz. This is a typical frequency where polarized has been observed as in (Haverkorn et al. 2003). We further compare our results at 350 MHz with frequencies of 1 GHz, 700 MHz, 500 MHz, 200 MHz and 50 MHz and also consider the case where no Faraday rotation occurs.

The standard input parameters in this model are: a regular magnetic field B (μG) which is separately taken as being parallel and perpendicular to the line of sight ($B_\parallel, B_\perp$), an isotropic turbulent magnetic field b (μG), a maximum turbulent cell size d (pc), and both thermal and cosmic ray electron densities (cm^{-3}).

We adopt a regular magnetic field strength of $3\,\mu$G and add it to the turbulent magnetic field to have a regular field oriented parallel to the line of sight $\boldsymbol{B}_{\rm tot} = \boldsymbol{B}_\parallel + \boldsymbol{b}$, perpendicular to the line of sight $\boldsymbol{B}_{\rm tot} = \boldsymbol{B}_\perp + \boldsymbol{b}$, or with $\boldsymbol{B}_{\rm tot} = \boldsymbol{b}$ (regular field absent). The isotropic turbulent magnetic field has a root mean square (rms) field strength (with mean zero), given by its standard deviation, is fixed to $\sigma_b = 6\,\mu$G with each component $\sigma_{b_i} = (6/\sqrt{3})\,\mu$G where $i = x, y, z$. Moreover, the turbulent field has a power spectrum given by a power law with an adjustable spectral index α_b. The regular magnetic field strength and isotropic turbulent magnetic field strength that are used are comparable with values obtained earlier in the literature: for the regular field $B \sim 2\,\mu$G (Zweibel & Heiles 1997; Sun & Reich 2009) or $B \sim 4\,\mu$G (Zweibel & Heiles 1997; Schnitzeler 2008) and for the turbulent field in the halo $\sigma_b \leq 6\,\mu$G (Jansson & Farrar 2012) or the slightly more

conservative estimate $\sigma_b \sim 3\mu$G assumed in (Sun & Reich 2009). A value of 100 pc is used for the maximum turbulent cell size. We adopt $n_e = 0.014$ cm^{-3} from the value found by Gaensler et al. (2008). Whereas n_e is a constant, the cosmic ray electron density may fluctuate about its constant mean value with $\delta_{n_{cr}} = 0.2$. Based on Haverkorn et al. (2004, Appx. B) for our values of the the path length and observing frequency, we choose $c = 0.6$ where c is a constant proportional to the cosmic ray electron density n_{cr}. The square of the total magnetic field is also correlated with n_{cr} with the correlation parameter C taking on values of $(-1, -0.5, 0, +0.5, +1)$.

We simulate a box of $128 \times 128 \times (640, 1280)$ pixels, where the 640 and 1280 pixels are along the line of sight and represent 1 kpc and 2 kpc, respectively. Then, the field of view is $11^\circ.3$ and $5^\circ.7$, both corresponding to a distance of 200 pc at the far side of the simulation volume (short edge of the box). This gives corresponding angular resolutions of 0.18° and 0.09° per pixel, accounting for the Nyquist sampling frequency which requires 2 pixels per wave. Thus, by construction, the available ℓ range is $31 \leq \ell \leq 1005$ and $63 \leq \ell \leq 2011$ in our simulations which allows for comparison with power spectra in Haverkorn et al. (2003); Stutz et al. (2014).

2.2.1 Random magnetic field

We generate a divergence-free, random, isotropic Gaussian magnetic field with a prescribed energy power spectrum following a similar construction as used for chaotic or turbulent flow modeling (Malik & Vassilicos 1999; Wilkin, S. L. 2006; Wilkin et al. 2007) but with aperiodic boundary conditions. The random vector field $\boldsymbol{b} = (b_x, b_y, b_z)$ is position dependent only and is given as the sum over the N modes of the simulation by

$$\boldsymbol{b}(\boldsymbol{x}) = \sum_{n=1}^{N} \left[\boldsymbol{F}_n \times \hat{\boldsymbol{k}}_n \cos(\boldsymbol{k}_n \cdot \boldsymbol{x}) + \boldsymbol{G}_n \times \hat{\boldsymbol{k}}_n \sin(\boldsymbol{k}_n \cdot \boldsymbol{x}) \right]. \tag{2.1}$$

Each unit vector

$$\hat{\boldsymbol{k}}_n = \begin{pmatrix} \cos\theta \sin\phi \\ \sin\theta \sin\phi \\ \cos\phi \end{pmatrix}$$

and its corresponding wave vector $\boldsymbol{k}_n = k_n \hat{\boldsymbol{k}}_n$ is constructed by selecting at each n a pair of angles (θ, ϕ) randomly from the range $0 \leq \theta < 2\pi, 0 \leq \phi \leq \pi$ such that the pair describes a random point that has equal probability of being chosen in any small area on the surface of a unit sphere. This is achieved by setting

$$\theta = 2\pi u,$$
$$\phi = \arccos(2v - 1),$$

with random variables u, v picked from a uniform distribution on the open interval $(0, 1)$ (Weisstein 2002). It is apparent from Eq. (2.1) that the vector field is solenoidal since $\nabla \cdot \boldsymbol{b} = 0$ is satisfied by construction since $\boldsymbol{k} \cdot (\boldsymbol{X} \times \boldsymbol{k}) = 0$ for any vector $\boldsymbol{X}$. The wave number k_n is constrained by the resolution through $k_n = 2\pi / l_n$, where l_n is the wavelength of the

sinusoidal mode n. The smallest wave number (largest scale) k_1 is given by the number of turbulent cells selected for the box of 128^3 pixels and the largest wave number (smallest scale) k_N is constrained by $2\pi/(5/128)$ where 5 is the minimum number of pixels needed to resolve a wave. The directions of the vectors $\boldsymbol{F}_n$ and $\boldsymbol{G}_n$ are chosen randomly with the constraint that they be normal to $\boldsymbol{k}_n$ which ensures that the mean energy of each mode is $\left(F_n^2 + G_n^2\right)/2$. The individual modes comprising the magnetic field thus have independent random phases and directions and the amount of energy contained in each mode of the magnetic field is controlled by the lengths of the vectors $\boldsymbol{F}_n$ and $\boldsymbol{G}_n$. The magnitudes of $\boldsymbol{F}_n$ and $\boldsymbol{G}_n$ are defined as

$$F_n = G_n = \left[\frac{2}{3} E\left(k_n\right) \Delta k_n\right]^{1/2},$$

where

$$\Delta k_n = \begin{cases} \left(k_{n+1} - k_n\right)/2 & \text{if } n = 1, \\ \left(k_{n+1} - k_{n-1}\right)/2 & \text{if } 2 \leq n \leq N-1, \\ \left(k_n - k_{n-1}\right)/2 & \text{if } n = N, \end{cases}$$

and $E(k_n)$ is the energy spectrum of the inertial range. For our purpose, we assume a power law energy spectrum of the form $E(k_n) = A\left(k_n/k_1\right)^{-\alpha}$ with $\alpha = 3/2$, $5/3$[1], and 2 and mode independent constant A. These values for the slope are physically motivated by predictions from incompressible and compressible magnetohydrodynamic (MHD) turbulence (Cho & Lazarian 2003; Galtier et al. 2005; Beresnyak & Lazarian 2006; Beresnyak 2014) and are chosen to examine the imprint of both steeper and shallower magnetic field spectra with respect to the expected spectrum of $\alpha_b = 5/3$ on $\alpha_{\rm I}, \alpha_{\rm Q}, \alpha_{\rm U}$, and $\alpha_{\rm P}$. In particular, we set $N = 256$ to have a dense sampling of the energy associated with the inertial turbulence range between k_1 and k_N and merge 20 such independent realizations to make the final simulation cubes b_x, b_y, b_z isotropic. A total of 50 such independent simulation cubes, each of which is $128 \times 128 \times 128$ pixels, are generated for each magnetic field component (b_x, b_y, b_z) for each spectral index examined. This, therefore, allows for the 1 kpc and 2 kpc path lengths to be modeled with 10 and 5 statistically independent line-of-sight volumes, respectively. The standard deviation of the resulting spectral indices of the synthetic maps of I, Q, U, P obtained for each of these independent lines of sight is then taken as the error in the spectral index values.

2.2.2 Correlation method

We test whether the parameters I,Q,U, and P can trace correlations or anti-correlations between the magnetic energy density and cosmic ray electron density following Stepanov et al. (2014). For this purpose, we consider a cosmic ray electron density distribution $n_{\rm cr}$,

[1] In the literature, there appear references to a Kolmogorov spectrum for the magnetic field. We emphasize here that a Kolmogorov spectrum strictly refers to the fluctuations of thermal electron density in the local ISM for scales ranging from 10^{-3} AU to 30 pc (Armstrong et al. 1995). A reasonable but unproven assumption states that because turbulent magnetic fields are frozen into the ionized interstellar medium they should follow the Kolmogorov spectrum on these scales (Han 2009).

which fluctuates around its mean value $n_{\mathrm{cr},0}$, given by

$$n_{\mathrm{cr}} = n_{\mathrm{cr},0}\left[1 + \delta_{n_{\mathrm{cr}}}\left(C\,\frac{B_{\mathrm{tot}}^2 - \overline{B_{\mathrm{tot}}^2}}{\sigma_{B_{\mathrm{tot}}^2}} + \sqrt{1-C^2}\,\frac{W-\overline{W}}{\sigma_W}\right)\right], \tag{2.2}$$

where $\delta_{n_{\mathrm{cr}}} \equiv (\sigma_{n_{\mathrm{cr}}}/n_{\mathrm{cr},0}) = 0.2$ is the relative magnitude of cosmic ray number density fluctuations and σ_X denotes the standard deviation of a variable X, the over-bar denotes ensemble averaging, $\boldsymbol{B}_{\mathrm{tot}} = \boldsymbol{B}+\boldsymbol{b}$ is the total magnetic field, and W is an auxiliary positive-definite, scalar random field which is uncorrelated with the magnetic energy density B_{tot}^2. The correlation parameter C is defined as

$$C = \frac{\overline{n_{\mathrm{cr}} B_{\mathrm{tot}}^2} - n_{\mathrm{cr},0}\,\overline{B_{\mathrm{tot}}^2}}{\sigma_{n_{\mathrm{cr}}}\,\sigma_{B_{\mathrm{tot}}^2}}.$$

Equipartition and pressure equilibrium are introduced via setting $C = 1$ and $C = -1$ respectively. A shortcoming of applying this method is that negative values of n_{cr} arise when $C < 0$ (in certain realizations at certain locations) because B_{tot}^2 can attain arbitrarily large values (as a Gaussian random variable squared). The maximum percentage of all such negative values attained from all trials is less than 0.03% for $C = -1$ and less than 0.01% for $C = -0.5$ of the total line-of-sight volume. These negative values of n_{cr} are then set to zero in the numerical calculation. This makes an *exact* anti-correlation between n_{cr} and B_{tot}^2 impossible. However, the actual affect of this truncation of negative values on the power spectrum is negligible.

2.2.3 Stokes parameters

Maps of I,Q,U, and P are obtained through numerical integration of the line-of-sight volume using the composite trapezoidal rule. These maps are not convolved with any beam profile at any stage. Sight lines originate in the center of a short edge of the simulation box and diverge to simulate a cone-like field of view using a cubic spline interpolation method. We have,

$$\begin{aligned}
I(x_\perp) &= \int_0^L \varepsilon(\boldsymbol{x})\; dz,\\
Q(x_\perp) &= \int_0^L \varepsilon(\boldsymbol{x}) \cos\left[2\left(\psi_0 + 0.81\,\lambda^2 \int_z^L n_{\mathrm{e}}\,(B_\parallel + b_\parallel)\,(\boldsymbol{x})\,dz'\right)\right] dz,\\
U(x_\perp) &= \int_0^L \varepsilon(\boldsymbol{x}) \sin\left[2\left(\psi_0 + 0.81\,\lambda^2 \int_z^L n_{\mathrm{e}}\,(B_\parallel + b_\parallel)\,(\boldsymbol{x})\,dz'\right)\right] dz,\\
P(x_\perp) &= \sqrt{Q^2(x_\perp) + U^2(x_\perp)},
\end{aligned}$$

where the synchrotron emissivity ε from each cell is given by

$$\varepsilon(\boldsymbol{x}) = \begin{cases} c\left(B_\perp + b_\perp\right)^2(\boldsymbol{x}) & \text{if } C = 0 \text{ with } \delta_{n_{\mathrm{cr}}} = 0,\\ c(\boldsymbol{x})\left(B_\perp + b_\perp\right)^2(\boldsymbol{x}) & \text{if } C \neq 0 \text{ with } \delta_{n_{\mathrm{cr}}} = 0.2, \end{cases}$$

with c a constant proportional to the cosmic ray electron density $n_{\rm cr}$ defined in Eq. (2.2) and $B_\perp$ and $b_\perp$ ($\perp = \{x, y\}$) the regular and turbulent transverse magnetic field components in μG. Moreover, λ is the 'observing' wavelength (m), ψ_0 is the intrinsic polarization angle, dz' and dz are increments along the line of sight with positive direction pointing toward the observer, $n_{\rm e}$ is the thermal electron density taken to be a constant, L is the total path length (pc), and z denotes the location of each emitting source along the line of sight with $z = 0$ marking the location of the farthest source from the observer. The maximum turbulent cell size d affects Q, U, and P through the dispersion of RM within the simulated volume given by $\sigma_{RM} = 0.81\, n_{\rm e}\, b_\parallel\, (L\, d)^{1/2}$. As a check, histograms of the maps reveal Gaussian distributions for I, Q, and U while the map of P has a Rician distribution, since it is the sum of two Gaussian distributions, as expected. Figure 2.1 shows example maps of the Stokes parameters. Stokes I appears 'patchy' while P evolves from 'patchy' to having one pixel wide 'canals' of low intensity values arising from abrupt changes in the polarization angle to 'grainy' (more power on small scales) with increasing wavelength. The structure of both Stokes Q and U are essentially the same.

2.2.4 Angular power spectrum

In order to quantify the structure in the total intensity and polarization maps and compare with observations, we calculate angular power spectra following Haverkorn et al. (2003) but do not use the APS approach since our models maximally cover 0.3% of the $\sim 41,000$ square degrees on the sky. Instead, we use the PS approach with PS(ℓ) a function of multipole ℓ where $\mathrm{PS}_X(\ell)$ is given by the square of the discrete Fourier transform (DFT) $\mathcal{F}$ of a variable X as $\mathrm{PS}_X(\ell) = |\mathcal{F}(X)|^2$ with the DFT computed via the FFT algorithm. The power spectrum of b is calculated in three dimensions while the power spectra of I, Q, U, and P are computed in two dimensions and averaged over azimuth in radial bins. The multipole spectral index α, defined as $\mathrm{PS}_X(\ell) \propto \ell^{-\alpha_X}$, is calculated from a log-log fit to the power spectrum as in Fig. 2.2.

2.3 Results

We first consider the model with standard parameters as defined in Section 2.2. PS of polarized intensity and Stokes Q at a range of observing frequencies, viz. 1 GHz, 700 MHz, 500 MHz, 350 MHz, 200 MHz and 50 MHz are shown in Fig 2.2. Since the PS become very noisy at large angular scales (small multipoles), due to our limited simulation box size, we only consider multipoles $\ell \gtrsim 150$. At high frequencies (1 GHz and 700 MHz), the PS show an unbroken power law with a spectral index $\alpha_Q, \alpha_P \sim 2.8$ ($\alpha_b = 5/3$). However, at lower frequencies (500 MHz and 350 MHz), the PS show a break, where the spectral index is consistent with the high-frequency PS at small angular scales, but flattens out at larger scales. At small angular scales, the PS amplitude increases while it decreases at large scales due to the flattening of the PS. The location of the break is also frequency dependent; the break occurs at smaller angular scales for lower frequencies. The flattening of the large-scale spectrum increases towards lower frequencies. At the

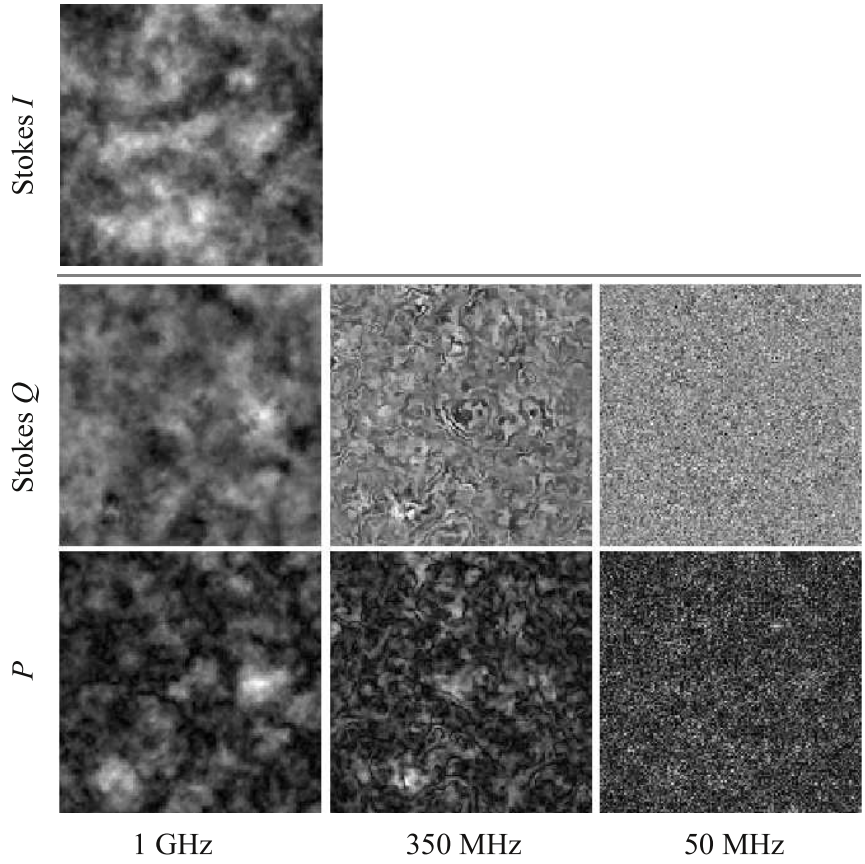

Figure 2.1: Sample simulated output map of Stokes I (top) and sample output maps of Stokes Q (middle) and P (bottom) observed at frequencies of 1 GHz, 350 MHz, and 50 MHz, respectively. All maps featured are for an input turbulent magnetic field power spectrum of 5/3 for the choice of $B = 3\,\mu$G and $\sigma_b = 6\,\mu$G and $C = 0$, $\delta_{n_{cr}} = 0$. A cone line of sight with 1 kpc distance has been used. Outer scale of turbulence is 100 pc. The gray scale range is independent for each parameter since this is more revealing of its structure with lighter shades corresponding to high values and darker shades to low values.

lowest frequencies (200 MHz and 50 MHz), the PS no longer show a break, but rather a flat to inverted PS. The flattening of the PS is more pronounced in the PS of Stokes Q than in P. Flattening of PS of polarized radio emission has been observed frequently (see Section 3.7) and has been explained by increased Faraday rotation and depolarization at low frequencies (Haverkorn et al. 2003). These simulation results show that there is a typical angular scale associated with a break in the PS, which is frequency dependent. In the following, we choose to work with the high spectral index, assuming that the steep part of the spectrum is representative.

Table 2.1: Output power spectral index of total intensity I, Stokes Q and polarized intensity P as a function of input power spectral index of turbulent magnetic field, α_b. The path length is 1 kpc and the outer scale of turbulence is 100 pc. The error in the spectral indices is the standard deviation of 10 independent realizations. The subscripts 'st' and 'sh' denote steep and shallow parts of the broken power spectrum observed at 350 MHz. The error is the standard deviation of 10 independent realizations. These values are given for positive and negative correlation between magnetic fields and cosmic rays represented by parameter C (see text) for $\boldsymbol{B} = 0$.

α_b	α_I	α_Q	α_P
$C = 0$			
$3/2_{\rm st}$	2.4 ± .1	1.2 ± .2	2.2 ± .2
$3/2_{\rm sh}$		.3 ± .2	1.2 ± .2
$5/3_{\rm st}$	2.5 ± .1	1.6 ± .2	2.5 ± .1
$5/3_{\rm sh}$		.4 ± .2	1.4 ± .3
$2_{\rm st}$	2.6 ± .2	2.3 ± .2	3.2 ± .2
$2_{\rm sh}$		.5 ± .2	1.8 ± .3
$C = -0.5$			
$3/2_{\rm st}$	2.2 ± .1	1.2 ± .2	2.0 ± .2
$3/2_{\rm sh}$		.3 ± .2	1.2 ± .2
$5/3_{\rm st}$	2.3 ± .1	1.6 ± .2	2.3 ± .1
$5/3_{\rm sh}$		.4 ± .2	1.3 ± .2
$2_{\rm st}$	2.3 ± .1	2.3 ± .2	2.9 ± .2
$2_{\rm sh}$		.5 ± .2	1.8 ± .3
$C = +0.5$			
$3/2_{\rm st}$	2.3 ± .1	1.2 ± .2	2.1 ± .2
$3/2_{\rm sh}$		.2 ± .2	1.2 ± .2
$5/3_{\rm st}$	2.4 ± .1	1.6 ± .2	2.5 ± .1
$5/3_{\rm sh}$		.4 ± .2	1.4 ± .3
$2_{\rm st}$	2.5 ± .2	2.3 ± .2	3.1 ± .2
$2_{\rm sh}$		.5 ± .2	1.9 ± .3
$C = -1$			
$3/2_{\rm st}$	2.4 ± .1	1.2 ± .1	2.1 ± .2
$3/2_{\rm sh}$		.3 ± .2	1.2 ± .2
$5/3_{\rm st}$	2.5 ± .1	1.6 ± .2	2.4 ± .1
$5/3_{\rm sh}$		.4 ± .2	1.3 ± .2
$2_{\rm st}$	2.7 ± .1	2.3 ± .2	3.1 ± .2
$2_{\rm sh}$		.5 ± .2	1.7 ± .2
$C = +1$			
$3/2_{\rm st}$	2.4 ± .1	1.2 ± .2	2.2 ± .3
$3/2_{\rm sh}$		.2 ± .2	1.2 ± .2
$5/3_{\rm st}$	2.5 ± .1	1.6 ± .2	2.5 ± .1
$5/3_{\rm sh}$		.4 ± .2	1.5 ± .3
$2_{\rm st}$	2.6 ± .2	2.3 ± .2	3.2 ± .2
$2_{\rm sh}$		.5 ± .2	1.9 ± .3

Table 2.2: As in Table 2.1 but for an outer scale of 50 pc.

α_b	α_I	α_Q	α_P
$C = 0$			
$3/2_{st}$	$2.4 \pm .1$	$.6 \pm .1$	$1.6 \pm .2$
$3/2_{sh}$		$-.3 \pm .1$	$.3 \pm .1$
$5/3_{st}$	$2.6 \pm .1$	$.7 \pm .2$	$1.8 \pm .1$
$5/3_{sh}$		$-.2 \pm .2$	$.3 \pm .1$
2_{st}	$2.8 \pm .1$	$1.1 \pm .1$	$2.2 \pm .2$
2_{sh}		$-.2 \pm .2$	$.5 \pm .1$

Table 2.3: As in Table 2.1 but for an outer scale of 100 pc and path length of 2 kpc. The error is the standard deviation of 5 independent realizations.

α_b	α_I	α_Q	α_P
$C = 0$			
$3/2_{st}$	$2.3 \pm .2$	$.1 \pm .1$	$1.2 \pm .2$
$3/2_{sh}$		$-.6 \pm .2$	$0. \pm .2$
$5/3_{st}$	$2.6 \pm .1$	$.3 \pm .1$	$1.4 \pm .1$
$5/3_{sh}$		$-.6 \pm .2$	$.3 \pm .1$
2_{st}	$2.6 \pm .1$	$.6 \pm .1$	$1.9 \pm .1$
2_{sh}		$-.6 \pm .2$	$.5 \pm .1$

Table 2.4: As in Table 2.3 but for an outer scale of 50 pc and path length of 2 kpc.

α_b	α_I	α_Q	α_P
$C = 0$			
$3/2_{st}$	$2.4 \pm .1$	$-.4 \pm .1$	$.6 \pm .1$
$3/2_{sh}$		$-.5 \pm .2$	$-.3 \pm .2$
$5/3_{st}$	$2.5 \pm .1$	$-.1 \pm .1$	$.9 \pm .1$
$5/3_{sh}$		$-.5 \pm .1$	$-.2 \pm .2$
2_{st}	$2.8 \pm .1$	$-.1 \pm .1$	$1.2 \pm .1$
2_{sh}		$-.6 \pm .2$	$0. \pm .2$

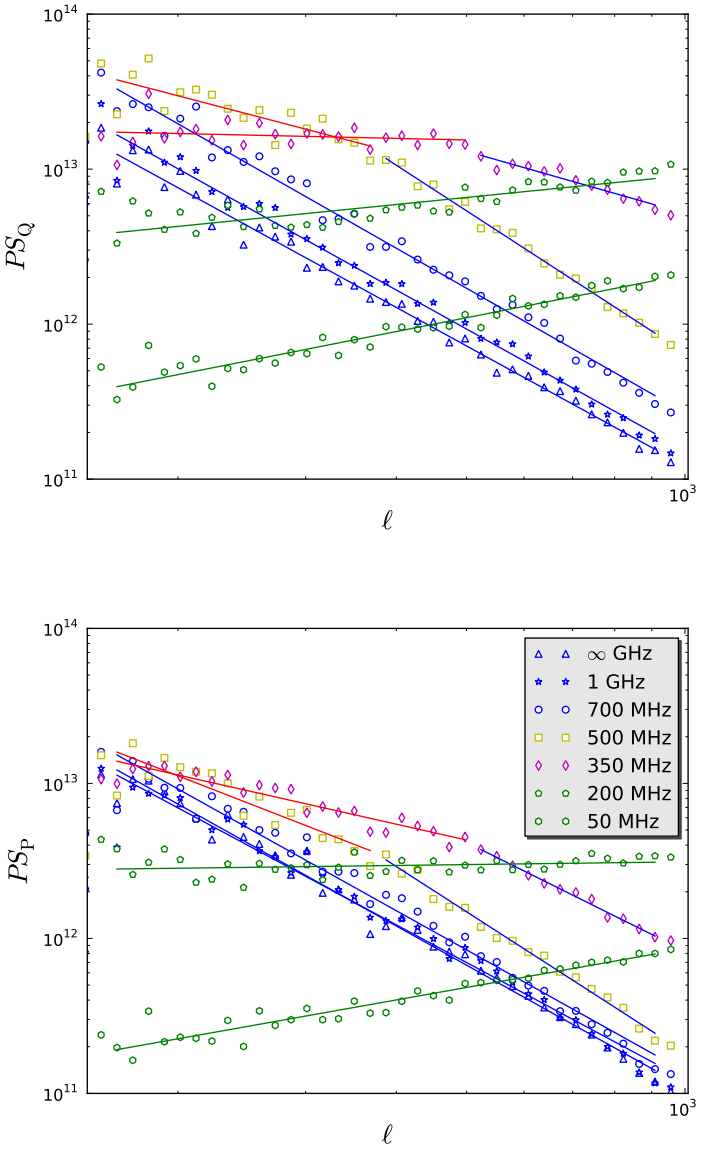

Figure 2.2: Angular power spectra of Stokes Q (right) and polarized intensity P (left) in simulations with $\alpha_b = 5/3$ and standard parameters (see text), for a range of observing frequencies for $\boldsymbol{B} = 0$ and $C = 0$. In the presence of a break, the red and blue solid lines give the best-fit slope for the shallow and steep parts, respectively.

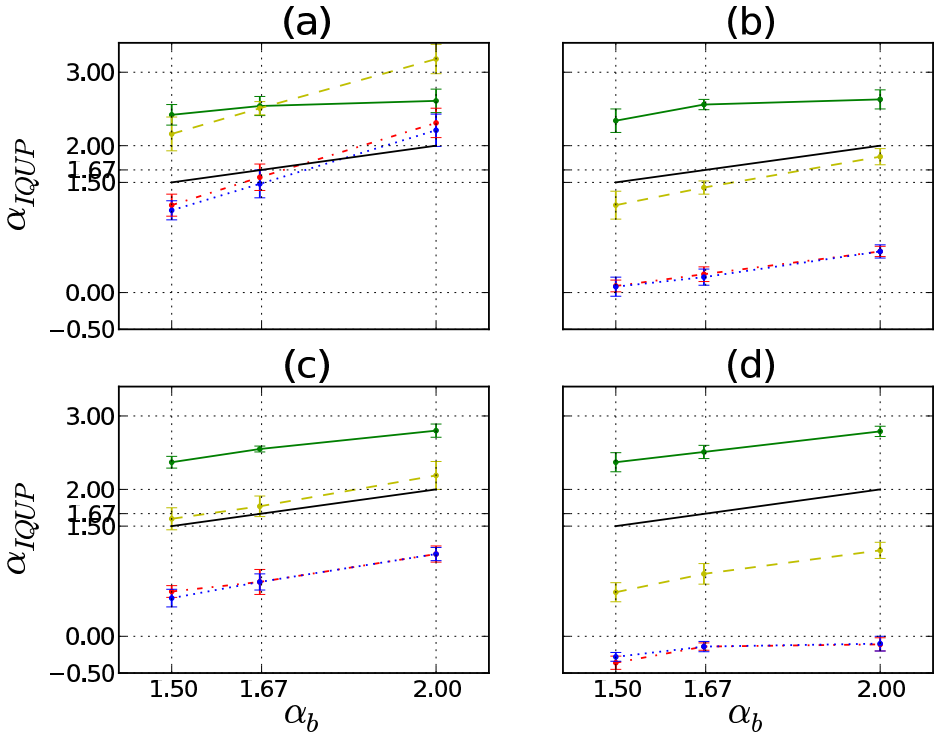

Figure 2.3: Trends of angular power spectra of I, Q, U, and P for input turbulent magnetic field power spectra $\boldsymbol{b}$ at 350 MHz for $\boldsymbol{B} = 0$ and $C = 0$. The solid green line corresponds to α_I, the dashed yellow line to α_P, the red dash dotted line to α_Q, and the blue dotted line to α_U. The solid black line indicates the locus of equality. The following trends are shown: (a) path length of 1 kpc and an outer scale of turbulence of 100 pc, (b) path length of 1 kpc and an outer scale of turbulence of 50 pc, (c) path length of 2 kpc and an outer scale of turbulence of 100 pc, (d) path length of 2 kpc and an outer scale of turbulence of 50 pc. In all these plots, only the steep part of the spectrum has been plotted.

2.3.1 Dependence on magnetic field spectral index

The spectral index of PS of polarized emission should depend on the spectral index of the input turbulent magnetic field. Whether this dependence is unique and whether it can be observed is a crucial question. If this is possible, then we can directly determine magnetic field spectral indices from radiopolarimetric observations. The dependence of spectral indices of I, Q, U and P on the spectral index of the input random, isotropic Gaussian magnetic fields are shown in Fig. 2.3 for our standard frequency of 350 MHz. The four plots show the variation with path length through the medium (1 kpc and 2 kpc) and with outer scale of turbulence (50 pc and 100 pc). All respective spectral index values for these plots are provided in Tables 2.1 - 2.4.

Table 2.5: As in Table 2.1 for $\boldsymbol{B} = 0$ and $C = 0$ but for observing frequencies of 1 GHz and 50 MHz.

α_b	α_I	α_Q	α_P
1 GHz			
3/2	2.4 ± .1	2.6 ± .1	2.6 ± .1
5/3	2.5 ± .1	2.7 ± .1	2.7 ± .1
2	2.6 ± .2	2.8 ± .1	3. ± .1
			* 2.4 ± .2
50 MHz			
3/2	2.4 ± .1	−1. ± .1	−.9 ± .1
5/3	2.5 ± .1	−1. ± .1	−.9 ± .1
2	2.6 ± .2	−1. ± .1	−.8 ± .1

Notes: (*) $B_\perp$

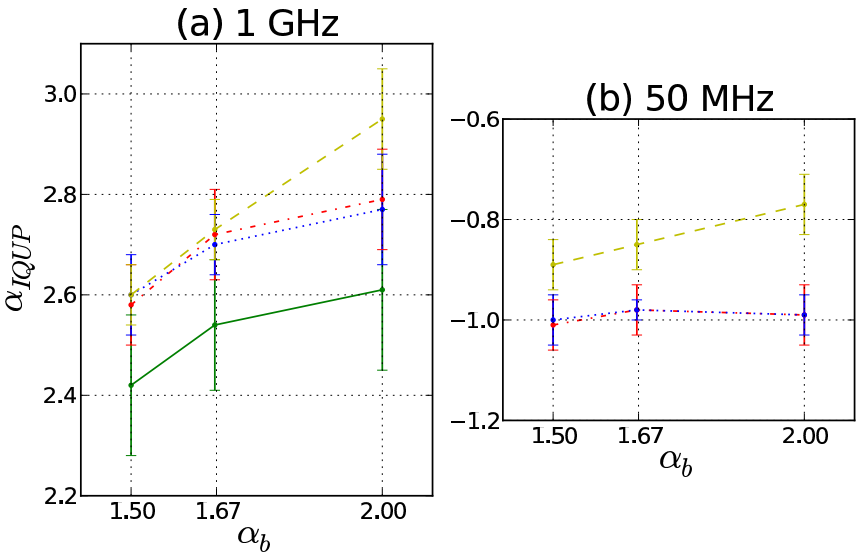

Figure 2.4: Trends of angular power spectra of I, Q, U, and P for $\boldsymbol{B} = 0$ and $C = 0$ at a frequency of 1 GHz (a) and 50 MHz (b). The path length is 1 kpc and the outer scale of turbulence is 100 pc. The legend is the same as in Fig. 2.3. Since α_I is not frequency dependent it is not reproduced in (b).

The spectral indices of I, Q, U, and P increase with increasing α_b as expected. In order to explain our results for the spectral index of I we argue along the following lines. For $\alpha_b = 5/3$ in 1D, one would expect a 3D magnetic field PS of $\alpha_b = 11/3$. Since synchrotron intensity (Stokes I) is the *addition* of emissivity due to these fields along a line of sight, and not an integration over scale k, the spectral index of the 2D Stokes I map should also be $\alpha_I^{2D} = 11/3$. Integrating the Stokes I map to a one-dimensional PS will thus result in $\alpha_I = 8/3$. By analogy, we might expect that $\alpha_I = \alpha_b + 1$ which is supported by our simulations. The spectral index of Stokes I does not depend on outer scale of turbulence or path length, as expected.

Spectral indices of polarized radiation depend on path length and turbulent outer scale, because these change the depolarization characteristics. As expected, $\alpha_Q = \alpha_U$. The spectral indices of Q, U and P increase with increasing α_b, but there is no fixed relation as for α_I. In all situations presented in Fig. 2.3, $\alpha_P > \alpha_Q, \alpha_U$, which means that in Q and U, turbulence creates more small-scale structure than in P.

Polarization spectral indices at 1 GHz and 50 MHz are given in Table 2.5 and Fig. 2.4. At 1 GHz, $\alpha_I \approx \alpha_P \approx \alpha_Q \approx \alpha_U$, indicating that Faraday rotation and depolarization only play a minor role at this frequency. This was also noted observationally at 1.4 GHz (Stutz et al. 2014). In fact, Fig. 2.2 indicates that complete depolarization already occurs at 1 GHz since α_I has the same spectral index as at $\lambda = 0$ (∞ frequency).

2.3.2 Dependence on other input parameters

Figure 2.3 shows the dependence of output spectral indices on path length. Doubling the path length from 1 kpc to 2 kpc does not change the spectrum of Stokes I. However, the spectra of polarized emission (Q, U, and P) become considerably shallower. This result is consistent with the additional depolarization resulting from a longer path length, which converts large scale structure into small scales. Similarly, decreasing the maximum scale of magnetic field fluctuations from 100 pc to 50 pc leads to a shallowing of the polariztion spectra.

Introducing a correlation or anti-correlation between the magnetic field energy density and cosmic ray density by the factor C (see Section 2.2.2) does not alter polarization spectral indices as seen from Table 2.1, but has an effect on the amplitude of the PS, as shown in Fig. 2.5. However, the PS of I for $C = -0.5$ is flatter than for other values of C which is due to an upturn at the smallest scales as seen in panel (a) of the same figure. The largest amplitude in I and P (and similarly for Q and U) arises from equipartition ($C = 1$) whereas the lowest comes from pressure equilibrium ($C = -1$). Since the (anti-) correlation indicates a dependence of $n_{\rm cr}$ on $\boldsymbol{B}_{\rm tot}$ as in Eq. 2.2, this is indeed as expected. Therefore, spectral index studies cannot be used to determine the rate of correlation between magnetic field and cosmic rays in the interstellar medium. Additionally, spectral indices are found to be insensitive to either the presence or the orientation of the regular field $\boldsymbol{B}$ for the regular and turbulent magnetic field strengths considered here.

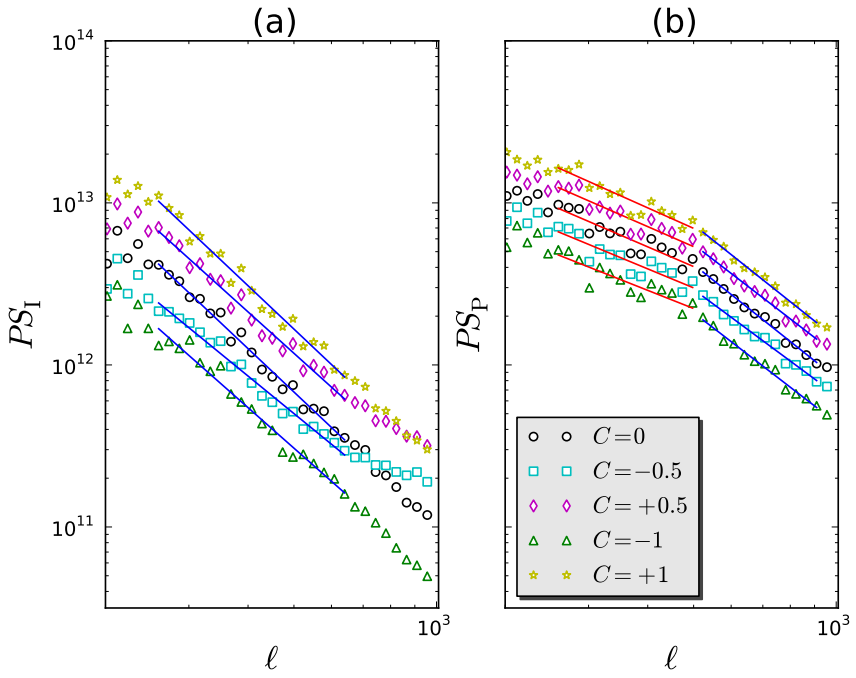

Figure 2.5: Amplitudes of the power spectra of I (a) and P (b) at 350 MHz for $C = 0, \pm 0.5, \pm 1$ (see text), $\alpha_b = 5/3$, and standard parameters.

2.4 Discussion

The aim of this chapter is to establish the dependence of spectral indices of total and polarized intensity and Stokes parameters Q and U on physical parameters in the ISM. Our simulations suggest that total intensity Stokes I is a good tracer of the underlying magnetic field power spectrum as long as magnetic field fluctuations dominate over thermal density fluctuations in the real ISM. However, it may not be possible to distinguish between different α_b using α_I.

Regis (2011) computes Stokes I power spectra for five radio surveys from the literature and finds $\alpha_I = 2.9^{+0.3}_{-0.1}$ for high latitudes, in agreement with our findings of α_I for a spectrum with $\alpha_b = 2$. However, as Regis expects α_I to reproduce the 3D Kolmogorov spectrum of thermal density fluctuations (i.e. $\alpha_I = 11/3$), he concludes that his value of α_I is shallower.

Depolarization has been named as a cause of flattening of power spectra of polarized emission in a number of observational papers (e.g. Baccigalupi et al. (2001); Haverkorn et al. (2003)). We confirm numerically that depolarization flattens the power spectra of the polarized emission. However, since depolarization depends degenerately on many

factors such as path length, turbulent magnetic field, or outer scale of fluctuations, spectral indices of Q, U or P cannot be used to determine the spectral index of turbulent magnetic field. In fact, a large variety of spectral indices of polarized emission is expected to occur even for a single turbulent magnetic field spectrum. A wide range of α_P is indeed observed in the Canadian Galactic Plane Survey and its vertical extensions by Stutz et al. (2014). These authors find an average $\langle\alpha_P\rangle = 2.3$ with significant spatial variation. Their conclusion that α_P increases with Galactic latitude may be a path length effect as shown in our simulations.

Their study also finds that $\alpha_P = \alpha_Q = \alpha_U$ at 1.4 GHz, in agreement with our results. Our simulations also confirm the observed flattening of α_P as a function of observing wavelength (Haverkorn et al. 2003). The simulation result that $\alpha_P > \alpha_Q, \alpha_U$ is generally not confirmed by observations. At low frequencies, $\alpha_P < \alpha_Q, \alpha_U$ is observed (Haverkorn et al. 2003). However, the steepening of α_Q, α_U is attributed to the presence of nearby Faraday screens: these screens will add large-scale structure to Q and U, but not to P. Since our simulation does not contain Faraday screens, we cannot hope to reproduce these observational results.

We show, to our knowledge for the first time, that the PS of Q, U, and P may have a frequency dependent break. The frequency dependence of the angular scale of the break depends on parameters of the turbulence such as magnetic field strength, path length, and thermal electron density. Therefore, measuring the angular scale of the break as a function of frequency may help determine the turbulence parameters. This should be accompanied by simulations testing the dependence of the angular scale of the break on turbulence parameters, which is beyond the scope of this chapter.

An interesting prediction of our simulations is the flattening of the PS at very low frequencies. This means that low-frequency polarimetric observations from e.g. LOFAR or the MWA may seem pure noise, but may contain signal. Polarized intensity PS constructed at very low frequencies should in theory show an inverted power spectrum (to a positive slope). However, in practice this may be difficult to observe due to the low PS amplitude and finite observing beams.

2.5 Summary and conclusions

We constructed static simulations of the magneto-ionized ISM using a power spectrum of random magnetic field with random phases and a predetermined spectral index, constant thermal electron density, and cosmic ray density that can be either constant or (anti-) correlated with magnetic energy density. We simulate radiopolarimetric observations by calculating the propagation of polarized synchrotron radiation through the medium and study the resulting spectral indices α of Stokes I, Q, U and polarized intensity P as a function of magnetic field power spectrum, path length, outer scale of turbulence, correlation of cosmic rays and magnetic field, and frequency.

Our models confirm that more depolarization leads to shallower spectra, where depolarization can be increased by increasing path length or decreasing frequency. We show that smaller outer scales of turbulence lead to smaller α_P, but that (anti-) correlation of

magnetic field and cosmic rays does not have a discernible influence on α_P. The dependence of polarization spectral index on ISM parameters indicates that the variety in α_P in observations, even within the same survey, can originate in a single spectrum of magnetic field. Polarization power spectra not only flatten with decreasing frequency, but show a break at mutipoles that increase with decreasing frequency. At very low frequencies ($\lesssim$ 200 MHz), this can lead to flat or even inverted power spectra. This behavior may become visible with the current low-frequency instruments such as LOFAR or MWA.

Acknowledgements

CS and MH acknowledge the support of research program 639.042.915, which is partly financed by the Netherlands Organization for Scientific Research (NWO). CS is grateful for the additional financial support by the *Leids Kerkhoven-Bosscha Fonds, LKBF* work visit subsidies. AF and AS thank the Leverhulme trust for financial support under grant RPG-097. The simulations were performed on the Coma Cluster at Radboud University, Nijmegen, The Netherlands.

Bibliography

Armstrong, J. W., Rickett, B. J., & Spangler, S. R. 1995, ApJ, 443, 209
Baccigalupi, C., Burigana, C., Perrotta, F., et al. 2001, A&A, 372, 8
Beresnyak, A. 2014, ApJ, 784, L20
Beresnyak, A. & Lazarian, A. 2006, ApJ, 640, L175
Bowman, J. D., Cairns, I., Kaplan, D. L., et al. 2013, PASA, 30, 31
Bruscoli, M., Tucci, M., Natale, V., et al. 2002, New A, 7, 171
Burn, B. J. 1966, MNRAS, 133, 67
Carretti, E., Haverkorn, M., McConnell, D., et al. 2010, MNRAS, 405, 1670
Chepurnov, A. & Lazarian, A. 2010, ApJ, 710, 853
Cho, J. & Lazarian, A. 2003, MNRAS, 345, 325
de Bruyn, A. G., Katgert, P., Haverkorn, M., & Schnitzeler, D. H. F. M. 2006, Astronomische Nachrichten, 327, 487
Gaensler, B. M., Madsen, G. J., Chatterjee, S., & Mao, S. A. 2008, PASA, 25, 184
Galtier, S., Pouquet, A., & Mangeney, A. 2005, Physics of Plasmas, 12, 092310
Han, J. 2009, in IAU Symposium, Vol. 259, IAU Symposium, ed. K. G. Strassmeier, A. G. Kosovichev, & J. E. Beckman, 455–466
Haverkorn, M. & Heesen, V. 2012, Space Sci. Rev., 166, 133
Haverkorn, M., Katgert, P., & de Bruyn, A. G. 2003, A&A, 403, 1045
Haverkorn, M., Katgert, P., & de Bruyn, A. G. 2004, A&A, 427, 169
Heald, G. & LOFAR Collaboration. 2014, in American Astronomical Society Meeting Abstracts, Vol. 223, American Astronomical Society Meeting Abstracts, 236.07
Jansson, R. & Farrar, G. R. 2012, ApJ, 761, L11
Jelić, V., Zaroubi, S., Labropoulos, P., et al. 2008, MNRAS, 389, 1319
La Porta, L. & Burigana, C. 2006, A&A, 457, 1
La Porta, L., Burigana, C., Reich, W., & Reich, P. 2008, A&A, 479, 641
Malik, N. A. & Vassilicos, J. C. 1999, Physics of Fluids, 11, 1572
Regis, M. 2011, Astroparticle Physics, 35, 170
Schnitzeler. 2008, PhD thesis, Leiden University, The Netherlands
Shneider, C., Haverkorn, M., Fletcher, A., & Shukurov, A. 2014, A&A, 567, A82
Simonetti, J. H., Cordes, J. M., & Spangler, S. R. 1984, ApJ, 284, 126
Sokoloff, D. D., Bykov, A. A., Shukurov, A., et al. 1998, MNRAS, 299, 189

Sokoloff, D. D., Bykov, A. A., Shukurov, A., et al. 1999, MNRAS, 303, 207
Stepanov, R., Shukurov, A., Fletcher, A., et al. 2014, MNRAS, 437, 2201
Stutz, R. A., Rosolowsky, E. W., Kothes, R., & Landecker, T. L. 2014, ApJ, 787, 34
Sun, X. H. & Reich, W. 2009, A&A, 507, 1087
Tucci, M., Carretti, E., Cecchini, S., et al. 2002, ApJ, 579, 607
Weisstein, E. W. 2002, Sphere Point Picking, http://mathworld.wolfram.com
Wieringa, M. H., de Bruyn, A. G., Jansen, D., Brouw, W. N., & Katgert, P. 1993, A&A, 268, 215
Wilkin, S. L., Barenghi, C. F., & Shukurov, A. 2007, Physical Review Letters, 99, 134501
Wilkin, S. L. 2006, PhD thesis, Newcastle University, U.K.
Zweibel, E. G. & Heiles, C. 1997, Nature, 385, 131

3

Depolarization of synchrotron radiation in a multilayer magneto-ionic medium

C. Shneider, M. Haverkorn, A. Fletcher, A. Shukurov

Astronomy & Astrophysics, Volume 567, A82 (2014)

Abstract

Depolarization of diffuse radio synchrotron emission is classified in terms of wavelength-independent and wavelength-dependent depolarization in the context of regular magnetic fields and of both isotropic and anisotropic turbulent magnetic fields. Previous analytical formulas for depolarization due to differential Faraday rotation are extended to include internal Faraday dispersion concomitantly, for a multilayer synchrotron emitting and Faraday rotating magneto-ionic medium. In particular, depolarization equations for a two- and three-layer system (disk-halo, halo-disk-halo) are explicitly derived. To both serve as a 'user's guide' to the theoretical machinery and as an approach for disentangling line-of-sight depolarization contributions in face-on galaxies, the analytical framework is applied to data from a small region

in the face-on grand-design spiral galaxy M51. The effectiveness of the multiwavelength observations in constraining the pool of physical depolarization scenarios is illustrated for a two- and three-layer model along with a Faraday screen system for an observationally motivated magnetic field configuration.

3.1 Introduction

Depolarization of linearly polarized synchrotron radiation combined with multiwavelength observations is a powerful diagnostic for probing the constituents of the diffuse interstellar medium (ISM) in galaxies. The medium may be either synchrotron-emitting and Faraday-rotating or only Faraday-rotating (a Faraday screen) depending on whether cosmic ray electrons occur conjointly with thermal electrons and magnetic fields. Magnetic fields encompass regular (mean) fields, which are ordered and coherent on large scales and turbulent fields on small scales. Turbulent fields are further classified as isotropic or anisotropic. An alternative definition of anisotropy in terms of field striation may be found in Jansson & Farrar (2012). The three distinct components of the magnetic field - regular, turbulent isotropic, and turbulent anisotropic - contribute differently to the three observables of total synchrotron intensity (I), polarized synchrotron intensity (P), and the Faraday rotation measure (RM) as discussed in Jaffe et al. (2010); Jansson & Farrar (2012) (see Fig.1 of Jaffe et al. (2010) for an illustration).

The study of depolarization signatures in synchrotron radiation has its origins in the suggestion by Alfvén & Herlofson (1950) that cosmic radio waves result from relativistic electrons spiralling in magnetic fields. For an overview of observational tracers of galactic magnetic fields, see Zweibel & Heiles (1997).

In the context of nearby spiral galaxies, the basic results concerning polarization and Faraday effects stem from the seminal work of Burn (1966) who considered wavelength-dependent depolarization contributions from regular and *isotropic* turbulent magnetic fields to describe the distribution of polarized radiation along the line of sight. Depolarization of synchrotron radiation by anisotropic magnetic fields and the effects of the magneto-ionic medium on the propogation of radio waves had already been described by Ginzburg & Syrovatskii (1965). In particular, Korchakov & Syrovatskii (1962) had arrived at wavelength-independent analytical formulas connecting the degree of polarization to the degree of regularity of the field for the presence of an *anisotropic* magnetic field superimposed on a regular magnetic field as in the spiral arms of the Galaxy. In their introduction, Sokoloff et al. (1998, 1999) provide a concise summary of works on applications of depolarization laws to characterize magnetic fields in radio galaxies, jets, and other radio sources. Burn (1966) considered the case of a symmetric, single-layer uniform slab with constant emissivity and Faraday rotation per unit line of sight (for a review of several other models see Gardner & Whiteoak (1966)).

In the sole presence of regular magnetic fields permeating the (Burn) slab, the polarization angle is a linear function of the square of the wavelength, and the degree of polarization follows the (Burn) depolarization (sinc) function. The Galactic foreground was modeled as a Burn slab in the work of Brentjens & de Bruyn (2005). When an isotropic

Gaussian random magnetic field is also present the Burn depolarization formula is modified to include internal Faraday dispersion (IFD), with dispersion scaling with the quartic power of the wavelength. As noted by Sokoloff et al. (1998), a factor of '2' was missed in the dispersion formula. Moreover, Faraday dispersion in an external screen was also examined and received criticism from Tribble (1991) who modified this result to scale with the quadratic power of the wavelength since the dispersion would cause the spatial correlation length of the polarized emission to decrease with increasing wavelength until it would drop below the size of the turbulent cells (see also Sokoloff et al. (1998)). Burn (1966) also considered wavelength-independent depolarization arising from variations in polarization angle by the presence of isotropic random magnetic fields. This led to the expression for the degree of polarization in terms of the ratio of energy densities of the regular and random magnetic fields as

$$\frac{p_{obs}}{p_{max}} = \frac{B_u^2}{B_u^2 + B_r^2},$$

which was corrected by Heiles (1996) to

$$\frac{p_{obs}}{p_{max}} = \frac{B_u^2}{B_u^2 + \frac{2}{3}B_r^2},$$

for a face-on spiral galaxy. Here, p_{obs} and p_{max} are the observed and maximum degrees of polarization, and B_u and B_r denote the uniform (regular) and random (isotropic turbulent) magnetic fields, respectively.

The work of Sokoloff et al. (1998) generalizes the results of Burn (1966) to describe more complex lines of sight in which magnetic field reversals occur and which pass though a multilayer magneto-ionic medium as characteristic of spiral galaxies. Emissivity and Faraday rotation are no longer constant and may arise from cosmic ray electrons and thermal electrons with differing extents along the line of sight. These authors consider the cases of a symmetric nonuniform slab, an asymmetric slab, and a multilayer slab and show that the polarization angle is no longer a linear function of the wavelength squared in all of these contexts. Additionally, formulas for wavelength-independent depolarization arising from isotropic turbulent and anisotropic turbulent magnetic fields are derived using the rms value for the turbulent magnetic field strength.

We base our method on the multilayer slab approach but now include the simultaneous action of differential Faraday rotation (DFR) and IFD in each layer of a two- or three-layer magneto-ionic medium. An explicit analytical formula for polarization arising from a three-layer medium is provided. We also combine wavelength-dependent and wavelength-independent effects in this framework and allow for regular, isotropic random, and anisotropic random magnetic fields. To the authors' knowledge, this is also the first specific application (in modeling) of the analytical work done on anisotropic fields.

This multilayer approach is intended for modeling nearly face-on galaxies where it is difficult to disentangle the signal from the disk and halo. We apply the developed theoretical machinery to the face-on, grand-design spiral galaxy M51, which lends itself to a decomposition into a disk and a halo thanks to its small angle of inclination.

In this chapter, we lay the foundations for an improved physical modeling of the galaxy, building on previous works (Berkhuijsen et al. 1997; Fletcher et al. 2011) by taking depolarizing effects into account directly, thus enabling a statistical comparison with polarization maps at each observing wavelength. In Chap. 4, we will apply the method to constrain both regular and turbulent field strengths in M51.

3.2 Method

3.2.1 Regular, isotropic turblent, and anisotropic turbulent

We model a nearly face-on spiral galaxy with a disk and a halo. The multilayer decomposition along the line of sight is performed explicitly for a two- (disk-halo) and three-(halo-disk-halo, with the far and near sides of the halo being identical) layer system, in order to examine the depolarization contribution of the side of the halo farthest from the observer. Constant strength regular and turbulent magnetic fields along with a constant cosmic ray density $n_{\rm cr}$ as well as a constant thermal electron density $n_{\rm e}$ serve as independent input for the disk and halo. The effects of wavelength-independent and wavelength-dependent depolarization are directly traced by the normalized degree of polarization that describes the degree to which the measured polarized signal deviates from its intrinsic value. Several depolarization mechanisms are in play in the medium. We focus on the main ones for our modeling and discuss these separately.

The total field is comprised of a regular and fluctuating (turbulent) part and is given by $\boldsymbol{B} = \overline{\boldsymbol{B}} + \boldsymbol{b}$, where the over-bar notation has been adopted to denote the mean field. The fluctuating part is described by a three dimensional turbulent vector field $\boldsymbol{b}$ which is a random variable, with cylindrical components b_r, b_ϕ, b_z (in the galaxy plane) and whose standard deviation is similarly σ_r, σ_ϕ, σ_z. A correlation between the transverse $b_\perp$ and longitudinal b_z components of the turbulent magnetic field $\boldsymbol{b}$ arises from the solenoidality or divergence free condition $\nabla \cdot \boldsymbol{b} = 0$. It is assumed that the effect of such a correlation is negligible, thereby allowing for these components to be treated as uncorrelated (Sokoloff et al. 1998).

As soon as turbulent magnetic fields appear in the description, all related quantities have to be addressed through an expectation value given by a volume average over the random magnetic fluctuations in the source of synchrotron radiation. Since volume averaging will be equal to ensemble averaging in our treatment, the self consistency of the above representation for the total magnetic field may be obtained by *ensemble* averaging both sides and noting that $\boldsymbol{b}$ and its components are random variables with zero mean. Hence, $\overline{\boldsymbol{B}}$ is also an ensemble average of the total field $\boldsymbol{B}$. Upon including the three dimensional turbulent magnetic field $\boldsymbol{b}$ and assuming the standard scaling of emissivity with the square of the perpendicular component of the total magnetic field, $\varepsilon \propto B_\perp^2$, it is the expectation values of $\langle B_k \rangle = \overline{B}_k$ and $\left\langle B_k^2 \right\rangle = \overline{B}_k^2 + \sigma_k^2$ where σ denotes the respective standard deviation with $k = \{x, y, z\}$ and $\langle \ldots \rangle$ represent expectation values or ensemble averages, which feature in equations describing depolarization. Please consult Appx. 3.A for a more detailed explanation and an alternative scaling based on the equipartition as-

sumption.

For isotropy, $\sigma_r = \sigma_\phi = \sigma_z = \sigma$. We include anisotropy caused by compression along spiral arms and by shear from differential rotation and assume it to have the form

$$\sigma_\phi^2 = \alpha\,\sigma_r^2,\ \sigma_r = \sigma_z, \tag{3.1}$$

with $\alpha > 1$. Isotropy may be seen as the case where $\alpha = 1$. We emphasize that the above relations for isotropy and anisotropy, characterized by α, are relations between the square of the standard deviation or variance of the components of $\boldsymbol{b}$ and *not* among components of $\boldsymbol{b}$ itself.

3.2.2 Projection from galaxy-plane to sky-plane coordinates

The total magnetic field and the intrinsic polarization angle of synchrotron radiation must be projected from the galaxy-plane onto the sky-plane. For the regular disk and halo fields, the transformation from galaxy-plane cylindrical polar coordinates to sky-plane Cartesian coordinates proceeds with the introduction of two Cartesian reference frames, one with its origin at M51's center and the second in the sky-plane, with the x-axis of both frames pointing to the northern end of the major axis, and is given as (Berkhuijsen et al. 1997)

$$\begin{aligned}
\overline{B}_x &= B_r\cos(\phi)\ -\ B_\phi\sin(\phi),\\
\overline{B}_y &= \Big[B_r\sin(\phi)\ +\ B_\phi\cos(\phi)\Big]\cos(l) + B_z\sin(l),\\
\overline{B}_\parallel &= -\Big[B_r\sin(\phi)\ +\ B_\phi\cos(\phi)\Big]\sin(l) + B_z\cos(l),
\end{aligned}$$

where l is the inclination angle and $\parallel$ denotes a component of the field parallel to the line of sight.

The random fields, represented by their standard deviations, transform to the sky-plane as

$$\begin{aligned}
\sigma_x^2 &= \Big\langle\Big[b_r\cos(\phi) - b_\phi\sin(\phi)\Big]^2\Big\rangle\\
&= \sigma_r^2\cos^2(\phi) + \sigma_\phi^2\sin^2(\phi),\\
\sigma_y^2 &= \Big\langle\Big\{\Big[b_r\sin(\phi) + b_\phi\cos(\phi)\Big]\cos(l) + b_z\sin(l)\Big\}^2\Big\rangle\\
&= \Big[\sigma_r^2\sin^2(\phi) + \sigma_\phi^2\cos^2(\phi)\Big]\cos^2(l) + \sigma_z^2\sin^2(l),\\
\sigma_\parallel^2 &= \Big\langle\Big\{-\Big[b_r\sin(\phi) + b_\phi\cos(\phi)\Big]\sin(l) + b_z\cos(l)\Big\}^2\Big\rangle\\
&= \Big[\sigma_r^2\sin^2(\phi) + \sigma_\phi^2\cos^2(\phi)\Big]\sin^2(l) + \sigma_z^2\cos^2(l).
\end{aligned} \tag{3.2}$$

It follows from Eqs. (3.1) and (3.2) that anisotropy is given by

$$\sigma_x^2 = \sigma_r^2\Big[\cos^2(\phi) + \alpha\sin^2(\phi)\Big],$$

$$\sigma_y^2 = \sigma_r^2 \left\{ \left[\sin^2(\phi) + \alpha \cos^2(\phi) \right] \cos^2(l) + \sin^2(l) \right\},$$
$$\sigma_\parallel^2 = \sigma_r^2 \left\{ \left[\sin^2(\phi) + \alpha \cos^2(\phi) \right] \sin^2(l) + \cos^2(l) \right\}. \tag{3.3}$$

The intrinsic polarization angle in the presence of regular fields only is given by (Sokoloff et al. 1998)

$$\psi_0 = \tfrac{1}{2}\pi + \arctan\left(\overline{B}_y / \overline{B}_x\right)$$

which acquires an additional term under projection to the sky-plane to (Berkhuijsen et al. 1997)

$$\psi_0 = \tfrac{1}{2}\pi - \arctan\left[\cos(l)\tan(\phi)\right] + \arctan\left(\overline{B}_y / \overline{B}_x\right). \tag{3.4}$$

With the inclusion of turbulent magnetic fields, the last term in the above equation is modified and the intrinsic angle becomes (see Sokoloff et al. (1998) and Appx. 3.A for a derivation of this modification)

$$\langle \psi_0 \rangle = \tfrac{1}{2}\pi - \arctan\left[\cos(l)\tan(\phi)\right] + \tfrac{1}{2}\arctan\left(\frac{2\overline{B}_x \overline{B}_y}{\overline{B}_x^2 - \overline{B}_y^2 + \sigma_x^2 - \sigma_y^2} \right) \tag{3.5}$$

which reduces to Eq. (3.4) for the isotropic case. Hence, for both regular fields without any turbulence and for purely isotropic turbulence the same equation for the intrinsic angle applies.

3.3 The complex polarization

As a result of the assumption that the transverse and longitudinal components of the turbulent magnetic field are uncorrelated, both the emissivity and the intrinsic polarization angle become independent of the total Faraday depth which, consequently, leads to a decoupling of the wavelength-independent and wavelength-dependent effects, and the complex polarization $\mathcal{P}$ for the total magnetic field $\boldsymbol{B}$ may therefore be expressed, based on Sokoloff et al. (1998), as

$$\begin{aligned} \mathcal{P} = & \left(\int_V dV\, w(\boldsymbol{r}) \, \langle \varepsilon(\boldsymbol{r}) \rangle_{W\times h} \right)^{-1} \\ & \times \int_V dV\, \mathcal{P}_0 \, \langle \varepsilon(\boldsymbol{r}) \rangle_{W\times h} \, \exp\left[2\mathrm{i} \left(0.81\, \lambda^2 \int_z^{z_i} n_e \overline{B}_\parallel \, dl' \right) \right] \\ & \times \left\langle \exp\left[2\mathrm{i} \left(0.81\, \lambda^2 \int_z^{z_i} n_e b_\parallel \, dl' \right) \right] \right\rangle_{W\times h} \end{aligned} \tag{3.6}$$

where the intrinsic, complex polarization $\mathcal{P}_0$ is

$$\mathcal{P}_0 = p_0\, w(\boldsymbol{r}) \, \frac{\langle \varepsilon(\boldsymbol{r}) \, \exp\left[\, 2\mathrm{i}\, \psi_0(\boldsymbol{r}) \right] \rangle_{W\times h}}{\langle \varepsilon(\boldsymbol{r}) \rangle_{W\times h}}. \tag{3.7}$$

The intrinsic degree of linear polarization of synchrotron radiation is taken as $p_0 = 0.70$. $w(\boldsymbol{r})$ is the beam profile function of coordinates in the sky-plane, ε is the synchrotron emissivity, and the quantity inside the expectation value angular brackets in the numerator of Eq. (3.7) is known as the complex emissivity. $\overline{B}_{\parallel}$ and $b_{\parallel}$ are the mean and random magnetic field components along the line of sight (μG), $n_{\rm e}$ is the volume density of thermal electrons (cm^{-3}), ψ_0 is the intrinsic value of the local polarization angle ψ at position $\boldsymbol{r}$, and λ is the observing wavelength (m). $\langle \ldots \rangle_{W \times h}$ denotes volume averaging in the synchrotron source, encompassed by the beam cylinder, where W is the area covered by the telescope beam and h is the extent encompassed by a slice within the beam cylinder which should be much smaller than the scale height of the constituents of the magneto-ionic medium. Coordinate l' is measured in pc along the line of sight with positive direction pointing toward the observer with z_i denoting the boundary of either a synchrotron emitting region or a Faraday screen closest to the observer.

The complex polarization is linked to the *observable* polarization quantities, the Stokes parameters I, Q, U, as

$$\mathcal{P} = p \, \exp(2\mathrm{i}\,\Psi)$$

where

$$p = \frac{P}{I} = \frac{\sqrt{(Q^2 + U^2)}}{I}$$

and

$$\Psi = \tfrac{1}{2} \arctan\left(\frac{U}{Q}\right).$$

P is the polarized synchrotron intensity with $p = |\mathcal{P}|$ the degree of polarization, and Q and U may be seen to be the real and imaginary parts of $\mathcal{P}$, respectively, normalized by the total synchrotron intensity $I = \int_V \varepsilon \, dV$ and Ψ is the *observed* polarization angle.

The following additional assumptions are used in the succeeding analysis of depolarization:

1. The degree of polarization p and the polarization angle ψ are affected exclusively by depolarization mechanisms arising from the diffuse ISM *within the galaxy itself*.

2. A sufficiently large number of turbulent correlation cells for both $\varepsilon \exp(2\mathrm{i}\,\psi_0)$ and ε, denoted as N_W, is encompassed by the telescope beam area in order to have *deterministic* values for the complex polarization and, consequently, for the degree of polarization and polarization angle.

3. The beam profile function is for a flat telescope beam profile with $w(\boldsymbol{r}) = 1$.

4. The variation of parameters perpendicular to the line of sight is negligible within the telescope beam.

5. The expectation value of the intrinsic complex polarization $\langle \mathcal{P}_0 \rangle$ is not a function of the line of sight coordinate, where $\mathcal{P}_0$ is defined in Eq. (3.7) above. In general, this assumption no longer holds if the equipartition assumption is invoked as the

longitudinal component of the total field $B_\parallel$ enters the scene and it may be a function of the line of sight coordinate (see Appx. 3.A).

For a multilayer system it may be shown by direct integration of Eq. (3.6) along the line of sight l, with appropriate boundary conditions, that

$$\mathcal{P} = \left(\sum_{i=1}^{N} \langle \varepsilon_i \rangle \, L_i \right)^{-1} \times \sum_{i=1}^{N} \langle \mathcal{P}_{0i} \rangle \, \langle \varepsilon_i \rangle \left(\int_0^L \exp \Big\{ \int_z^L \left[2\mathrm{i} \, (0.81 \, \lambda^2 \, n_{ei} \overline{B}_{\parallel i}) \, - \, d_i \, \lambda^4 \, (0.81 \, \langle n_{ei} \rangle \, b_{\parallel i})^2 \right] dl' \Big\} \, dl \right) \tag{3.8}$$

$$= \sum_{i=1}^{N} \langle \mathcal{P}_{0i} \rangle \, \frac{I_i}{I} \left[\frac{1 - \exp\left(-2 \, \sigma_{RM_i}^2 \lambda^4 + 2\mathrm{i} \, R_i \lambda^2 \right)}{2 \, \sigma_{RM_i}^2 \lambda^4 - 2\mathrm{i} \, R_i \lambda^2} \right] \times \exp \left[2\mathrm{i} \left(\sum_{j=i+1}^{N} R_j \, \lambda^2 \right) \right], \tag{3.9}$$

where the per-layer total synchrotron emission I_i, the total Faraday depth[1] R_i, and the dispersion of the intrinsic rotation measure (RM) within the volume of the telescope beam σ_{RM_i} are respectively given as

$$I_i = \varepsilon_i \, L_i,$$

$$R_i = 0.81 \, n_{\mathrm{e}i} \, \overline{B}_{\parallel i} \, L_i, \tag{3.10}$$

$$\sigma_{RM_i} = 0.81 \, \langle n_{\mathrm{e}i} \rangle \, b_{\parallel i} \, (L_i \, d_i)^{1/2}, \tag{3.11}$$

and where

$$\langle \mathcal{P}_{0i} \rangle = p_0 \frac{\langle \varepsilon_i \, \exp(2\mathrm{i} \, \psi_{0i}) \rangle}{\langle \varepsilon_i \rangle} \tag{3.12}$$

is similarly given, as first introduced in Eq. (3.7), but now as a layer-dependent, averaged quantity. The σ_{RM} of Eq. (3.11) will be used in our modeling of wavelength-dependent depolarization due to isotropic and anisotropic turbulent magnetic fields in Section 3.5.2. In so doing, we make the implicit assumption that σ_{RM} may be taken as independent of observing angle as for a purely random magnetic field. From Eq. (3.9) we observe that wavelength-independent depolarization contributions may be directly appended to the terms expressing wavelength-dependent depolarization as if they were effectively constants.

The sum in Eqs. (3.8) and (3.9) is over independent, *uniform* layers indexed by i and N is the total number of layers in the medium with the Nth layer nearest the observer.

[1] Faraday depth and Faraday rotation measure (RM) are equivalent when the observed polarization angle Ψ is a linear function of λ^2 such as in a medium where synchrotron emission and Faraday rotation are separated. They differ only when this linearity no longer holds as for a medium with synchrotron emission and Faraday rotation mixed. A positive Faraday depth means that the magnetic field points toward the observer. See Brentjens & de Bruyn (2005) for further discussion.

ψ_{0i} is the initial angle of polarization (rad), $L = \sum_i L_i$ is the total path length through the medium (pc), $I = \sum_i I_i$ is the total synchrotron intensity from all layers, and d_i is the diameter of a turbulent cell (pc) in a layer. A constructive feature of the complex polarization $\mathcal{P}$ is that it is an *additive* quantity; the total combined complex polarization from all layers is the sum of the complex polarizations arising in each layer weighted by the fractional synchrotron intensity I_i/I.

3.4 Wavelength-independent depolarization

From Eq. (3.12) we observe that wavelength-independent depolarization can only modify the intrinsic degree of polarization in the presence of turbulent magnetic fields. It stems from a tangling of magnetic field lines in the emission region both along the line of sight and across the beam on all scales. Denoting the isotropic, anisotropic, and isotropic with anisotropic instances of $(|\langle\mathcal{P}_{0i}\rangle|/p_0))$ by $(W_I)_i$, $(W_A)_i$, and $(W_{AI})_i$, as well as a generic wavelength-independent depolarizing term by W_i, we have (Sokoloff et al. 1998)

$$(W_A)_i = \left\{ \frac{\left[\left(\overline{B}_x^2 - \overline{B}_y^2 + \sigma_x^2 - \sigma_y^2\right)^2 + 4\overline{B}_x^2\overline{B}_y^2\right]^{1/2}}{\overline{B_\perp^2}} \right\}_i , \tag{3.13}$$

where $\overline{B}_\perp^2 = \overline{B}_x^2 + \overline{B}_y^2$ and $\overline{B_\perp^2} = \overline{B}_\perp^2 + \sigma_x^2 + \sigma_y^2$ (see Appx. 3.A for a derivation). The subscripted i appears on the braces to indicate that all magnetic fields occurring in the equation are representative of a particular layer. Equation (3.13) reduces in the isotropic case to

$$(W_I)_i = \left(\frac{\overline{B}_\perp^2}{\overline{B}_\perp^2 + 2\sigma^2} \right)_i . \tag{3.14}$$

When both isotropic and anisotropic fields are present in a layer then

$$(W_{AI})_i = \left(\frac{\overline{B}_\perp^2}{\overline{B}_\perp^2 + 2\sigma^2} \right)_i \underbrace{\left\{ \frac{\left[\left(\overline{B}_x^2 - \overline{B}_y^2 + \sigma_x^2 - \sigma_y^2\right)^2 + 4\overline{B}_x^2\overline{B}_y^2\right]^{1/2}}{\overline{B_\perp^2}} \right\}_i}_{\sigma_x \neq \sigma_y} . \tag{3.15}$$

With the occurrence of both isotropic and anisotropic turbulent magnetic fields in the same layer, there is consecutive depolarization by these fields as contained in Eq. (3.15). The two turbulent fields are viewed as describing two spatially separate, bulk regions in the galaxy that do not interact.

In the context of a purely random field $\boldsymbol{B} = \boldsymbol{b}$, from Eq. (3.13) it is observed that

complete depolarization may be avoided only with an *anisotropic* random magnetic field

$$(W_A)_i = \left(\frac{\left| \sigma_x^2 - \sigma_y^2 \right|}{\sigma_x^2 + \sigma_y^2} \right)_i , \; \sigma_x \neq \sigma_y . \tag{3.16}$$

Equation (3.16) implies that the smaller the difference between σ_x and σ_y, the nearer the turbulent field to being purely random, and the closer the signal to being completely depolarized. On the other hand, the greater the difference between the standard deviations, the weaker the contribution of wavelength-independent depolarization, and the closer the signal to its intrinsic degree of polarization. In the absence of any random fields, $\sigma_k = 0$, and it is readily observed that there is no wavelength-independent depolarization contribution, with $|\langle \mathcal{P}_{0i} \rangle| = p_0$, in Eqs. (3.13) - (3.15).

3.5 Wavelength-dependent depolarization

3.5.1 Differential Faraday rotation

Differential Faraday rotation occurs when emission from different depths in the emitting layer, along the *same* line of sight, experience different amounts of Faraday rotation due to the presence of *regular* fields. For a regular field only, $\boldsymbol{B} = \overline{\boldsymbol{B}}$, Eq. (3.9) becomes (Sokoloff et al. 1998)

$$\mathcal{P}_{\left(\boldsymbol{B}=\overline{\boldsymbol{B}}\right)} = p_0 \sum_{i=1}^{N} \frac{I_i}{I} \frac{\sin\left(R_i \lambda^2\right)}{\left(R_i \lambda^2\right)} \exp\left[2\mathrm{i} \left(\psi_{0i} + \frac{R_i}{2} \lambda^2 + \sum_{j=i+1}^{N} R_j \, \lambda^2 \right) \right] . \tag{3.17}$$

Equation (3.17) shows that the polarized emission coming from a given layer has an initial degree of polarization determined by the Faraday depth in that layer and that the signal's intrinsic polarization angle undergoes Faraday rotation with $RM = R_i/2$ in the originating layer and $RM = R_j$ in each successive layer, which function as Faraday screens for the emission from layers deeper than themselves.

For the goal of this chapter, the above equation is explicitly expanded to a two- and three-layer medium. For a two-layer system, with a halo between the disk and observer, this is given by

$$\begin{aligned} \left(\frac{p}{p_0} \right)_{2layer} &= \left| \frac{I_d}{I} \frac{\sin\left(R_d \lambda^2\right)}{\left(R_d \lambda^2\right)} e^{2\mathrm{i}\left[\psi_{0d} + \left(\frac{R_d}{2} + R_h\right)\lambda^2\right]} \right. \\ &\quad \left. + \frac{I_h}{I} \frac{\sin\left(R_h \lambda^2\right)}{\left(R_h \lambda^2\right)} e^{2\mathrm{i}\left(\psi_{0h} + \frac{R_h}{2}\lambda^2\right)} \right| \\ &= \left\{ A_d^2 + A_h^2 + 2\, A_d\, A_h \, \cos\left[2\, \Delta\psi_{dh} + (R_d + R_h)\, \lambda^2 \right] \right\}^{1/2} , \end{aligned} \tag{3.18}$$

where

$$A_i = (I_i/I) \frac{\sin\left(R_i \lambda^2\right)}{\left(R_i \lambda^2\right)} = (I_i/I) \, \mathrm{sinc}\left(R_i \, \lambda^2\right) . \tag{3.19}$$

The subscripts $i = d, h$ refer to the disk and halo, and $\Delta\psi_{dh} = \langle\psi_{0d}\rangle - \langle\psi_{0h}\rangle$ is the difference in the intrinsic angle of polarization between the disk and halo. Equation (3.18), in particular, is a typo-corrected form of the equation as it appears in Sokoloff et al. (1998), and it was derived in the work of Chadderton (2011). The corresponding equation for a three-layer (halo-disk-halo) system, where the far and near sides of the halos are identical, is given by

$$\begin{aligned}\left(\frac{p}{p_0}\right)_{3layer} &= \left|\frac{I_h}{I}\frac{\sin\left(R_h\lambda^2\right)}{(R_h\lambda^2)}\left\{e^{2\mathrm{i}\left[\psi_{0h}+\left(\frac{3R_h}{2}+R_d\right)\lambda^2\right]} + e^{2\mathrm{i}\left(\psi_{0h}+\frac{R_h}{2}\lambda^2\right)}\right\}\right. \\ &\quad \left. + \frac{I_d}{I}\frac{\sin\left(R_d\lambda^2\right)}{(R_d\lambda^2)}\,e^{2\mathrm{i}\left[\psi_{0d}+\left(\frac{R_d}{2}+R_h\right)\lambda^2\right]}\right| \\ &= \left(2A_h^2\left\{1 + \cos\left[2\left(R_d+R_h\right)\lambda^2\right]\right\} + A_d^2\right. \\ &\quad + 2A_dA_h\left\{\cos\left[-2\Delta\psi_{dh} + \left(R_d+R_h\right)\lambda^2\right]\right. \\ &\quad \left.\left. + \cos\left[2\Delta\psi_{dh} + \left(R_d+R_h\right)\lambda^2\right]\right\}\right)^{1/2}. \end{aligned} \tag{3.20}$$

3.5.2 Internal Faraday dispersion

Internal Faraday dispersion results from polarized signal undergoing different amounts of Faraday rotation both along the line of sight and across the telescope beam *within* a region of synchrotron emission when the telescope beam encompasses many turbulent cells.

For a purely random field, $\boldsymbol{B} = \boldsymbol{b}$, Eq. (3.9) becomes

$$\mathcal{P}_{(\boldsymbol{B}=\boldsymbol{b})} = \sum_{i=1}^{N}\langle\mathcal{P}_{0i}\rangle\,\frac{I_i}{I}\,\frac{\sinh\left(\sigma_{RM_i}^2\lambda^4\right)}{\left(\sigma_{RM_i}^2\lambda^4\right)}\,\exp\left(-\sigma_{RM_i}^2\lambda^4\right). \tag{3.21}$$

In contrast to DFR, the intrinsic polarization angle remains completely unaffected by any contributions to the phase from Faraday dispersion because such contributions by random fields are zero on average.

Upon comparing Eqs. (3.17) and (3.21), it is apparent that the A_i in Eq. (3.19) has been modified to (Burn 1966; Sokoloff et al. 1998)

$$\begin{aligned}\tilde{A}_i &= (I_i/I)\left[\frac{1-\exp\left(-2\,\sigma_{RM_i}^2\lambda^4\right)}{2\,\sigma_{RM_i}^2\lambda^4}\right] \\ &= (I_i/I)\,\frac{\sinh\left(\sigma_{RM_i}^2\lambda^4\right)}{\left(\sigma_{RM_i}^2\lambda^4\right)}\,\exp\left(-\sigma_{RM_i}^2\lambda^4\right),\end{aligned}$$

and that Eqs. (3.18) and (3.20) are modified to

$$\left(\frac{p}{p_0}\right)_{2layer} = (WA)_d\,\tilde{A}_d + (WA)_h\,\tilde{A}_h,$$

$$\left(\frac{p}{p_0}\right)_{3layer} = 2\,(WA)_h\,\tilde{A}_h + (WA)_d\,\tilde{A}_d.$$

A fundamental physical change has been effected; the sinc function with its non-monotonic, π-periodic zero-crossings in Eq. (3.17) has now been replaced by a monotonically decreasing function of Faraday depth in Eq. (3.21) as the product of a *hyperbolic* sinc function with an exponential decay.

3.5.3 External Faraday dispersion

When polarized emission is modeled as arising exclusively from the disk, by having the halo devoid of any cosmic ray electrons, a two- and three-layer model approach to depolarization becomes degenerate since there is no longer a sum over depolarization terms but rather a single term that describes the Faraday depolarization contribution from the disk, together with the influence of the near halo (nearest to the observer) on the polarized signal. In particular, the far halo, coming from a three-layer model, would be completely dormant in terms of polarized signal. With only regular fields present in the halo, the halo contributes with just a Faraday rotating phase term that does not affect the degree of polarization.

With the inclusion of turbulent fields in the halo, the halo functions as a Faraday screen, contributing an external Faraday dispersion (EFD) term. *External* refers to the turbulent fields between the observer and the source. Having both regular and turbulent magnetic fields present in the disk and halo entails having DFR and IFD in the disk, together with EFD in the halo, and yields

$$\begin{aligned}\left(\frac{p}{p_0}\right)_{EFD} &= \left|\frac{\langle\mathcal{P}_{0d}\rangle}{p_0}\left[\frac{1-\exp\left(-2\,\sigma_{RM_d}^2\lambda^4+2\,\mathrm{i}\,R_d\lambda^2\right)}{2\,\sigma_{RM_d}^2\lambda^4-2\,\mathrm{i}\,R_d\lambda^2}\right]\right. \\ &\quad\left.\times\,\exp\left[2\mathrm{i}\left(\psi_{0d}+R_h\lambda^2\right)-2\sigma_{RM_h}^2\lambda^4\right]\right| \\ &= W_d\left[\frac{1-2\,e^{-2\,\sigma_{RM_d}^2\lambda^4}\cos\left(2\,R_d\lambda^2\right)+e^{-4\,\sigma_{RM_d}^2\lambda^4}}{\left(-2\,\sigma_{RM_d}^2\lambda^4\right)^2+\left(2\,R_d\lambda^2\right)^2}\right] \\ &\quad\times\,\exp\left(-2\sigma_{RM_h}^2\lambda^4\right). \end{aligned} \tag{3.22}$$

A fractional synchrotron intensity term I_d/I does not appear since all of the synchrotron emission stems from the disk (i.e., $I_d = I$).

For regular magnetic fields in the disk alone, along with turbulent magnetic fields in the halo, the equation is the natural reduction of Eq. (3.22) in this limit and is given by (Burn 1966; Sokoloff et al. 1998)

$$\left(\frac{p}{p_0}\right)_{EFD} = \left|\frac{\sin\left(R_d\lambda^2\right)}{\left(R_d\lambda^2\right)}\,\exp\left[2\mathrm{i}\left(\psi_{0d}+\frac{R_d}{2}\lambda^2+R_h\lambda^2\right)-2\sigma_{RM_h}^2\lambda^4\right]\right|$$

$$= \frac{\sin\left(R_d\lambda^2\right)}{(R_d\lambda^2)}\,\exp\left(-2\sigma^2_{RM_h}\lambda^4\right). \tag{3.23}$$

3.5.4 Depolarization from DFR with IFD

We derive equations for depolarization arising from IFD occurring concomitantly with DFR from Eq. (3.9). For a two-layer system (with a halo between the disk and observer as in Eq. (3.18)), this is given by

$$\begin{aligned}
\left(\frac{p}{p_0}\right)_{2layer} &= \left|\frac{\langle\mathcal{P}_{0d}\rangle}{p_0}\,\frac{I_d}{I}\left[\frac{1-e^{\left(-2\,\sigma^2_{RM_d}\lambda^4+2\,\mathrm{i}\,R_d\lambda^2\right)}}{2\,\sigma^2_{RM_d}\lambda^4-2\,\mathrm{i}\,R_d\lambda^2}\right]e^{2\mathrm{i}\left(\psi_{0d}+R_h\lambda^2\right)}\right.\\
&\quad\left.+\,\frac{\langle\mathcal{P}_{0h}\rangle}{p_0}\,\frac{I_h}{I}\left[\frac{1-e^{\left(-2\,\sigma^2_{RM_h}\lambda^4+2\,\mathrm{i}\,R_h\lambda^2\right)}}{2\,\sigma^2_{RM_h}\lambda^4-2\,\mathrm{i}\,R_h\lambda^2}\right]e^{2\mathrm{i}\psi_{0h}}\right|\\
&= \left\{W_d^2\left(\frac{I_d}{I}\right)^2\left(\frac{1-2e^{-\Omega_d}\cos C_d+e^{-2\Omega_d}}{\Omega_d^2+C_d^2}\right)\right.\\
&\quad+\,W_h^2\left(\frac{I_h}{I}\right)^2\left(\frac{1-2e^{-\Omega_h}\cos C_h+e^{-2\Omega_h}}{\Omega_h^2+C_h^2}\right)\\
&\quad+\,W_dW_h\,\frac{I_dI_h}{I^2}\,\frac{2}{F^2+G^2}\Big[\{F,G\}\,(2\Delta\psi_{dh}+C_h)\\
&\quad+\,e^{-(\Omega_d+\Omega_h)}\,\{F,G\}\,(2\Delta\psi_{dh}+C_d)\\
&\quad-\,e^{-\Omega_d}\,\{F,G\}\,(2\Delta\psi_{dh}+C_d+C_h)\\
&\quad\left.-\,e^{-\Omega_h}\,\{F,G\}\,(2\Delta\psi_{dh})\Big]\right\}^{1/2},
\end{aligned} \tag{3.24}$$

where $\Omega_d = 2\sigma^2_{RM_d}\lambda^4$, $\Omega_h = 2\sigma^2_{RM_h}\lambda^4$, $C_d = 2R_d\lambda^2$, $C_h = 2R_h\lambda^2$, $F = \Omega_d\Omega_h + C_dC_h$, $G = \Omega_hC_d - \Omega_dC_h$. The operation $\{F,G\}\,(a)$ is defined as $\{F,G\}\,(a) = F\cos(a) - G\sin(a)$.

The corresponding equation for a three-layer system (with far and near halos identical as in Eq. (3.20)) is given by

$$\begin{aligned}
\left(\frac{p}{p_0}\right)_{3layer} &= \left|\frac{\langle\mathcal{P}_{0h}\rangle}{p_0}\,\frac{I_h}{I}\left[\frac{1-e^{\left(-2\,\sigma^2_{RM_h}\lambda^4+2\,\mathrm{i}\,R_h\lambda^2\right)}}{2\,\sigma^2_{RM_h}\lambda^4-2\,\mathrm{i}\,R_h\lambda^2}\right]\left\{e^{2\mathrm{i}\left[\psi_{0h}+(R_d+R_h)\lambda^2\right]}\right.\right.\\
&\quad\left.+\,e^{2\mathrm{i}\,\psi_{0h}}\right\}+\,\frac{\langle\mathcal{P}_{0d}\rangle}{p_0}\,\frac{I_d}{I}\left[\frac{1-e^{\left(-2\,\sigma^2_{RM_d}\lambda^4+2\,\mathrm{i}\,R_d\lambda^2\right)}}{2\,\sigma^2_{RM_d}\lambda^4-2\,\mathrm{i}\,R_d\lambda^2}\right]e^{2\mathrm{i}\left(\psi_{0d}+R_h\lambda^2\right)}\Bigg|\\
&= \left(2\,W_h^2\left(\frac{I_h}{I}\right)^2\left\{\frac{\left(1-2e^{-\Omega_h}\cos C_h+e^{-2\Omega_h}\right)\left[1+\cos\left(C_d+C_h\right)\right]}{\Omega_h^2+C_h^2}\right\}\right.
\end{aligned}$$

$$
\begin{aligned}
&+ W_d^2 \left(\frac{I_d}{I}\right)^2 \left(\frac{1 - 2e^{-\Omega_d}\cos C_d + e^{-2\Omega_d}}{\Omega_d^2 + C_d^2}\right) \\
&+ W_d W_h \frac{I_d I_h}{I^2} \frac{2}{F^2 + G^2} \Bigg\{ \{F, -G\}\,(-2\Delta\psi_{dh} + C_d) \\
&+ \{F, G\}\,(2\Delta\psi_{dh} + C_h) \\
&+ e^{-(\Omega_d + \Omega_h)} \Big[\{F, G\}\,(2\Delta\psi_{dh} + C_d) + \{F, -G\}\,(-2\Delta\psi_{dh} + C_h) \Big] \\
&- e^{-\Omega_d} \Big[\{F, G\}\,(2\Delta\psi_{dh} + C_d + C_h) + \{F, -G\}\,(-2\Delta\psi_{dh}) \Big] \\
&- e^{-\Omega_h} \Big[\{F, -G\}\,(-2\Delta\psi_{dh} + C_d + C_h) + \{F, G\}\,(2\Delta\psi_{dh}) \Big] \Bigg\} \Bigg)^{1/2} . \qquad (3.25)
\end{aligned}
$$

The symmetry properties of these equations will be reserved for discussion in Appx. 3.B. The above equations explicitly show the competition between the turbulent and regular fields with the σ_{RM} and R strictly characterizing exponential decay and periodicity.

Figure 3.1 contains the depolarization profiles, with normalized degree of polarization plotted against wavelength, for a one-, two-, and three-layer magneto-ionic medium with DFR, IFD, and DFR with IFD. The wavelength-independent polarization has been assumed to be 0.5 for illustration purposes. Its actual value should be fit to observations at a small enough wavelength to make wavelength-dependent depolarization effects negligible. With an increasing number of magneto-ionic layers modeled, the DFR curve has complete depolarization occurring at progressively earlier wavelengths. Comparing the IFD curve for a single and multilayer medium reveals that the IFD curve persists at longer wavelengths and thus is less effective as a depolarizing mechanism in a multilayer medium. The 'jagged' profile of the DFR curve in (b) relative to the smooth profile of (a) arises from there being two sinc functions with differing Faraday depths. For a three-layer system in (c), the halo sinc function alone determines the DFR curve thanks to the disk's small fractional synchrotron intensity, which accounts for the smoothness. Comparing the Burn (1966) and Sokoloff et al. (1998) result for DFR with IFD in a one-layer uniform slab (a), represented by the sole presence of a disk, with that in a two-layer medium (b) given by a disk plus a halo reveals that the presence of a halo supports polarization at longer wavelengths. Similarly, DFR with IFD in a three-layer medium (c) with identical far and near sides of the halo undergoes a drastic change in profile, which more closely resembles a one-layer halo polarization profile.

3.6 Modeling example: application to M51

We illustrate our method for the case of the nearby grand-design spiral galaxy M51, with its high galactic latitude of $b = +68.6°$ and with an inclination angle $l = -20°$. It is assumed that the observed emission is exclusively from M51 because of the high galactic latitude (Berkhuijsen et al. 1997). We use the Fletcher et al. (2011) model predictions of a two-dimensional regular magnetic field $\sum_m \boldsymbol{B}_m(r)\cos(m\phi - \beta_m)$ for both the disk and halo for a small region (a sector of radial size 1.2 kpc and azimuthal extent 20°) of

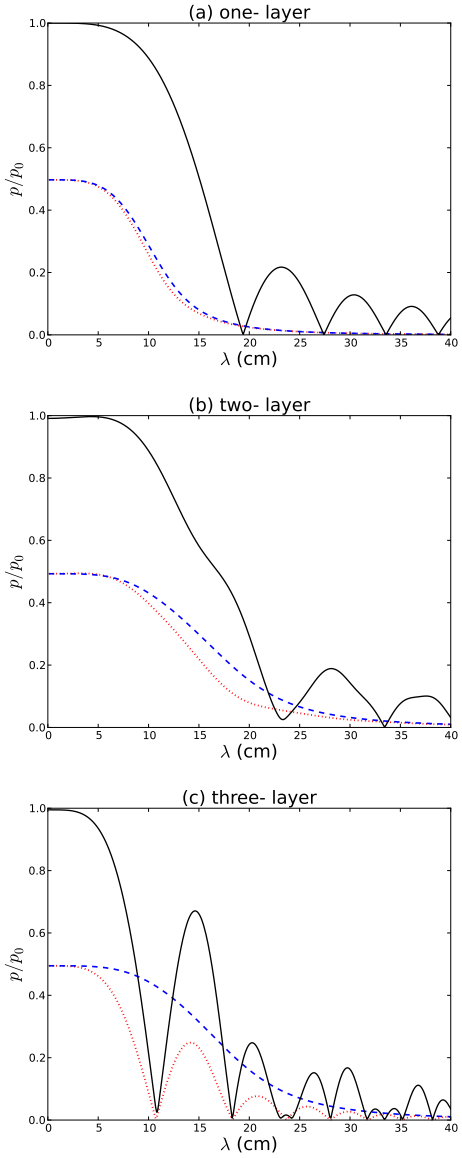

Figure 3.1: Normalized degree of polarization as a function of wavelength illustrated for a one-layer (a), two-layer (b), three-layer (c) system with characteristic profiles for DFR only (black solid), IFD only (blue dashed), and DFR with IFD (red dotted). A total isotropic turbulent magnetic field strength of $5\,\mu$G together with a total regular magnetic field strength also of $5\,\mu$G has been used in the disk and in the halo. The parameters of $n_{\rm e}, n_{\rm cr}, L, d, \alpha$ used in the construction of these plots are the same as those for the example bin of Section 3.6 and their values are reported in the bottom panel of Table 3.1.

the galaxy. The turbulent magnetic field in the disk and halo is three dimensional. We compare the observed degrees of polarization at $\lambda\lambda\lambda$ 3.5, 6.2, 20.5 cm with those expected from different models of the depolarization for this bin.

The regular disk and halo magnetic field configurations in cylindrical polar coordinates are

$$\begin{aligned} B_r &= B_0 \sin(p_0) + B_2 \sin(p_2) \cos(2\phi - \beta_2), \\ B_\phi &= B_0 \cos(p_0) + B_2 \cos(p_2) \cos(2\phi - \beta_2), \\ B_z &= 0, \\ B_{\mathrm{h}r} &= B_{\mathrm{h}0} \sin(p_{\mathrm{h}0}) + B_{\mathrm{h}1} \sin(p_{\mathrm{h}1}) \cos(\phi - \beta_{\mathrm{h}1}), \\ B_{\mathrm{h}\phi} &= B_{\mathrm{h}0} \cos(p_{\mathrm{h}0}) + B_{\mathrm{h}1} \cos(p_{\mathrm{h}1}) \cos(\phi - \beta_{\mathrm{h}1}), \\ B_{\mathrm{h}z} &= 0, \end{aligned} \tag{3.26}$$

where p_m is the pitch angle of the total horizontal magnetic field, β_m the azimuth at which the corresponding non $m = 0$ mode is a maximum, and h denotes the component of the halo field. The parameter values are given in Table 3.1. For anisotropic fields in the disk, α has been measured to be 1.83 (Houde et al. 2013) while for the halo anisotropic fields it is expected to be less than the disk value owing to weaker spiral density waves and differential rotation in the halo. In our model, the anisotropic factors for the disk and halo are 2.0 and 1.5, respectively.

Table 3.2 shows all the possible model constituents. The model types are constructed based on the following considerations:

1. The total synchrotron intensity (I) increases with the addition of turbulent fields since the ensemble average of the square of the transverse turbulent magnetic field component is non-zero $\left(\left\langle b_\perp^2 \right\rangle \neq 0\right)$. This is also why the total intensity would be non-zero in the absence of any regular fields.

2. Root mean square (rms) values are used for the field strengths of the individual components of the turbulent magnetic fields in the disk and halo. The strength of an individual square component of the field σ_k^2 with $k = \{x, y, \|\}$ is obtained by substituting for σ_r^2 in Eq. (3.3) the normalized input isotropic σ_{I}^2 or anisotropic σ_{A}^2 field strength as $\sigma_r^2 = \sigma_{\mathrm{I}}^2/3$ for isotropy ($\alpha = 1$) and $\sigma_r^2 = \sigma_{\mathrm{A}}^2/(2 + \alpha)$ for anisotropy. For completeness, $\sigma_\phi^2 = \alpha\, \sigma_r^2$. The anisotropic normalization factor in the galaxy plane is conserved upon projection to the sky plane.

3. The diameter of a turbulent cell d_i in the disk or halo is approximately given by (Fletcher et al. 2011)

$$d_i \simeq \left[\frac{D\, \sigma_{RM,D}}{0.81\, \langle n_{\mathrm{e}i} \rangle\, b_{\|i}\, (L_i)^{1/2}} \right]^{2/3}, \tag{3.27}$$

   with $\sigma_{RM,D}$ denoting the RM dispersion observed within a telescope beam of a linear diameter $D = 600$ pc, and $\sigma_{RM,D}$ has been fixed to the observed value of 15 rad m^{-2}.

Table 3.1: Parameters used to model the synchrotron polarization data for an example bin in M51 located in the innermost radial ring (2.4 – 3.6 kpc) at an azimuth centered on 100°.

	Disk	Halo
Mode ratios	$B_2/B_0 = (-33)/(-46)$	$B_{\rm h1}/B_{\rm h0} = (76)/(23)$
p_m [°]	$p_0 = -20$, $p_2 = -12$	$p_{\rm h0} = -43$, $p_{\rm h1} = -45$
β_m [°]	$\beta_2 = -8$	$\beta_{\rm h1} = 44$
$n_{\rm e}$ [cm^{-3}]	0.11	0.01
$n_{\rm cr}$ [cm^{-3}]*	const.	const.
L [pc]	800	5000
d [pc]**	40	240
α	2.0	1.5

Notes: The fitted model parameters appearing in the upper panel for the regular magnetic field of Eq. (3.26) are adopted from Fletcher et al. (2011) with central values reported only. The thermal electron density ($n_{\rm e}$) and path length (L) for the disk and halo are gathered from Fletcher et al. (2011); Berkhuijsen et al. (1997).
$^{(*)}$ The cosmic ray density is treated as a constant of proportionality between the synchrotron emissivity and the square of the total transverse magnetic field (μG) as $\varepsilon = cB_\perp^2$ with constant $c = 0.1$.
$^{(**)}$ The turbulent cell size d in the disk and halo is obtained from Eq. (3.27) with an RM dispersion $\sigma_{RM,D}$ fixed to the observed value of 15 rad m^{-2} within a telescope beam of linear diameter $D = 600$ pc. The rms value for the strength of the turbulent magnetic field along the line of sight $b_\parallel^2 = \sigma_\parallel^2$ has been assumed, where the value for $\sigma_\parallel^2$ is obtained via consideration (2) with $\sigma_{\rm I}^2 = \sigma_{\rm A}^2 = 10\,\mu$G in the disk and $\sigma_{\rm I}^2 = \sigma_{\rm A}^2 = 3\,\mu$G in the halo.

Figures 3.2 - 3.3 constitute a snapshot, at a physically reasonable set of magnetic field values for the disk and halo, of all observationally motivated combinations that may be used to constrain field values for our example bin. The particular magnetic fields underlying these figures involve a total regular disk and halo magnetic field strength of $5\,\mu$G each, an isotropic and anisotropic disk turbulent random field of $\sigma_{\rm I}^2 = \sigma_{\rm A}^2 = 10\,\mu$G for a total disk random field of about $14\,\mu$G, and an isotropic and anisotropic halo turbulent

Table 3.2: Model settings for Figs. 3.2 - 3.4 based on regular and turbulent magnetic field configurations in the disk and halo.

	Disk			Halo		
	Reg.	Iso.	Aniso.	Reg.	Iso.	Aniso.
DH	✓			✓		
DIH	✓	✓		✓		
DAH	✓		✓	✓		
DAIH	✓	✓	✓	✓		
DHI	✓			✓	✓	
DHA	✓			✓		✓
DHAI	✓			✓	✓	✓
DIHI	✓	✓		✓	✓	
DIHI ■	✓	✓		✓	✓	
DIHA	✓	✓		✓		✓
DAHI	✓		✓	✓	✓	
DAHA	✓		✓	✓		✓
DIHAI	✓	✓		✓	✓	✓
DAHAI	✓		✓	✓	✓	✓
DAIHI	✓	✓	✓	✓	✓	
DAIHA	✓	✓	✓	✓		✓
DAIHAI	✓	✓	✓	✓	✓	✓
D	✓					
DI	✓	✓				
DI ★	✓	✓				
DI ■ ★	✓	✓				
DA	✓		✓			
DA ★	✓		✓			
DAI	✓	✓	✓			
DAI ★	✓	✓	✓			
DhI	✓				✓	
DIhI	✓	✓			✓	
DIhI ■	✓	✓			✓	
DIhI ★	✓	✓			✓	
DIhI ■ ★	✓	✓			✓	
DAhI	✓		✓		✓	
DAhI ★	✓		✓		✓	
DAIhI	✓	✓	✓		✓	
DAIhI ★	✓	✓	✓		✓	

Notes: The three column headings below the principle headings of the 'Disk' and 'Halo' denote the regular, isotropic turbulent, and anisotropic turbulent magnetic fields. The rows contain a listing of all model types simulated with the following nomenclature: 'D' denotes disk magnetic fields, 'H' and 'h' both denote halo magnetic fields, 'I' and 'A' are the isotropic and anisotropic turbulent magnetic fields, ■ represents the use of the λ 3.5 cm observations to gauge the wavelength-independent effects, and ★ denotes the use of the generalized opaque-layer approximation to describe the contribution of internal Faraday dispersion (IFD) (in the disk) to depolarization, as detailed in Section 3.6.1. Upper case letters 'D' and 'H' and the lower case 'h' are used to distinguish between the presence or absence of a regular magnetic field in a given layer, respectively. The row ordering follows the model type order as in the legend of Figs. 3.2 and 3.3 for the top panel and that of Fig. 3.4 for the bottom panel.

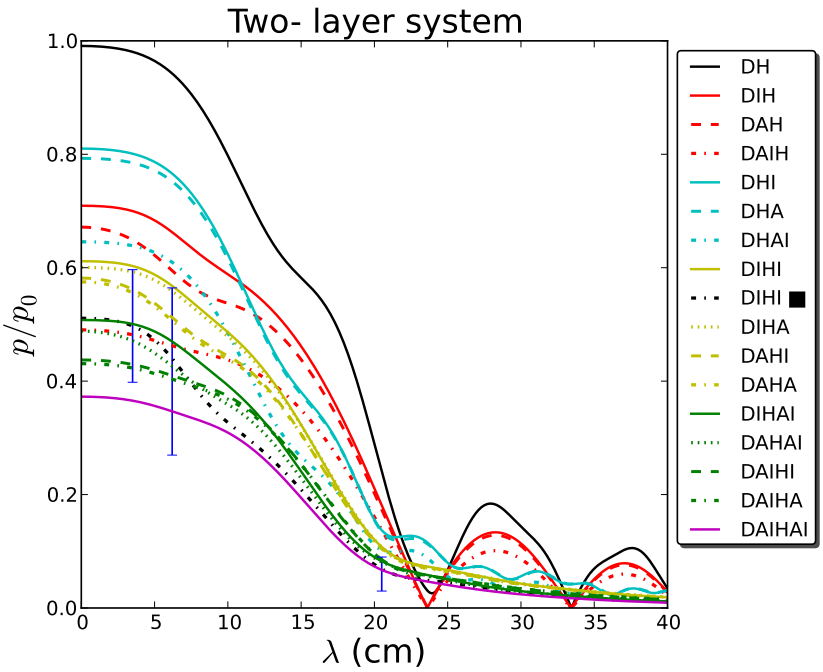

Figure 3.2: Normalized degree of polarization as a function of wavelength for a two-layer system description of M51. The measured polarization values for a sector with an azimuth centered at 100° in radial ring 1 (2.4 – 3.6 kpc) at the three observing wavelengths $\lambda\lambda\lambda$ 3.5, 6.2, 20.5 cm are displayed with error bars. All model profiles featured have been constructed from among the following set of magnetic fields: a total regular field strength of 5 μG in the disk and in the halo, an isotropic and anisotropic disk turbulent random field of 10 μG each, and an isotropic and anisotropic halo turbulent random field of 3 μG each. Please consult Table 3.2 for nomenclature and description of the model types appearing in the legend.

random field of $\sigma_{\rm I}^2 = \sigma_{\rm A}^2 = 3\,\mu$G for a total halo random field of roughly 4 μG. These total turbulent disk and halo magnetic field strengths are used to compute the disk and halo turbulent cell sizes of 40 pc and 240 pc, respectively.

3.6.1 Generalized opaque-layer approximation

We applied a generalized version of an approach, which was used by Berkhuijsen et al. (1997) to provide an approximate description to IFD, in order to predict depolarization values at the three observing wavelengths for M51 and test a method for parametrizing the depolarization, which is most significant at the λ 20.5 cm observing wavelength. The opaque-layer approximation was defined by Sokoloff et al. (1998). It assumes a thermal disk with uniform scale height h_{th}, a synchrotron disk with a wavelength-dependent, uni-

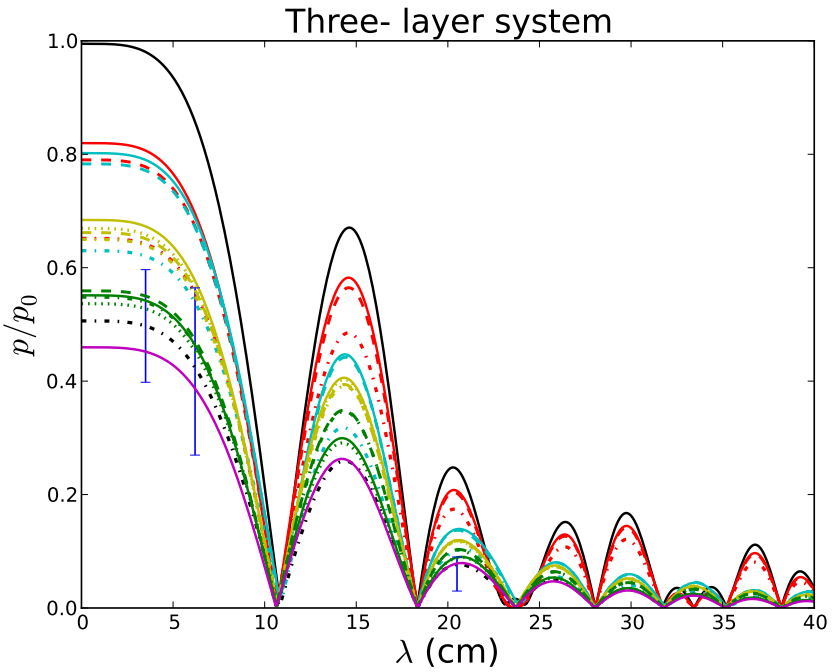

Figure 3.3: Exactly the same model types and physical parameters as used in Fig. 3.2 above but now for a three-layer system.

form scale height h_{syn}, and a thermal halo. Since $h_{syn} > h_{th}$, there is a narrow layer of synchrotron emission extending into the thermal halo. With the assumption that only the nearest part of the synchrotron emitting layer is visible due to depolarization, Berkhuijsen et al. (1997) estimate the contributions to the rotation measure from the disk and from the halo as $\mathrm{RM} = \xi_d\,\mathrm{RM}_d + \xi_h\,\mathrm{RM}_h$, where (ξ_d, ξ_h) parametrize the disk and halo fractional *RM* contribution to the total observed *RM*. The ξ parameters depend on the scale heights of the synchrotron disk and of both the thermal disk and halo and on the relative depolarization between the different observing wavelengths. There may be a variation with radius as well. In particular, the ξ parameter values at $\lambda\lambda\,3.5, 6.2$ cm are close to unity, which implies that there is hardly any change to the actual Faraday depth at these two lower wavelengths.

Fletcher et al. (2011) used the opaque-layer approximation to suppress Faraday rotation by the disk at the longest observing wavelength, while both the disk and halo Faraday rotate the emission at the shorter pair of observing wavelengths. As we are dealing here with a Faraday screen system, we implement either of Eqs. (3.22) or (3.23) and substitute the Faraday depth R in Eq. (3.10) by the *RM* values from Berkhuijsen et al. (1997). To determine the depolarization as predicted by this approximation at the observ-

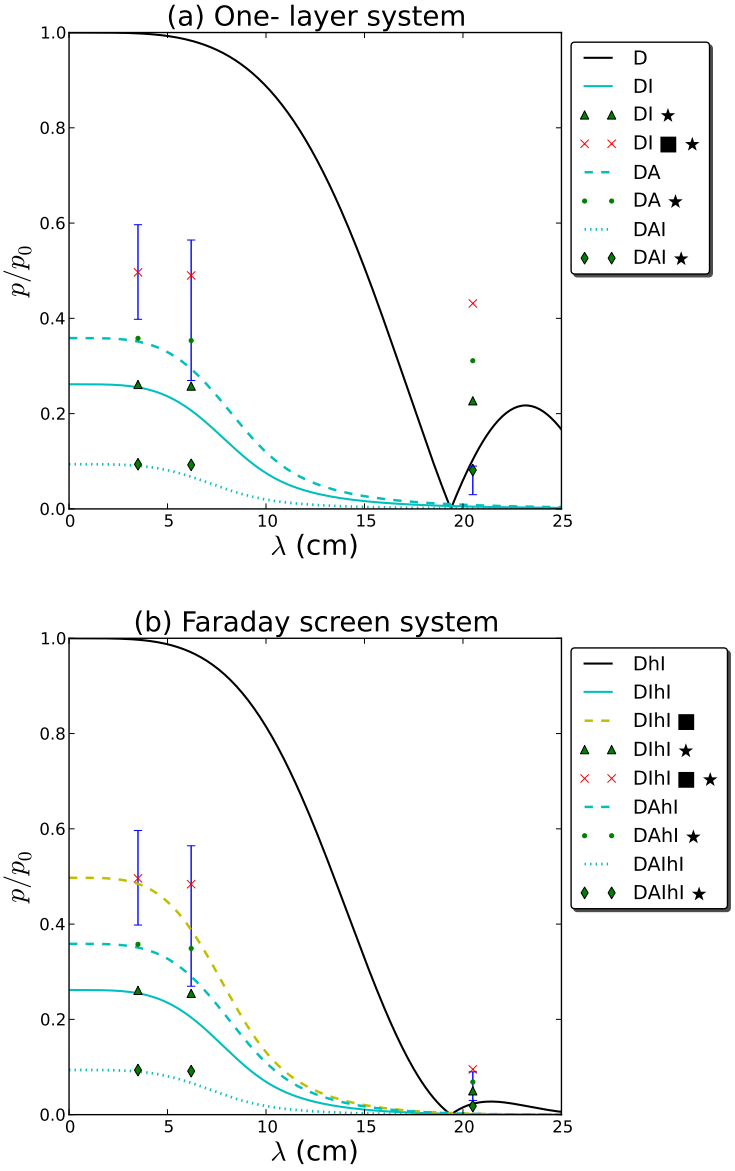

Figure 3.4: Normalized degree of polarization as a function of wavelength with the same physical parameters and nomenclature as in Figs. 3.2 and 3.3. (a) One- layer system with a synchrotron emitting and Faraday rotating disk only. (b) The disk as in (a) but now with a halo that is only Faraday rotating.

ing wavelengths, the scale heights of the synchrotron disk and of both the thermal disk and halo are used from Berkhuijsen et al. (1997), but the relative depolarization are determined from the Fletcher et al. (2011) data. The generalized opaque-layer approximation may be combined with the assumption that all wavelength-independent depolarization effects are calibrated by observations of polarization at the lowest observing wavelength of λ 3.5cm (Berkhuijsen et al. 1997). Comparing Fig. 3.4 (a) with Fig. 3.4 (b) indicates that the presence of a turbulent magnetic field in the halo is required together with both the wavelength-independent gauge and opaque-layer approximation in order to have the best chance of fitting the data for the physically plausible regular and turbulent magnetic fields examined for the disk and halo.

3.7 Discussion and conclusions

The effectiveness of the method in generating a range of models for the diffuse ISM in M51, in terms of the number of magneto-ionic layers modeled and type of magnetic field species occurring in the disk and halo, is illustrated in Figs. 3.2 - 3.4 for our example bin. With typical parameter values as in Table 3.1, one can immediately rule out models with regular fields only in the disk or in the disk and halo, in agreement with ubiquitous observations of turbulent magnetic fields in spiral galaxies.

Even though the modeled magnetic field strengths can be varied for individual models in order to match the data values, the variation in the degree of polarization predicted by the range of models is much greater than the errors in the observed degree of polarization. This gives confidence that observations like these can indeed be used to rule out at least some of the depolarization models.

These models contain many potentially free parameters, which will mean the optimum solutions will be degenerate, however many of the parameters, specifically those in Table 3.1, can be constrained using prior studies. The remaining free parameters are the regular field strengths and isotropic and anisotropic turbulent field strengths, both in the disk and halo.

For these values to be well determined, a sufficient number of data points are needed. For the data from Fletcher et al. (2011), containing only three wavelengths, data in one bin only (as shown in Figs. 3.2 - 3.4) cannot constrain the magnetic field strengths sufficiently. However, some additional assumptions about these field strengths can break the degeneracy. For example, we show in Paper II that the assumption of magnetic field strengths being independent of azimuth provides enough constraints to determine the regular and turbulent magnetic field strengths. With the broadband capabilities of most current radio interferometers, these depolarization curves can be sampled extremely well in wavelength space, with higher sensitivity, thus allowing actual tracing of these depolarization curves.

Throughout the chapter, we have assumed a p_0 of 70% corresponding to the theoretical injection spectrum for electrons accelerated in supernova remnants ($\alpha_{syn} = -0.5$), as representative of the synchrotron spectral index α_{syn} in the spiral arms of M51 (Fletcher et al. 2011). For realistic, optically thin astrophysical plasmas, such as disks and halos of galaxies, p_0 ranges from 60% to 80% (Ginzburg & Syrovatskii 1965, Section 3.3).

Fletcher et al. (2011) estimated a constant p_0 of 76% across M51 ($\alpha_{syn} = -1.1$) but observed variations in this value. This would imply that our current reported values of p/p_0 at the three observing wavelengths are, on the whole, 8% higher than the expected polarization value. However, this overestimate is small compared to the 20% to 50% margin of error in the observations at each of the three observing wavelengths. With better data having errors of only a few percent, the spectral index maps of Fletcher et al. (2011, Fig.7) would have to be binned in the same way as the polarization maps, and the resulting p_0 value per bin would have to be used.

In general, an anisotropic field has a higher degree of polarization than an isotropic field when comparing fields of equal total strength. The greater the anisotropic α term, the higher the polarization. The anisotropic and isotropic turbulent components are presently modeled as yielding two independent depolarization contributions in separate parts of the medium with the strength of IFD determined by the total turbulent field. The next step in modeling would be to include an anisotropic random component in the complete medium and to modify σ_{RM} to reflect an angular dependence in the presence of the anisotropic field. Moreover, if a non-constant spectral index were to be considered, then the effect of (spatial) spectral variation on polarization would have to be accounted for (Burn 1966; Gardner & Whiteoak 1966). The purpose of this work is not to arrive at exact equations for depolarization that are able to incorporate the effects of a greater number of depolarization mechanisms but rather to offer a useful approach to modeling and deducing certain physical parameters of the magneto-ionic medium being analyzed from its polarized emission.

We have shown that various models of depolarization in the disk and halo give widely differing predictions for depolarization at various wavelengths, making them a useful tool for estimating the disk's and halo's regular and turbulent magnetic fields. Our method incorporates depolarizing effects in the disk and halo directly and allows for simultaneous depolarization contributions from DFR and IFD. We also treated depolarization due to anisotropic turbulent fields, albeit with simplifying assumptions described earlier. Modeling the disk and halo as both a two- and three-layer synchrotron emitting and Faraday rotating system allows for the depolarization contribution of the far side of the halo to be examined. A model of the galaxy's regular field is required as an input. The multilayer modeling approach with the inclusion of anisotropic turbulent magnetic fields is found to be a more suitable prescription for the data. For the two-layer system where the halo functions as a Faraday screen, the opaque-layer approximation may work under certain circumstances, but not always. This may be due to oversimplification of the model and/or a lack of a synchrotron halo in the model.

Our method is more robust than the opaque-layer approximation because it is based on more fundamental physical parameters of the galaxy rather than on a wavelength-dependent synchrotron scale height parametrization. We modeled the effects of wavelength-independent and wavelength-dependent depolarization directly, which allowed for a statistical comparison with the polarization maps at the observing wavelengths. The different models provide different enough results that existing multiwavelength observations of nearly face-on galaxies can distinguish between them.

Acknowledgements

CS would like to express his gratitude to Huub Röttgering for his generous time and most supportive supervision. CS and MH acknowledge the support of research program 639.042.915, which is partly financed by the Netherlands Organization for Scientific Research (NWO). AF and AS thank the Leverhulme trust for financial support under grant RPG-097. We are grateful to the anonymous referee for the prompt and most helpful comments and suggestions for strengthening the published paper.

3.A Derivation of wavelength-independent depolarization equations for standard and equipartition scalings of emissivity

We derive the results of Sokoloff et al. (1998) for wavelength-independent depolarization to explicitly show how the corresponding equations arise for two different scalings of emissivity along with the independence of the intrinsic polarization angle from these scalings. We also correct two slight errors in the formula for emissivity given in Sokoloff et al. (1998) for the case of energy equipartition.

For a total magnetic field that is purely a regular (mean) field, $\boldsymbol{B} = \overline{\boldsymbol{B}}$, the complex *intrinsic* (hence wavelength-independent) polarization $\mathcal{P}_{0i}$ per layer i is given by

$$\mathcal{P}_{0i} = p_0 \, \exp\left(2\mathrm{i}\psi_{0i}\right), \tag{3.28}$$

where p_0 is the intrinsic degree of polarization, and ψ_{0i} is the initial polarization angle per layer i.

In the presence of a turbulent magnetic field $\boldsymbol{b}$, the total field becomes $\boldsymbol{B} = \overline{\boldsymbol{B}} + \boldsymbol{b}$ and, together with a sufficiently large number of correlation cells encompassed by the telescope beam cylinder, the volume average in the synchrotron emitting source becomes equal to the ensemble average via the ergodic hypothesis, and $\mathcal{P}_{0i}$ is modified from the above Eq. (3.28) to what is given by Eq. (3.12)

$$\langle \mathcal{P}_{0i} \rangle = p_0 \frac{\langle \varepsilon_i \, \exp\left(2\mathrm{i}\,\psi_{0i}\right) \rangle}{\langle \varepsilon_i \rangle}, \tag{3.29}$$

where ε_i is the synchrotron emissivity and $\langle \ldots \rangle$ denotes ensemble averaging. This expectation value entails computing various moments of the total magnetic field components.

To determine how the intrinsic polarization value p_0 has been modified, in effect, by the presence of turbulence to a layer dependent value p_{0i} (p_0 itself remains constant and equal to 0.7), the quantity $|\langle \mathcal{P}_{0i} \rangle| \, / \, p_0$ has to be evaluated.

Assuming that the total magnetic field is a random Gaussian variable, a Taylor expansion of the moment-generating function M for a normal or Gaussian distributed random variable X defined as

$$M_X(s) = \exp\left(s\mu + \tfrac{1}{2}\,\sigma^2\, s^2\right) \tag{3.30}$$

is performed about $s = 0$ to yield equations for m_n, the n^{th} moment of M_X, at each n^{th} derivative of the function. Therefore, m_n is to be identified with $\langle X^n \rangle$.

The explicit computation of moments of M_X in Eq. (3.30) may be explained as follows. For a given layer i, whether disk or halo, substitute X by the successive components of the total field $\boldsymbol{B}$, which is a random variable because it is the sum of a regular and random variable, and replace s with appropriate instances of the three spatial directions in Cartesian coordinates x, y, z. Then identify μ as an instance of the mean $\overline{B}_{x,y,z}$ and σ^2 as an instance of the variance[2] $\sigma^2_{x,y,z}$ of the corresponding components of $\boldsymbol{b}$.

For completeness, the first through fourth moments are

$$\begin{aligned} m_1 &= \mu, \\ m_2 &= \mu^2 + \sigma^2, \\ m_3 &= \mu^3 + 3\,\mu\,\sigma^2, \\ m_4 &= \mu^4 + 3\,\sigma^4 + 6\,\mu^2\,\sigma^2. \end{aligned}$$

For the case of a purely random field, $\mu = 0$ leaving only the even (central) moments m_2 and m_4. For the case of a purely regular field, $\sigma = 0$ and the four moments simply reduce to the first through fourth powers of the mean field.

Assuming that the emissivity per layer i scales as

$$\varepsilon_i = c\,B^2_{\perp i}, \tag{3.31}$$

the complex emissivity is, therefore, given by

$$\varepsilon_i\,\exp\left(2\mathrm{i}\,\psi_{0i}\right) = c\,(B^2_{xi} - B^2_{yi} + 2\mathrm{i}\,B_{xi}\,B_{yi}), \tag{3.32}$$

where $B_{\perp i} = B_{xi} + \mathrm{i}B_{yi}$, $B^2_{\perp i} = |B_{\perp i}|^2 = B^2_{xi} + B^2_{yi}$, and c is a constant depending on the number density of relativistic cosmic ray electrons n_{cr}. Taking the square of each of the two equivalent representations of a complex number z as given by $R\exp(\mathrm{i}\theta) = z = x + \mathrm{i}y$, with $R = |x + \mathrm{i}y|$ and $\tan\theta = \mathrm{Im}(z)\,/\,\mathrm{Re}(z) = y/x$ and identifying the coordinates x, y with B_{xi}, B_{yi} may serve as an aid in arriving at Eq. (3.32).

The absolute value of Eq. (3.29) with the emissivity scaling of Eq. (3.31) therefore yields the following equation for the wavelength-independent depolarization as in Eq. (3.13) and as in Eq. (19) of Sokoloff et al. (1998).

$$\frac{|\langle \mathcal{P}_{0i} \rangle|}{p_0} = \left\{ \frac{\left[\left(\overline{B}^2_x - \overline{B}^2_y + \sigma^2_x - \sigma^2_y \right)^2 + 4\overline{B}^2_x \overline{B}^2_y \right]^{1/2}}{\overline{B^2_\perp}} \right\}_i ,$$

where $\overline{B}^2_\perp = \overline{B}^2_x + \overline{B}^2_y$, $\overline{B^2_\perp} = \overline{B}^2_\perp + \sigma^2_x + \sigma^2_y$.

[2] The variance of a complex random variable X is given by:
$\sigma^2_X = \langle (X - \langle X \rangle)\,(X^* - \langle X^* \rangle) \rangle = \langle X\,X^* \rangle - \langle X \rangle\,\langle X^* \rangle$, where the asterisk denotes the complex conjugate.

The intrinsic polarization angle is also modified and obtained from the ratio of imaginary to real parts of the expectation value of the complex emissivity via $\tan(2\langle\psi_{0i}\rangle) = \mathrm{Im}(\langle\text{Eq. (3.32)}\rangle) \,/\, \mathrm{Re}(\langle\text{Eq. (3.32)}\rangle)$ and is therefore given by

$$\langle\psi_{0i}\rangle = \tfrac{1}{2}\pi + \tfrac{1}{2}\arctan\left(\frac{2\overline{B}_x\overline{B}_y}{\overline{B}_x^2 - \overline{B}_y^2 + \sigma_x^2 - \sigma_y^2}\right)_i \tag{3.33}$$

as in Eq. (3.5) without the sky-plane coordinate transformation term and as in Eq. (20) of Sokoloff et al. (1998).

With the energy equipartition and pressure equilibrium assumptions the cosmic ray number density scales as $n_{cr} \propto B^2$ if the energy densities of magnetic fields and cosmic rays are completely correlated, and the scaling of synchrotron emissivity with magnetic field becomes

$$\varepsilon_i = C\, B_i^2\, B_{\perp i}^2 \tag{3.34}$$

with a certain constant C, therefore

$$\varepsilon_i\, \exp(2\mathrm{i}\,\psi_{0i}) \;=\; C\, B_i^2\, (B_{xi}^2 - B_{yi}^2 + 2\mathrm{i}\, B_{xi}\, B_{yi}), \tag{3.35}$$

where $B_i^2 = B_{xi}^2 + B_{yi}^2 + B_{zi}^2$. The intrinsic polarization angles are *unaffected* by the rescaling of emissivity since the constant term CB_i^2 cancels out, exactly like the c term, in arriving at Eq. (3.33). In addition to the first two moments, the third and fourth moments of the fields B_k with $k = \{x, y, z\}$ in Eqs. (3.34) and (3.35) must be computed.

Consequently, the absolute value of Eq. (3.29) transforms to

$$\begin{aligned}\frac{|\langle\mathcal{P}_{0i}\rangle|}{p_0} = &\left[\overline{B^2}\,\overline{B_\perp^2} \;+\; 2\left(\sigma_x^4 + \sigma_y^4\right) \;+\; 4\left(\overline{B}_x^2\,\sigma_x^2 \;+\; \overline{B}_y^2\,\sigma_y^2\right)\right]^{-1} \\ &\times\left\{\left[\overline{B}_x^4 - \overline{B}_y^4 + 3\left(\sigma_x^4 - \sigma_y^4\right) + 6\left(\overline{B}_x^2\,\sigma_x^2 - \overline{B}_y^2\,\sigma_y^2\right)\right.\right. \\ &\left.\left. + \overline{B_\parallel^2}\left(\overline{B_x^2} - \overline{B_y^2}\right)\right]^2 + 4\overline{B}_x^2\overline{B}_y^2\left[\overline{B^2} + 3\left(\sigma_x^2 + \sigma_y^2\right)\right]^2\right\}^{1/2},\end{aligned} \tag{3.36}$$

where the righthand side of the above equation is to be taken per individual layer i, disk or halo, $\overline{B_\parallel^2} = \overline{B}_\parallel^2 + \sigma_\parallel^2$ and $\overline{B^2} = \overline{B_\perp^2} + \overline{B_\parallel^2}$. Isotropy is now given by $\sigma_x = \sigma_y = \sigma_\parallel = \sigma$. The form of Eq. (3.36) would then imply the corresponding modification in Eqs. (3.13) - (3.15). The simple multiplicative relationship between the wavelength-dependent and wavelength-independent terms as represented in Eq. (3.9) would continue to hold only if no dependence on the line-of-sight coordinate arose.

3.B Symmetries and equation properties

Symmetry considerations are appropriate for discussion in the context of depolarization. Layer *ordering* and line-of-sight magnetic field *reversal* are two distinct symmetries that arise in our modeling. Layer ordering involves a reflection of the physical system or the placement of the observer at the opposite end of the originally oriented system. For a two-layer medium this simply involves an exchange of the index i that also causes $\Delta\psi_{dh} \rightarrow -\Delta\psi_{dh}$. For a three-layer system, with identical far and near sides of the halo, reflection is automatically satisfied. For magnetic field reversal along the line of sight, only the direction of the line-of-sight *regular* field has to be reversed $\overline{B}_z \rightarrow -\overline{B}_z$, in all layers at once, since a change of sign for turbulent fields has no affect on polarization.

With only DFR present, the equation for depolarization in a two-layer system, given by Eq. (3.18), indicates that the presence of the $\Delta\psi$ term breaks each of the ordering and reversal symmetries but that symmetry is preserved only if both layer ordering and field reversal are applied *simultaneously*. A three-layer system remains invariant under field reversal as apparent from Eq. (3.20).

IFD occurring with DFR changes the previously encountered symmetry properties for DFR alone in terms of layer ordering and field reversal for a two- and three-layer system. In particular, it is always the cross terms (which mix the layers) that determine these symmetries. A two-layer system given by Eq. (3.24) remains invariant under the line-of-sight regular magnetic field sign inversion only when the disk and halo intrinsic polarization angles are equal ($\Delta\psi_{dh} = 0$) just as for the two-layer system with DFR alone. However, the IFD 'carrier' σ_{RM} terms break the previously achieved layer ordering symmetry so that the two-layer system becomes sensitive to whether the far or near side of the halo is switched on alongside the disk. For a three-layer system given by Eq. (3.25), the presence of IFD now imposes the extra condition that the disk and halo intrinsic polarization angles must be equal in order to have the field reversal symmetry as for the two-layer system. For a Faraday screen system, Eq. (3.22) remains *symmetric* under the reversal of the total magnetic field direction along the line of sight $B_z \rightarrow -B_z$. When the symmetries are broken, the amplitude and period are only slightly affected for our example bin. Both of the three-layer Eqs. (3.25) and (3.20) contain a non-trivial $\left(1 + \cos\left(2\,(R_d + R_h)\,\lambda^2\right)\right)$ term that contains the combined actions of the disk and near halo regular fields and arises from the near and far sides of the halo being set identically equal.

3.C General expression for wavelength-dependent depolarization for a three-layer system

For completeness, we provide the general expression for depolarization in three *distinct* layers with differential Faraday rotation (DFR) and internal Faraday dispersion (IFD) occurring concomitantly in each layer.

$$
\begin{aligned}
\left(\frac{p}{p_0}\right)_{3layer} = \Bigg| & \frac{\langle \mathcal{P}_{01} \rangle}{p_0} \frac{I_1}{I} \left[\frac{1 - e^{\left(-2\sigma_{RM_1}^2 \lambda^4 + 2\,\mathrm{i}\, R_1 \lambda^2\right)}}{2\sigma_{RM_1}^2 \lambda^4 - 2\,\mathrm{i}\, R_1 \lambda^2} \right] e^{2\mathrm{i}\left[\psi_{01} + (R_2 + R_3)\lambda^2\right]} \\
& + \frac{\langle \mathcal{P}_{02} \rangle}{p_0} \frac{I_2}{I} \left[\frac{1 - e^{\left(-2\sigma_{RM_2}^2 \lambda^4 + 2\,\mathrm{i}\, R_2 \lambda^2\right)}}{2\sigma_{RM_2}^2 \lambda^4 - 2\,\mathrm{i}\, R_2 \lambda^2} \right] e^{2\mathrm{i}\left(\psi_{02} + R_3 \lambda^2\right)} \\
& + \frac{\langle \mathcal{P}_{03} \rangle}{p_0} \frac{I_3}{I} \left[\frac{1 - e^{\left(-2\sigma_{RM_3}^2 \lambda^4 + 2\,\mathrm{i}\, R_3 \lambda^2\right)}}{2\sigma_{RM_3}^2 \lambda^4 - 2\,\mathrm{i}\, R_3 \lambda^2} \right] e^{2\mathrm{i}\,\psi_{03}} \Bigg| \\
= \Bigg\{ & W_1^2 \left(\frac{I_1}{I}\right)^2 \left(\frac{1 - 2e^{-A}\cos D + e^{-2A}}{A^2 + D^2} \right) \\
& + W_2^2 \left(\frac{I_2}{I}\right)^2 \left(\frac{1 - 2e^{-B}\cos E + e^{-2B}}{B^2 + E^2} \right) \\
& + W_3^2 \left(\frac{I_3}{I}\right)^2 \left(\frac{1 - 2e^{-C}\cos F + e^{-2C}}{C^2 + F^2} \right) \\
& + W_1 W_2 \frac{I_1 I_2}{I^2} \frac{2}{M^2 + N^2} \Big[\{M, N\}\,(2\Delta\psi_{12} + E) \\
& + e^{-(A+B)}\,\{M, N\}\,(2\Delta\psi_{12} + D) \\
& - e^{-A}\,\{M, N\}\,(2\Delta\psi_{12} + D + E) \\
& - e^{-B}\,\{M, N\}\,(2\Delta\psi_{12}) \Big] \\
& + W_2 W_3 \frac{I_2 I_3}{I^2} \frac{2}{S^2 + T^2} \Big[\{S, T\}\,(2\Delta\psi_{23} + F) \\
& + e^{-(B+C)}\,\{S, T\}\,(2\Delta\psi_{23} + E) \\
& - e^{-B}\,\{S, T\}\,(2\Delta\psi_{23} + E + F) \\
& - e^{-C}\,\{S, T\}\,(2\Delta\psi_{23}) \Big] \\
& + W_1 W_3 \frac{I_1 I_3}{I^2} \frac{2}{U^2 + V^2} \Big[\{U, V\}\,(2\Delta\psi_{13} + E + F) \\
& + e^{-(A+C)}\,\{U, V\}\,(2\Delta\psi_{13} + D + E)
\end{aligned}
$$

$$- e^{-A}\{U,V\}(2\Delta\psi_{13} + D + E + F)$$
$$- e^{-C}\{U,V\}(2\Delta\psi_{13} + E)\Big]\Big\}^{1/2}, \tag{3.37}$$

where $A = 2\sigma^2_{RM_1}\lambda^4$, $B = 2\sigma^2_{RM_2}\lambda^4$, $C = 2\sigma^2_{RM_3}\lambda^4$, $D = 2R_1\lambda^2$, $E = 2R_2\lambda^2$, $F = 2R_3\lambda^2$ with the index subscript $i = 1, 2, 3$ labeling the far halo, disk, and near halo, respectively. Furthermore, $M = AB + DE$, $N = BD - AE$, $S = BC + EF$, $T = CE - BF$, $U = AC + DF$, $V = CD - AF$, $\Delta\psi_{ij} = \psi_{0i} - \psi_{0j}$ for layers (i, j), and $\{X, Y\}(a) = X\cos(a) - Y\sin(a)$ for general variables X, Y and argument a. σ_{RM_i} denotes the dispersion of the intrinsic rotation measure RM within the volume of the telescope beam and is given by Eq. (3.11) and R_i is the total Faraday depth given by Eq. (3.10) with both quantities taken per layer i. The $\langle\mathcal{P}_{0i}\rangle$ are defined in Eq. (3.12) and the W_i are the generic wavelength-independent depolarizing terms discussed in section 3.4. This expression naturally reduces to Eq. (3.25) for identical far and near halos upon setting $i = 1 = 3$.

Finally, we remark that for an n-layer system, with each layer distinct, the total number of terms following the second equal sign of Eq. (3.37) would be given by $n + 8\binom{n}{2}$; the sum of direct squared terms given by the number of layers, n, and all cross terms that mix the layers, $8\binom{n}{2}$, where n choose 2 is the total number of unique pairs of layers and the 8 comes from the four new term types per layer appearing inside the large square brackets, with each of these terms being multiplied by a sum of a sine and cosine term as contained in the operation $\{X, Y\}$. The pattern of the terms after the second equality in the above expression, in the context of increasing layer number, is straightforward in the first three direct terms and emerges in the three groupings of cross terms, each of which consists of four distinct terms inside the large square brackets. Labeling the cross terms by the pairings of the emissivities $I_{i,j}$, it is readily observed that the arguments inside the square brackets of $I_{1,2}$ and $I_{2,3}$ have the same characteristics and combine in the same manner. That this is also the underlying property for $I_{1,3}$, which is a 'long-range' grouping as it spans the entire medium, may by seen upon setting the middle layer as $E = 0$. We identify these characteristics to hold for all 'nearest-neighbor' layers, as $I_{1,2}$ and $I_{2,3}$, with longer distance neighboring layer pairings (D and F are the endpoints) containing the additional terms of the layers between them in place of the E term. Thus proceeding, the direct and cross terms for an n-layer system may be explicitly derived.

Bibliography

Alfvén, H. & Herlofson, N. 1950, Physical Review, 78, 616
Berkhuijsen, E. M., Horellou, C., Krause, M., et al. 1997, A&A, 318, 700
Brentjens, M. A. & de Bruyn, A. G. 2005, A&A, 441, 1217B
Burn, B. J. 1966, MNRAS, 133, 67
Chadderton, R. 2011, MSc Thesis Newcastle University
Fletcher, A., Beck, R., Shukurov, A., Berkhuijsen, E. M., & Horellou, C. 2011, MNRAS, 412, 2396
Gardner, F. F. & Whiteoak, J. B. 1966, ARA&A, 4, 245
Ginzburg, V. L. & Syrovatskii, S. I. 1965, ARA&A, 3, 297
Heiles, C. 1996, in Astronomical Society of the Pacific Conference Series, Vol. 97, Polarimetry of the Interstellar Medium, ed. W. G. Roberge & D. C. B. Whittet, 457
Houde, M., Fletcher, A., Beck, R., et al. 2013, ApJ, 766, 49
Jaffe, T. R., Leahy, J. P., Banday, A. J., et al. 2010, MNRAS, 401, 1013
Jansson, R. & Farrar, G. R. 2012, ApJ, 761, L11
Korchakov, A. A. & Syrovatskii, S. I. 1962, Soviet Ast., 5, 678
Sokoloff, D. D., Bykov, A. A., Shukurov, A., et al. 1998, MNRAS, 299, 189
Sokoloff, D. D., Bykov, A. A., Shukurov, A., et al. 1999, MNRAS, 303, 207
Tribble, P. C. 1991, MNRAS, 250, 726
Zweibel, E. G. & Heiles, C. 1997, Nature, 385, 131

4

Constraining regular and turbulent magnetic field strengths in M51 via Faraday depolarization

C. Shneider, M. Haverkorn, A. Fletcher, A. Shukurov

Astronomy & Astrophysics, Volume 568, A83 (2014)

Abstract

We employ an analytical model that incorporates both wavelength-dependent and wavelength-independent depolarization to describe radio polarimetric observations of polarization at $\lambda\lambda\lambda\, 3.5, 6.2, 20.5$ cm in M51 (NGC 5194). The aim is to constrain both the regular and turbulent magnetic field strengths in the disk and halo, modeled as a two- or three-layer magneto-ionic medium, via differential Faraday rotation and internal Faraday dispersion, along with wavelength-independent depolarization arising from turbulent magnetic fields. A reduced chi-squared analysis is used for the statistical comparison of predicted to observed polarization maps to determine the best-fit magnetic field configuration at each of four radial rings spanning 2.4 – 7.2 kpc in 1.2 kpc increments. We find that a two-layer modeling approach provides a better

fit to the observations than a three-layer model, where the near and far sides of the halo are taken to be identical, although the resulting best-fit magnetic field strengths are comparable. This implies that all of the signal from the far halo is depolarized at these wavelengths. We find a total magnetic field in the disk of approximately 18 μG and a total magnetic field strength in the halo of $\sim 4-6\,\mu$G. Both turbulent and regular magnetic field strengths in the disk exceed those in the halo by a factor of a few. About half of the turbulent magnetic field in the disk is anisotropic, but in the halo all turbulence is only isotropic.

4.1 Introduction

Magnetic fields are important drivers of dynamical processes in the interstellar medium (ISM) of galaxies on both large and small scales. They regulate the density and distribution of cosmic rays in the ISM (Beck 2004) and couple with both charged and, through ion-neutral collisions, neutral particles in essentially all interstellar regions except for the densest parts of molecular clouds (Ferrière 2001). Moreover, their energy densities are comparable to the thermal and turbulent gas energy densities on large scales, as indicated for the spiral galaxies NGC 6946 and M33 and for the Milky Way (Beck 2007; Tabatabaei et al. 2008; Heiles & Haverkorn 2012), thereby affecting star formation and the flow of gas in spiral arms and around bars (Beck 2009, 2007, and refs. therein). In the case of the Galaxy, magnetic fields contribute to the hydrostatic balance and stability of the ISM on large scales, while they affect the turbulent motions of supernova remnants and superbubbles on small scales (Ferrière 2001, and refs. therein). Knowledge of the strength and structure of magnetic fields is therefore paramount to understanding ISM physics in galaxies.

Multiwavelength radio-polarimetric observations of diffuse synchrotron emission in conjunction with numerical modeling is a way of probing magnetic field interactions with cosmic rays and the diffuse ISM in galaxies. Of particular interest are the total magnetic field and its regular and turbulent components, as well as their respective contributions to both wavelength-dependent and wavelength-independent depolarization in the thin and thick gaseous disk (hereafter the disk and halo).

Physically, regular magnetic fields are produced by dynamo action, anisotropic random fields from compression and shearing gas flows, and isotropic random fields by supernovae and other sources of turbulent gas flows. In the presence of magnetic fields, cosmic ray electrons emit linearly polarized synchrotron radiation. Polarization is attributable only to the ordered magnetic fields, while unpolarized synchrotron radiation stems from disordered magnetic fields. The degree of polarization p, defined as the ratio of polarized synchrotron to total synchrotron intensity, thus characterizes the magnetic field content and may be used as an effective modeling constraint.

Except for edge-on galaxies, where the disk and halo are spatially distinct in projection to the observer, disentangling contributions to depolarization from the disk and halo is challenging. In this chapter, we apply the theoretical framework developed in Chap. 3

to numerically simulate the combined action of depolarization mechanisms in two or three consecutive layers describing a galaxy's disk and halo to constrain the regular and turbulent disk and halo magnetic field strengths in a face-on galaxy.

In particular, M51 (NGC 5194) is ideally suited to studying such interactions for several reasons: (i) small angle of inclination ($l = -20°$) permits the assumption of a multilayer decomposition into disk and halo components along the line of sight, (ii) high galactic latitude (b = +68.6°) facilitates polarized signal extraction from the total synchrotron intensity since the contribution from the Galactic foreground is negligible at those latitudes (Berkhuijsen et al. 1997), and (iii) proximity of 7.6 Mpc allows for a high spatial resolution study. Besides a regular, large-scale magnetic field component and an isotropic random, small-scale field, the presence of an anisotropic random field component is expected since there is no large-scale pattern in Faraday rotation accompanying M51's magnetic spiral pattern observed in radio polarization (Fletcher et al. 2011). Additionally, M51's galaxy type (Sc), linear dimension, and ISM environment are comparable with that of the Milky Way (Mao et al. 2012), (see also Pavel & Clemens (2012) for near infrared (NIR) polarimetry), possibly allowing for the nature of the global magnetic field properties of our own Galaxy to be further elucidated.

4.2 Observational data

We use the Fletcher et al. (2011) $\lambda\lambda\lambda$ 3.5, 6.2, 20.5 cm continuum polarized and total synchrotron intensity observations of M51, taken with the VLA and Effelsberg and smoothed with a 15″ beam resolution, to construct degree of polarization p maps. The p maps are partitioned into four radial rings from 2.4 – 7.2 kpc in 1.2 kpc increments with every ring further subdivided into 18 azimuthal sectors, each with an opening angle of 20°, following Fletcher et al. (2011). We will call these rings 1 through 4 from the innermost to the outermost ring. This results in a total of 72 bins. In the outermost ring, two of the bins are excluded as the number of data points within them is too small (less than five). For each of the remaining bins, histograms are produced to check that the individual distributions are more or less Rician and the mean of p is computed with the standard deviation of p taken as the error. Thermal emission subtraction was done using a constant thermal emission fraction across the Galaxy (Fletcher et al. 2011). In this method, thermal emission may have possibly been underestimated in the spiral arms in the Fletcher et al. (2011) total synchrotron intensity maps, the values of p may, consequently, be overestimated in the bins that contain the spiral arms.

4.3 Model

4.3.1 Regular field

Following Fletcher et al. (2011), we use a two dimensional regular magnetic field $\sum_m \boldsymbol{B}_m(r)\cos(m\phi - \beta_m)$ for both the disk and halo with integer mode number m and

azimuthal angle in the galaxy plane ϕ, measured counterclockwise from the northern end of the major axis along M51's rotation. A superposition of axisymmetric modes ($m = 0, 2$) describes the disk magnetic field while mainly a bisymmetric mode ($m = 1$) describes the halo magnetic field. These modes yield the individual amplitudes B_m, pitch angles[1] p_m and β_m angles[2].

The regular disk and halo magnetic fields in cylindrical polar coordinates are

$$\begin{aligned}
B_r &= B_0 \sin(p_0) + B_2 \sin(p_2) \cos(2\phi - \beta_2), \\
B_\phi &= B_0 \cos(p_0) + B_2 \cos(p_2) \cos(2\phi - \beta_2), \\
B_z &= 0, \\
B_{\mathrm{h}r} &= B_{\mathrm{h}0} \sin(p_{\mathrm{h}0}) + B_{\mathrm{h}1} \sin(p_{\mathrm{h}1}) \cos(\phi - \beta_{\mathrm{h}1}), \\
B_{\mathrm{h}\phi} &= B_{\mathrm{h}0} \cos(p_{\mathrm{h}0}) + B_{\mathrm{h}1} \cos(p_{\mathrm{h}1}) \cos(\phi - \beta_{\mathrm{h}1}), \\
B_{\mathrm{h}z} &= 0,
\end{aligned} \tag{4.1}$$

where h denotes the component of the halo field. Please consult Table 4.1 for the associated magnetic field parameters in Eq. (4.1) and see Fig.14 of Fletcher et al. (2011) for an illustration of their best-fit disk and halo modes. An anomalous halo pitch angle of $-90°$ for the outermost ring was deemed unphysical and probably arose owing to the low polarization degrees in this ring. Therefore, we ignore this value and instead use $-50°$, the pitch angle in the adjacent ring.

Our model inputs only the regular magnetic field *directions*, described by the respective modes for the disk and halo in Eq. (4.1), along with the relative strengths of these modes, given by B_2/B_0 and B_{h1}/B_{h0} in Table 4.1, while the regular disk and halo magnetic field *strengths* are allowed to vary.

The components of the regular magnetic field are projected onto the sky-plane (Berkhuijsen et al. 1997) as

$$\begin{aligned}
\overline{B}_x &= B_r \cos(\phi) \; - \; B_\phi \sin(\phi), \\
\overline{B}_y &= \Big[B_r \sin(\phi) \; + \; B_\phi \cos(\phi) \Big] \cos(l) + B_z \sin(l), \\
\overline{B}_\parallel &= - \Big[B_r \sin(\phi) \; + \; B_\phi \cos(\phi) \Big] \sin(l) + B_z \cos(l),
\end{aligned}$$

where l is the inclination angle and $\parallel$ denotes a component of the field parallel to the line of sight.

4.3.2 Turbulent field

We explicitly introduce three-dimensional turbulent magnetic fields with both isotropic and anisotropic components. The random magnetic fields are expressed as the standard

[1] The pitch angle of the total horizontal magnetic field is given by $\arctan\left(B_r/B_\phi\right)$ per mode m. Hence, $\sin(p_m)$ and $\cos(p_m)$ correspond to the B_r and B_ϕ components of $\boldsymbol{B}$, respectively.

[2] The β angle is the azimuth at which the corresponding $m \neq 0$ mode is a maximum.

Table 4.1: Fitted Model Parameters adopted from Fletcher et al. (2011, Table A1). Ratios of mode strengths are reported as this allows for the magnetic field strengths to be left as a variable parameter in our model.

	Ring 1	Ring 2	Ring 3	Ring 4
r [kpc]	[2.4, 3.6]	[3.6, 4.8]	[4.8, 6.0]	[6.0, 7.2]
B_2/B_0	−33/−46	−25/−57	−40/−76	−44/−76
$p_0[^\circ]$	−20	−24	−22	−18
$p_2[^\circ]$	−12	16	8	3
$\beta_2[^\circ]$	−8	−6	−14	−25
B_{h1}/B_{h0}	76/23	...	...	...
$p_{h0}[^\circ]$	−43	...	...	...
$p_{h1}[^\circ]$	−45	−49	−50	-50^a
$\beta_{h1}[^\circ]$	44	30	−3	−16

Notes: The index h refers to the halo magnetic field. Dots mean that the corresponding parameter was insignificant in the Fletcher et al. (2011) fits and is thus not an input in our model.
[(a)] changed from original value of -90° to be in closer agreement with the halo pitch angle value reported for inner three rings.

deviations of the total magnetic field and are given by

$$\begin{aligned}
\sigma_x^2 &= \sigma_r^2 \left[\cos^2(\phi) + \alpha \sin^2(\phi)\right], \\
\sigma_y^2 &= \sigma_r^2 \left\{\left[\sin^2(\phi) + \alpha \cos^2(\phi)\right] \cos^2(l) + \sin^2(l)\right\}, \\
\sigma_\parallel^2 &= \sigma_r^2 \left\{\left[\sin^2(\phi) + \alpha \cos^2(\phi)\right] \sin^2(l) + \cos^2(l)\right\}.
\end{aligned} \tag{4.2}$$

Anisotropy is assumed to exclusively arise from compression along spiral arms and by shear from differential rotation and is assumed to have the form $\sigma_\phi^2 = \alpha \sigma_r^2$ with $\alpha > 1$ and $\sigma_r = \sigma_z$. Isotropy is the case when $\alpha = 1$. For anisotropic disk magnetic fields in M51, α has been measured to be 1.83 by Houde et al. (2013) who measured the random field anisotropy in terms of the correlation scales in the two orthogonal directions (x and y) and not in terms of the strength of the fluctuations in the two directions, as we use. For the halo anisotropic fields, α is expected to be less than the disk value as a result of weaker spiral density waves and differential rotation in the halo. In our model, the disk and halo anisotropic factors are fixed to 2.0 and 1.5, respectively, and are reported in Table 4.2. Root mean square (rms) values are used for individual components of the turbulent magnetic field strengths in the disk or halo by normalizing the square isotropic

Table 4.2: Model Standard Parameters. Thermal electron density (n_e) and path length (L) values are collected from Berkhuijsen et al. (1997) and Fletcher et al. (2011). The parameter α is used to characterize anisotropic turbulent magnetic fields and is discussed in Section 4.3.2.

	n_e [cm^{-3}]	L [pc]	α
Disk Ring 1,2	0.11	800	2.0
Disk Ring 3,4	0.06	1200	2.0
Halo Ring 1,2	0.01	5000	1.5
Halo Ring 3,4	0.006	3300	1.5

σ_I^2 or anisotropic σ_A^2 field strength as $\sigma_r^2 = \sigma_I^2/3$ for isotropy and $\sigma_r^2 = \sigma_A^2/(2 + \alpha)$ for anisotropy in Eq. (4.2).

4.3.3 Densities

The thermal electron density (n_e) is assumed to be a constant at each of the four radial rings and about an order of magnitude smaller in the halo than in the disk. Table 4.2 displays these values along with the respective path lengths through the (flaring) disk and halo. The cosmic ray density (n_{cr}) is assumed to be a global constant throughout the entire galaxy whose actual value is not significant as it cancels out upon computing p. Synchrotron emissivity is described as $\varepsilon = cB_\perp^2$ with constant $c = 0.1$.

4.3.4 Depolarization

We model the wavelength-dependent depolarization mechanisms of differential Faraday rotation (DFR) and internal Faraday dispersion (IFD) concomitantly to account for the presence of regular and turbulent magnetic fields in a given layer together with wavelength-independent depolarization. The combined wavelength-dependent and wavelength-independent depolarization for a two-layer system and three-layer system, with identical far and near sides of the halo, are given by (Chap. 3, Eqs. (3.24), (3.25))

$$\begin{aligned}\left(\frac{p}{p_0}\right)_{2layer} = \Bigg\{ & W_d^2 \left(\frac{I_d}{I}\right)^2 \left(\frac{1 - 2e^{-\Omega_d}\cos C_d + e^{-2\Omega_d}}{\Omega_d^2 + C_d^2}\right) \\ & + W_h^2 \left(\frac{I_h}{I}\right)^2 \left(\frac{1 - 2e^{-\Omega_h}\cos C_h + e^{-2\Omega_h}}{\Omega_h^2 + C_h^2}\right) \\ & + W_d W_h \frac{I_d I_h}{I^2} \frac{2}{F^2 + G^2} \Bigg[\{F, G\}\,(2\Delta\psi_{dh} + C_h) \\ & + e^{-(\Omega_d + \Omega_h)}\,\{F, G\}\,(2\Delta\psi_{dh} + C_d) \\ & - e^{-\Omega_d}\,\{F, G\}\,(2\Delta\psi_{dh} + C_d + C_h)\end{aligned}$$

$$- e^{-\Omega_h} \{F, G\} (2\Delta\psi_{dh}) \Big] \Big\}^{1/2}, \tag{4.3}$$

and

$$\begin{aligned}
\left(\frac{p}{p_0}\right)_{3layer} &= \left(2\, W_h^2 \left(\frac{I_h}{I}\right)^2 \left\{ \left(\frac{1}{\Omega_h^2 + C_h^2}\right) \times \right.\right. \\
&\left(1 - 2e^{-\Omega_h} \cos C_h + e^{-2\Omega_h}\right) \Big[1 + \cos\left(C_d + C_h\right)\Big] \Big\} \\
&+ W_d^2 \left(\frac{I_d}{I}\right)^2 \left(\frac{1 - 2e^{-\Omega_d} \cos C_d + e^{-2\Omega_d}}{\Omega_d^2 + C_d^2}\right) \\
&+ W_d W_h \frac{I_d I_h}{I^2} \frac{2}{F^2 + G^2} \Big\{ \{F, -G\} (-2\Delta\psi_{dh} + C_d) \\
&+ \{F, G\} (2\Delta\psi_{dh} + C_h) \\
&+ e^{-(\Omega_d + \Omega_h)} \Big[\{F, G\} (2\Delta\psi_{dh} + C_d) + \{F, -G\} (-2\Delta\psi_{dh} + C_h) \Big] \\
&- e^{-\Omega_d} \Big[\{F, G\} (2\Delta\psi_{dh} + C_d + C_h) + \{F, -G\} (-2\Delta\psi_{dh}) \Big] \\
&- e^{-\Omega_h} \Big[\{F, -G\} (-2\Delta\psi_{dh} + C_d + C_h) + \{F, G\} (2\Delta\psi_{dh}) \Big] \Big\} \Big)^{1/2},
\end{aligned} \tag{4.4}$$

where p_0 is the intrinsic degree of linear polarization of synchrotron radiation, $\{d, h\}$ denote the disk and halo, $\Omega_d = 2\sigma_{RM_d}^2 \lambda^4$, $\Omega_h = 2\sigma_{RM_h}^2 \lambda^4$, $C_d = 2R_d \lambda^2$, $C_h = 2R_h \lambda^2$, $F = \Omega_d \Omega_h + C_d C_h$, $G = \Omega_h C_d - \Omega_d C_h$.

In Eqs. (4.3) and (4.4), the per-layer total synchrotron emission I_i, the total Faraday depth R_i, the dispersion of the intrinsic *RM* within the volume of the telescope beam σ_{RM_i}, along with the wavelength-independent depolarizing terms W_i are respectively given as

$$\begin{aligned}
I_i &= \varepsilon_i \, L_i, \\
R_i &= 0.81 \, n_{ei} \, \overline{B}_{\|i} \, L_i, \\
\sigma_{RM_i} &= 0.81 \, \langle n_{ei} \rangle \, b_{\|i} \, (L_i \, d_i)^{1/2}, \qquad (4.5) \\
W_i &= \left\{ \frac{\left[\left(\overline{B}_x^2 - \overline{B}_y^2 + \sigma_x^2 - \sigma_y^2 \right)^2 + 4 \overline{B}_x^2 \overline{B}_y^2 \right]^{1/2}}{\overline{B_\perp^2}} \right\}_i, \qquad (4.6)
\end{aligned}$$

where ε_i is the synchrotron emissivity, $b_{\|i}$ is the turbulent field parallel to the line of sight, I_i is the synchrotron intensity, L_i is the path length (pc), along with $\overline{B}_\perp^2 = \overline{B}_x^2 + \overline{B}_y^2$ and $\overline{B_\perp^2} = \overline{B}_\perp^2 + \sigma_x^2 + \sigma_y^2$. The form of W_i in Eq. (4.6) implicitly assumes that emissivity scales with $\varepsilon \propto B_\perp^2$ corresponding to a synchrotron spectral index of -1. Isotropic expressions for the intrinsic polarization angle and for wavelength-independent depolarization are obtained by setting $\sigma_x = \sigma_y$. The operation $\{F, G\} (a)$ is defined as $\{F, G\} (a) =$

$F\cos(a) - G\sin(a)$. $\Delta\psi_{dh} = \langle\psi_{0d}\rangle - \langle\psi_{0h}\rangle$ is the difference in the projected intrinsic polarization angles of the disk and halo with the respective angles given by (Sokoloff et al. 1998, 1999, and Eq. (3.5) of Chap. 3) as

$$\langle\psi_{0i}\rangle = \tfrac{\pi}{2} - \arctan\left[\cos(l)\tan(\phi)\right] + \tfrac{1}{2}\arctan\left(\frac{2\overline{B}_x\overline{B}_y}{\overline{B}_x^2 - \overline{B}_y^2 + \sigma_x^2 - \sigma_y^2}\right)_i . \tag{4.7}$$

Expectation values denoted by $\langle\ldots\rangle$ arise whenever turbulent magnetic fields are present. Only the last term of Eq. (4.7) remains upon taking the difference.

In our use of Eq. (4.5) to describe both isotropic and anisotropic random fields we implicitly treat σ_{RM} as a global constant, independent of the observer's viewing angle as for a purely isotropic random field. Moreover, the diameter of a turbulent cell d_i in the disk or halo, as it appears in Eq. (4.5), is approximately given by (Fletcher et al. 2011)

$$d_i \simeq \left[\frac{D\,\sigma_{RM,D}}{0.81\,\langle n_{ei}\rangle\, b_{\|i}\,(L_i)^{1/2}}\right]^{2/3}, \tag{4.8}$$

with $\sigma_{RM,D}$ denoting the RM dispersion observed within a telescope beam of a linear diameter $D = 600$ pc. $\sigma_{RM,D}$ has been fixed to the observed value of 15 rad m^{-2} (Fletcher et al. 2011).

4.4 Procedure

We use various magnetic field configurations of isotropic turbulent and/or anisotropic turbulent fields in the disk and halo with the requirement that there be at least a turbulent magnetic field in the disk following Fletcher et al. (2011) observations. We also model wavelength-independent depolarization directly via W_i in Eq. (4.6) instead of approximating it with the value of p at the shortest wavelength. Consequently, these turbulent configurations, given in Table 4.3, span 12 of the 17 model types listed in the upper panel of Table 3.2 of Chap. 3, and are illustrated by Figs. 3.2 and 3.3 for an example bin with a particular choice of magnetic field strengths. These configurations may also be viewed in terms of two distinct groups characterized by the presence or absence of a turbulent magnetic field in the halo.

The isotropic and anisotropic turbulent magnetic field strengths in the disk and halo are each sampled from $[0, 2, 5, 8, 10, 15, 20, 25, 30]\,\mu$G in line with M51 observations of having a $10\,\mu$G isotropic and a $10\,\mu$G anisotropic turbulent field in the disk (Houde et al. 2013). We assume that the total turbulent field strength in the halo is less than or equal to that in the disk. For each of these turbulent magnetic field configurations, we allow the regular magnetic fields in the disk and halo to separately vary in the ranges of $0 - 50\,\mu G$ in steps of $0.1\,\mu G$.

We apply a reduced chi-square statistic to discern a best-fit magnetic field configuration for each of the four radial rings, independently, at the three observing wavelengths

Table 4.3: Model settings for a two- or three-layer system based on regular and turbulent magnetic field configurations in the disk and halo.

	Disk			Halo		
	Reg.	Iso.	Aniso.	Reg.	Iso.	Aniso.
DIH	✓	✓		✓		
DAH	✓		✓	✓		
DAIH	✓	✓	✓	✓		
DIHI	✓	✓		✓	✓	
DIHA	✓	✓		✓		✓
DAHI	✓		✓	✓	✓	
DAHA	✓		✓	✓		✓
DIHAI	✓	✓		✓	✓	✓
DAHAI	✓		✓	✓	✓	✓
DAIHI	✓	✓	✓	✓	✓	
DAIHA	✓	✓	✓	✓		✓
DAIHAI	✓	✓	✓	✓	✓	✓

Notes: The three column headings below the principle headings of the 'Disk' and 'Halo' denote the regular, isotropic turbulent, and anisotropic turbulent magnetic fields. The rows contain a listing of all model types simulated with the following nomenclature: 'D' and 'H' denote disk and halo magnetic fields, respectively, 'I' and 'A' are the isotropic and anisotropic turbulent magnetic fields.

$\lambda\lambda\lambda$ 3.5, 6.2, 20.5 cm. The reduced chi-square statistic is given by

$$\chi^2_{red} = \frac{\chi^2}{N} = \frac{1}{N} \sum_{bins \in ring} \frac{(p_{obs} - p_{mod})^2}{\sigma^2},$$

where p_{obs} and p_{mod} are the observed and modeled p values given in Eqs. (4.3) and (4.4), σ is the standard deviation of the measured p values per bin in a given ring, and the sum is taken over all bins comprising a given ring. N is the number of degrees of freedom given by (*# observing wavelengths*) $\times$ (*# bins in a ring*) $-$ (*# independent parameters*), with the number of independent parameters being the variable disk and halo regular magnetic field strengths and, hence, always two, for a fixed input of turbulent magnetic fields describing a particular configuration.

For each turbulent magnetic field configuration sampled, the best-fit combination of total disk and halo regular magnetic field strengths corresponding to the lowest χ^2_{red} value are found and a range of χ^2_{red} contours are plotted in order to examine the χ^2_{red} landscape. Repeating this procedure allows for a global minimum χ^2_{red} value to be obtained for each of the rings.

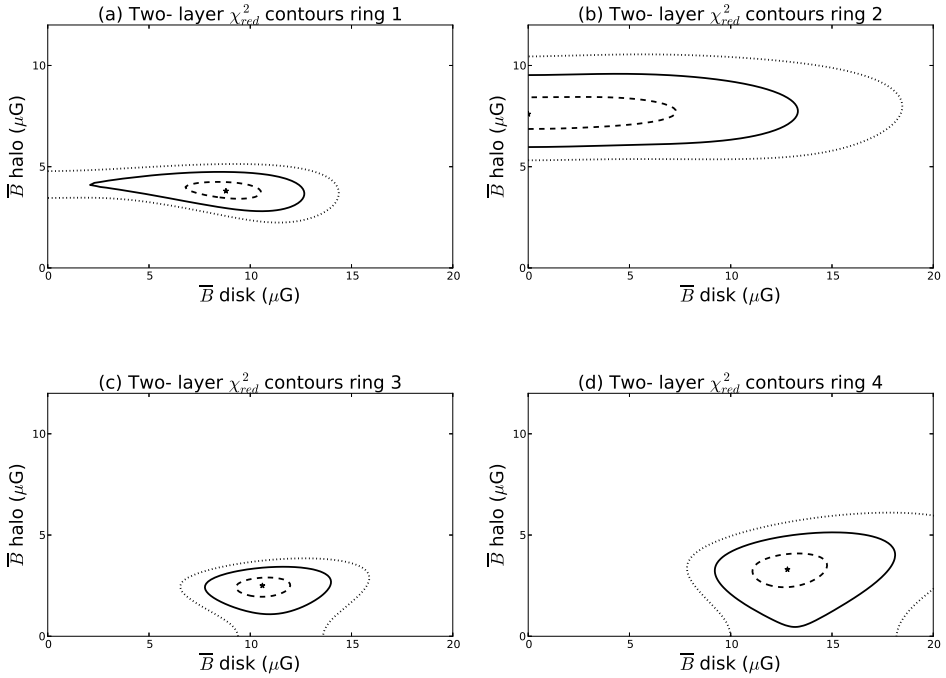

Figure 4.1: (a)-(d) Contours of equal reduced chi-square values for regular magnetic field strengths $\overline{B}$ in disk and halo in a two-layer model for each of the four rings. The best-fit DAIHI model, denoted by ★, is composed of regular, isotropic turbulent and anisotropic turbulent disk and halo magnetic fields with respective minimum reduced chi-square (χ^2_{min}) values and field strengths presented in Table 4.4. The dashed, solid, and dotted contours represent $10, 50,$ and 100 percent increases in the χ^2_{min} value, respectively.

χ^2_{red} values larger than one are accepted in order to establish a trend in turbulent magnetic field configurations and strengths. To test whether the admission of these higher χ^2_{red} values yield regular disk and halo magnetic field configurations that are statistically consistent for each ring, we use a generalization error approach (bootstrap technique) which is independent of the χ^2_{red} statistic. This approach stipulates to approximately retain 70% of the data while discarding around 30% of the data at random, for each independent trial run, and to check the resulting fits again. In this way, the stability of the lowest χ^2_{red} contours for a particular configuration is tested. Following 50 such independent trial runs for each of the global χ^2_{red} minimum found per ring reveals that all such lowest χ^2_{red} contours are *stable* for both a two-layer model and (quasi) stable for a three-layer model.

We examine a smaller subset of the turbulent field configurations for a three-layer model making sure to examine configurations that are both good and poor fits for the corresponding two-layer system.

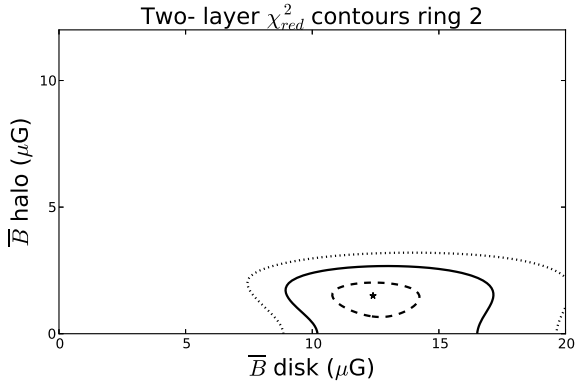

Figure 4.2: Contours of constant $\chi^2_{\rm min}$ for values of regular field in the disk and halo for ring 2 with a deviating value for the isotropic turbulent field corresponding to the alternative best-fit model adopted, see text. Symbols are the same as used in Fig. 4.1.

4.5 Results

4.5.1 Two-layer model

The turbulent magnetic field strengths which correspond to the best-fit two-layer model per ring are presented in Table 4.4 together with the best-fit regular disk and halo field strengths attained from the reduced chi-squared analysis. Errors reported for these respective regular field strengths are based on the solid contour in Fig. 4.1 which represents a 50% increase in the χ^2_{min} value. χ^2_{min} is the minimum χ^2_{red} value corresponding to the best-fit disk and halo magnetic field configuration composed of regular, isotropic turbulent, and anisotropic turbulent magnetic fields.

Figure 4.1 and Table 4.4 clearly indicate that the best-fit magnetic field values in ring 2 deviate from the trend in the other three rings, especially $B_{\rm reg}$ in the disk and $B_{\rm iso}$ in the halo. To test how significant this deviation from the other rings is, we calculated a best-fit model with magnetic field values consistent with the other rings and checked how much the $\chi^2_{\rm red}$ increased. Inserting $B_{\rm iso} = 2$ μG in the halo for ring 2, results in a minimum $\chi^2_{\rm red} = 3.1$ for best-fit regular field values of 12.4 μG and 1.5 μG in the disk and halo, respectively (see Fig. 4.2). Considering the uncertainties in the model, an increase in $\chi^2_{\rm min}$ from 2.4 to 3.1 is not believed to be a significant difference in ring 2. We conclude that these field values are equally plausible and choose to adopt them as the best-fit model, making all magnetic field values in all rings roughly consistent. Fig. 4.3 illustrates these regular and turbulent magnetic field values for the two-layer best-fit models.

Global conclusions to be drawn from these magnetic field values are:

- The total magnetic field strength in the disk is about $B_{tot,disk} \approx 18$ μG, while the total magnetic field strength in the halo is about $B_{tot,halo} \approx 4 - 6$ μG;

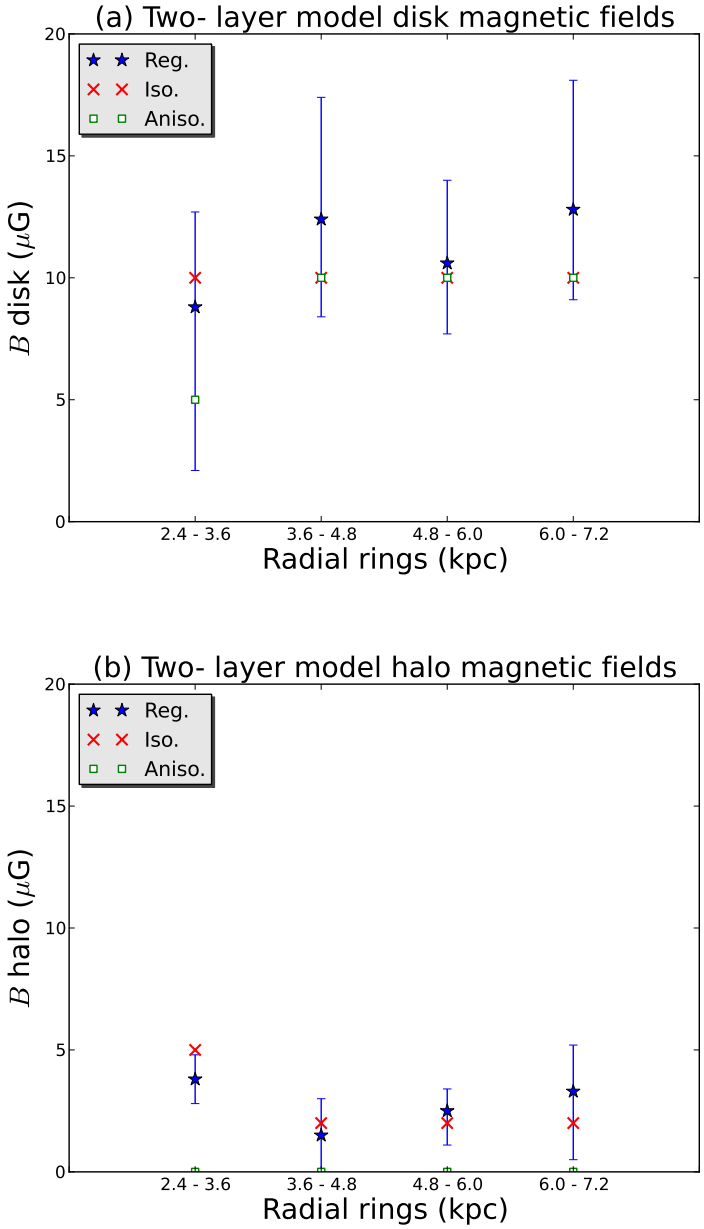

Figure 4.3: Predicted magnetic field strengths (μG) with radial distance (kpc) from M51. The best-fit two-layer model configuration consisting of an isotropic turbulent ('Iso.'), anisotropic turbulent ('Aniso.'), and regular ('Reg.') magnetic field strengths in the disk (a) and halo (b) is shown per ring.

Table 4.4: Two-layer best-fit DAIHI model magnetic field strengths. Values in parenthesis correspond to the alternative best-fit model adopted for ring 2.

	Ring 1	Ring 2	Ring 3	Ring 4
Disk				
Iso.[μG]	10	10	10	10
Aniso.[μG]	5	10	10	10
Reg.[μG]	8.8^{+4}_{-7}	0.0^{+13}_{-0} (12.4^{+5}_{-4})	10.6 ± 3	12.8^{+5}_{-4}
d[pc]	47	40	52	52
Halo				
Iso.[μG]	5	10 (2)	2	2
Aniso.[μG]	0	0	0	0
Reg.[μG]	3.8 ± 1	7.6 ± 2 (1.5 ± 1.5)	2.5 ± 1	3.3^{+2}_{-3}
d[pc]	215	135 (395)	638	638
χ^2_{min}	1.2	2.4 (3.1)	2.1	3.0

- Both regular and turbulent magnetic field strengths in the disk are a few times higher than those in the halo;
- There is a significant anisotropic turbulent field component in the disk, but not in the halo;
- Within the errors, none of the magnetic field strengths shows a clear trend as a function of galactocentric radius. A possible exception here is a slightly stronger (isotropic) random magnetic field strength in the inner halo.

The lower χ^2_{min} value and more sensitive χ^2_{red} range in ring 1 suggest that the regular and turbulent magnetic fields may be best fit in ring 1 of the two-layer model. This may arise from different magnetic field strengths and thermal electron densities between arm and interarm regions. Ring 1 contains mostly spiral arms, while rings 2 - 4 trace both arm and interarm regions which makes a single fit for magnetic field strengths in the entire ring less of a good fit. A π-periodic modulation is apparent in the best-fit polarization profiles of all rings in Fig. 4.4, indicating depolarization caused by the regular, mostly azimuthal, magnetic field component. It can also be clearly seen that smaller errors in the observed p/p_0 decrease the width of the shaded gray corridor in Fig. 4.4.

A model with *only* regular fields does not yield any good fits as expected on physical and observational grounds. A one-layer model is excluded by our modeling as a non-zero regular magnetic field in the halo is predicted by all magnetic field configurations sampled. This is consistent with the expectation of two separate Faraday rotating layers

Table 4.5: Three-layer best-fit DAIHI model magnetic field strengths.

	Ring 1	Ring 2	Ring 3	Ring 4
Disk				
Iso.[μG]	10	10	10	10
Aniso.[μG]	10	10	10	5
Reg.[μG][a]	1.8^{+10}_{-2}	0.0^{+10}_{-0}	2.2^{+17}_{-3}	10.9^{+16}_{-11}
d[pc]	40	40	52	61
Halo				
Iso.[μG]	5	8	10	8
Aniso.[μG]	0	0	0	0
Reg.[μG][a]	3.6 ± 1	5.3^{+2}_{-1}	6.8^{+3}_{-5}	6.8^{+4}_{-7}
d[pc]	215	157	218	253
χ^2_{min}	3.0	3.6	2.1	3.6

Notes: [(a)] A value of $0\,\mu$G is to be used for the lower regular field strength bound when the lower error bound exceeds the actual regular field value.

(Berkhuijsen et al. 1997; Fletcher et al. 2011). We also consider observations of M51 at 610 MHz which show that $p/p_0 < 1\%$ in spiral arms (Farnes et al. 2013). Applying the criterion that $p/p_0 < 1\%$ in the bins that contain the spiral arms in each ring, results in the exclusion of all field configurations which do not have a turbulent magnetic field in the halo. This also automatically rejects a one-layer model.

4.5.2 Three-layer model

For a three-layer model, with identical near and far sides of the halo, the χ^2_{red} landscape consists of an archipelago of minimum χ^2_{red} values as shown in Fig. 4.5. If a minimum χ^2_{red} were to be taken as representative of a global minimum, then, for the purposes of comparison with the two-layer model, we present the best-fit three-layer model results per ring in Table 4.5. The three-layer best-fit models are poorer fits to the polarization observations than the two-layer models owing to the higher χ^2_{min} in the innermost pair of rings and the outermost ring. Both three- and two-layer models favor the absence of an anisotropic turbulent halo field in all rings. Summarizing, the three-layer models result in roughly the same magnetic field values as the two-layer models.

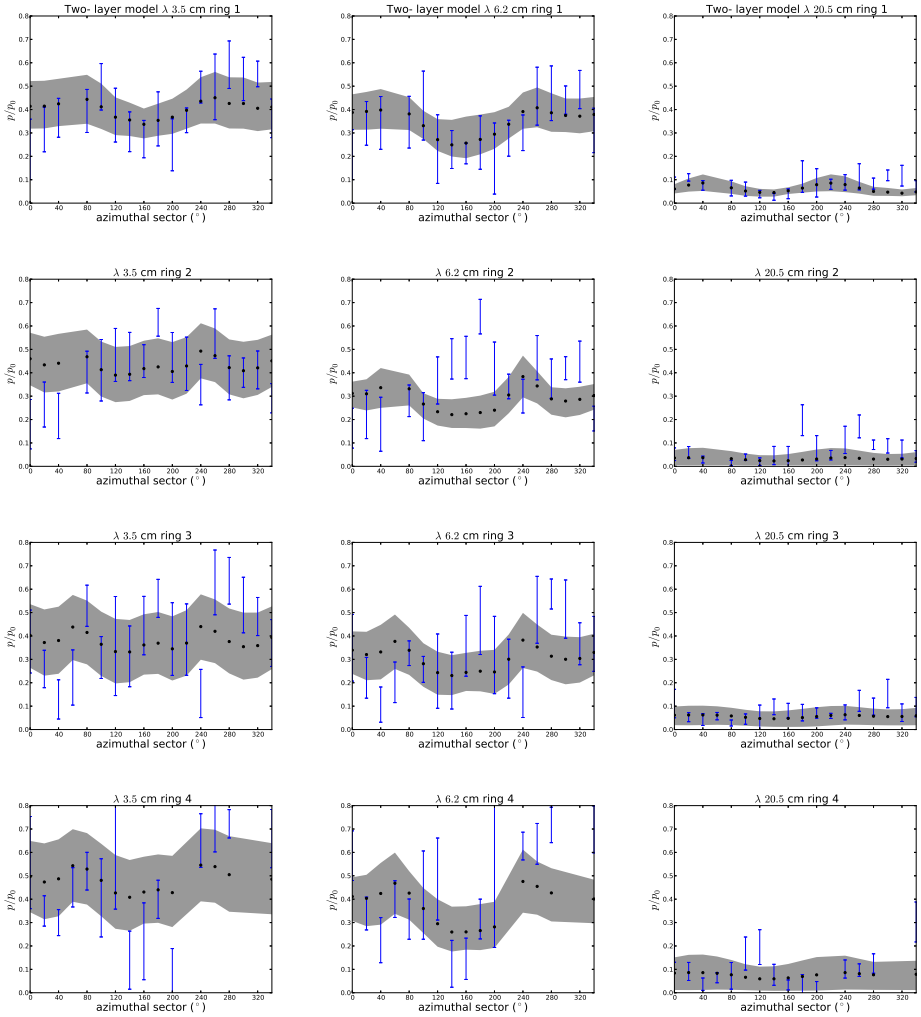

Figure 4.4: Normalized polarization degree p/p_0 as a function of azimuthal angle for observing wavelength of $\lambda\lambda\lambda$ 3.5, 6.2, 20.5 cm for each of the four rings for a two-layer model. Columns provide the polarization profiles per ring at a fixed observing wavelength while rows provide polarization profiles at all three observing wavelengths at a fixed ring. 0° corresponds to the North major axis of M51 with sectors counted counterclockwise. The solid black points correspond to the predicted polarization value, at each azimuth, from the best-fit magnetic field strengths. The shaded gray region corresponds to the range of polarization values predicted by all regular disk and halo magnetic field configurations encompassed by the solid, $1.5 * \chi^2_{min}$ contour in Fig. 4.1 for rings 1,3,4 and in Fig. 4.2 for ring 2. The turbulent magnetic fields are the same as described in Table 4.4. The following sectors have been discarded as they are outliers (see text): sector at 60° for the inner two rings, and sectors at 220°, 300°, and 320° in the outermost ring.

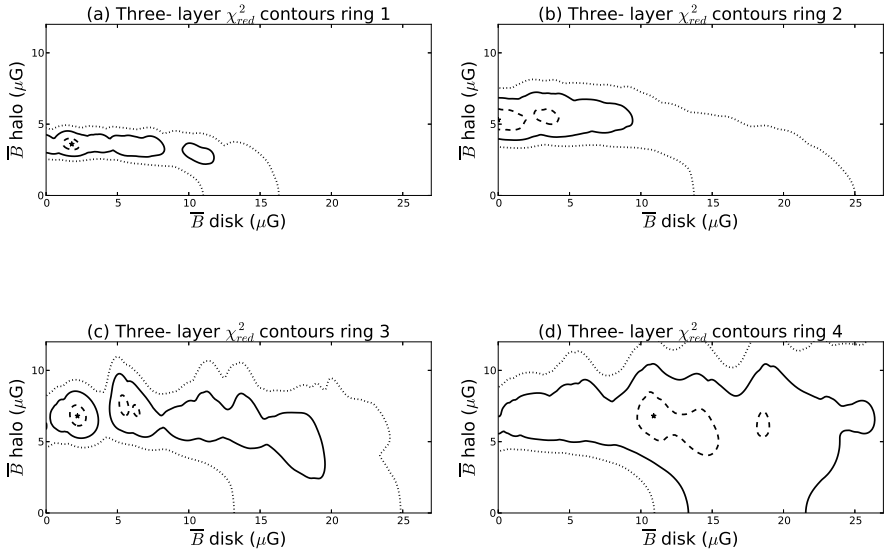

Figure 4.5: (a)-(d) Same as in Fig. 4.1 but now for a three-layer DAIHI model.

4.5.3 Robustness of results

The stability of the lowest χ^2_{red} contours for the two-layer models and the (quasi) stability of such contours for the three-layer models, following the bootstrap technique discussed in Section 4.4, gives confidence as to the robustness of the results. In addition, the elongated shape of the $\chi^2_{\rm red}$ contours in both these figures indicates that the halo is more sensitive to variation in its regular field value and is therefore a stronger depolarizing region than the disk. The models also yield χ^2_{red} contours for the innermost and outermost pair of rings which are morphologically similar among themselves. Morphological similarity between the rings constituting each pair may be expected based on the physical parameters of thermal electron density and path length being equal for each pair as listed in Table 4.2.

An area of very strong polarized intensity observed at $\lambda\lambda\, 3.5, 6.2$ cm in Fletcher et al. (2011, Fig. 2) coincides with the ring 1 sectors at 300° and 320° and plausibly accounts for the underestimated p values at those locations at all observing wavelengths. Moreover, the ring 1 and ring 2 bins at 60° along with the ring 4 bin at 320° are outliers as a result of an area of sparse data in the same maps and are consequently discarded. The results shown in Tables 4.4, 4.5 are obtained from the outlier free data.

Using the innermost ring which traces the data the closest, our models allow considerable variation in the turbulent magnetic field values in the disk, while magnetic field values in the halo are tightly constrained. In particular, replacing the best-fit ring 1 configuration in Table 4.4 with isotropic and anisotropic turbulent disk fields of 20 μG each,

while retaining the 5 μG isotropic turbulent halo field, results in less than a 20% increase in $\chi^2_{\rm min}$ whereas only changing the isotropic turbulent halo field to 10 μG, while keeping the isotropic and anisotropic turbulent disk fields at 10 μG and 5 μG, respectively, results in more than a 25% increase in $\chi^2_{\rm min}$. Correspondingly, total turbulent field values of up to 30 μG are allowed in the disk. However, Houde et al. (2013) report an observed value of the total turbulent disk field of 15 μG in M51, so that any models with a total turbulent field greater than 15 μG are excluded observationally. Finally, the *regular* disk and halo field strengths vary only slightly for all allowed values of turbulent disk and halo fields, indicating that they are robust for all rings.

4.6 Discussion

The picture that emerges is the following: in the disk, magnetic field strengths are $B_{\rm reg} \approx 10$ μG and $B_{\rm turb} \approx 11 - 14$ μG, where $B_{\rm turb}$ includes both the isotropic and anisotropic random components. In the halo, $B_{\rm reg} \approx 3$ μG and $B_{\rm turb}$ is about equal to $B_{\rm reg}$ and consists only of an isotropic component; there is no anisotropic random field in the halo. If anisotropy in magnetic field fluctuations is caused mostly by the strong density waves in M51 and shearing flow, the anisotropy would indeed mostly or exclusively occur in the disk. The regular and total magnetic field strengths in the disk are in agreement with equipartition values of $B_{\rm reg} \approx 8 - 13$ μG and $B_{\rm tot} \approx 15 - 25$ μG as calculated by Fletcher et al. (2011).

In the halo, maximum cell sizes of the turbulence appear to increase towards the outer part of the galaxy (for a two-layer model), whereas the turbulent cell sizes in the disk are approximately equal. The smaller the turbulent field strength, the larger the turbulent cell size for the representative *RM* dispersion as given by Eq. (4.8). If the turbulent cell size in the halo were equal for the inner and outer parts of the galaxy, the *RM* dispersion would decrease towards the outer part of the galaxy, for the values of turbulent magnetic field resulting from the model, which is not observed. However, the cell size in the halo is uncertain since Eq. (4.8) is only valid for $d \ll D$ and $d \ll L$, which might not be the case in the halo.

The field strengths we find are broadly consistent with earlier studies. Berkhuijsen et al. (1997) discussed the magnetic fields in M51 in terms of separate disk and halo for the first time. They found a slightly lower regular magnetic field in the disk $B_{reg,disk} \approx 7$ μG, constant across the disk. Their (assumed isotropic) turbulent field strength is comparable to our results; they show that for even larger galactocentric radii out to 15 kpc, this turbulent magnetic field is expected to decrease to ~ 9 μG. Fletcher et al. (2011) finds regular magnetic field strengths in both the disk and halo between roughly $1 - 4$ μG with a slight increasing trend in disk regular field strength with radius. They ascribed these anomalously low values to ignoring anisotropic random fields in the equipartition estimate for the regular field strength. There is still an anomaly in the estimated regular field strengths though since the polarization angle and *RM* give $1 - 4$ μG while depolarization and equipartition both give 10 μG field strengths. Possible explanations include ignoring the (unknown) filling factor of the thermal electrons in the *RM* based estimate, correla-

tions in the line-of-sight distributions of $B_{\parallel}$ and n_e, and equipartition not holding.

The resulting magnetic field strengths in the two-layer models and the three-layer models are in agreement. In fact, if the best-fit turbulent magnetic field configurations for all rings for the two-layer model were to be used for a three-layer model, then the resulting best-fit regular disk and halo fields would still be described by the three-layer model within the stated error. This implies that all of the signal is depolarized from the far side of the halo, at all wavelengths. Our models therefore confirm the conclusions from Horellou et al. (1992) and Berkhuijsen et al. (1997) based on Faraday rotation and polarization angle measurements. Analyzing polarization data of 21 nearby galaxies from the WSRT SINGS survey (Heald et al. 2009), Braun et al. (2010) concluded from RM Synthesis that M51 shows polarized intensity at Faraday depths $\phi \approx +13$ rad m^{-2}, coming from a region of emissivity located just above the midplane. They also measured Faraday depth components of about -180 and 200 rad m^{-2}, interpreted as emission from the far side of the mid-plane, which is highly Faraday rotated because of its propagation through the midplane. The positive and negative Faraday depth components roughly coincide to the hemispheres of the disk where the an azimuthal magnetic field would point towards or away from the observer. The high Faraday depth components are consistent with our model, assuming the path length and electron density as in Table 4.2 and $B_{\parallel} = 10\sin(l)\,\mu$G. The turbulent cell sizes found for the disk agree with the values in (Fletcher et al. 2011; Houde et al. 2013) and the turbulent cell sizes in the halo are characteristic of the typical cell size expected for spiral galaxies of between 100 − 1000 pc (Sokoloff et al. 1998).

The expected total magnetic field strength may also be estimated from the interdependence of the magnetic field strength, gas density, and star formation rate (SFR) as suggested by the far-infrared - radio correlation (Niklas & Beck 1997). Schleicher & Beck (2013) demonstrated that the observed relation between star formation rate and magnetic field strength arises as a result of turbulent magnetic field amplification by turbulent dynamo action, with turbulence driven by supernova (SN) explosions. The expression they derived, applied at a redshift $z = 0$, is given by

$$B_{\rm tot} \sim \sqrt{f_{\rm sat} 8\pi}\,\rho_0^{1/6}\,(f_{\rm mas}\,\epsilon\,E_{\rm SN})^{1/3}\,\Sigma_{\rm SFR}^{1/3}, \tag{4.9}$$

where $\rho_0 \sim 10^{-24}\,{\rm g\,cm^{-3}}$ is the typical ISM density, $\Sigma_{\rm SFR} \sim 0.1\,M_\odot\,{\rm kpc^{-2}\,yr^{-1}}$ is a reference SFR per unit area, $f_{\rm sat} \sim 5\%$ is the expected saturation level for supersonic turbulence or fraction of the turbulent energy averaged over timescales of ~ 100 Myr, $f_{\rm mas} \sim (8\%/M_\odot)$ is the mass fraction of stars yielding core-collapse SNs, $\epsilon \sim 5\%$ is the fraction of SN energy converted to turbulence, and $E_{\rm SN} \sim 10^{51}$ erg is the typical energy released by an SN. The $B_{\rm tot} \propto \Sigma_{\rm SFR}^{1/3}$ scaling of Schleicher & Beck (2013) is comparable with the observed relation between equipartition magnetic field strength and star formation rate for spiral galaxies by Niklas & Beck (1997). We take $\Sigma_{\rm SFR} = 0.012\,M_\odot\,{\rm kpc^{-2}\,yr^{-1}}$ for M51, adopted from Table 3 of Tabatabaei et al. (2013), which gives a total magnetic field strength $B_{\rm tot} \sim 10\,\mu$G via Eq. (4.9), as an order of magnitude estimate. Considering the roughness of the estimates of the parameter values in Eq. (4.9), $B_{\rm tot} \sim 10\,\mu$G in the disk is consistent with our results.

4.7 Conclusion

We have shown that it is possible to use our analytical depolarization models with radio polarimetric observations, consisting of only three observing wavelengths at $\lambda\lambda\lambda$ 3.5, 6.2, 20.5 cm, assisted by the criterion found from the 610 MHz M51 data by Farnes et al. (2013), to constrain both regular and turbulent magnetic field strengths in M51. By numerically simulating differential Faraday rotation (DFR) and internal Faraday dispersion (IFD) as the main wavelength-dependent depolarization mechanisms along with the contribution of isotropic and anisotropic turbulent magnetic fields to wavelength-independent depolarization, we have arrived at estimates for both regular and turbulent magnetic field strengths in the disk and halo consistent with literature, as shown in Table 4.4.

This agreement with earlier studies gives confidence that these models are realistic. However, our model is more sophisticated than earlier work since it directly simulates the wavelength-dependent depolarizing mechanisms of DFR and IFD thanks to the presence of both regular and random magnetic fields. Previous models (Berkhuijsen et al. 1997; Fletcher et al. 2011) did not include synchrotron emission from the halo, relied primarily on rotation measure (*RM*) measurements, and did not model the actual contribution of isotropic and anisotropic turbulent magnetic fields to wavelength-independent depolarization.

We find that anisotropic turbulent magnetic field strengths in the disk of M51 are comparable to isotropic turbulent field and regular field strengths of $\sim 10\ \mu$G. However, no anisotropic turbulent field is detected in the halo, where the isotropic field is $\sim 2\ \mu$G, comparable to the regular field strength in the halo.

Comparison of disk-halo models including and excluding a (depolarizing) halo at the far side shows that the far side halo is mostly depolarized at our radio wavelengths, making a two-layer model of disk and near side halo a good approximation.

These models show that even with observational data at only three wavelengths, useful results on magnetic field strengths and configurations can be obtained. Current observational capabilities of broadband radio polarimetry would allow the data to be constrained to a greater extent. This would make it possible not only to better determine whether a two-layer or three-layer modeling approach is best suited for describing the data but also to have tighter estimates for the regular and (isotropic and anisotropic) turbulent field strengths in the disk and halo.

Recent studies by Tabatabaei et al. (2013) and Heesen et al. (2014) have observationally revealed local correlations between the mean and turbulent magnetic field components with the star formation rate with a theoretical motivation for such scenarios recently provided by Schleicher & Beck (2013). Future investigations, in conjunction with tests of models for magnetic field amplification by dynamo action, would, therefore, focus on the dynamical physical quantities that give rise to the field structure found in this work. Valuable for this purpose would be spectroscopic data from Hα and far-infrared to probe the star formation rate, H I and H_2 for estimating gas density, and HI line emission for determination of rotational and turbulent velocity.

Acknowledgements

CS and MH acknowledge the support of research program 639.042.915, which is partly financed by the Netherlands Organization for Scientific Research (NWO). CS is grateful for the additional financial support by the *Leids Kerkhoven-Bosscha Fonds, LKBF* work visit subsidies. AF and AS thank the Leverhulme trust for financial support under grant RPG-097. The simulations were performed on the Coma Cluster at Radboud University, Nijmegen, The Netherlands. We thank the anonymous referee for the valuable suggestion to connect this work with the broader dynamical picture in galaxies and for suggestions for future research.

Bibliography

Beck, R. 2004, Ap&SS, 289, 293
Beck, R. 2007, A&A, 470, 539
Beck, R. 2009, Astrophys. Space Sci. Trans., 5, 43
Berkhuijsen, E. M., Horellou, C., Krause, M., et al. 1997, A&A, 318, 700
Braun, R., Heald, G., & Beck, R. 2010, A&A, 514, A42
Farnes, J. S., Green, D. A., & Kantharia, N. G. 2013, ArXiv e-prints
Ferrière, K. M. 2001, Reviews of Modern Physics, 73, 1031
Fletcher, A., Beck, R., Shukurov, A., Berkhuijsen, E. M., & Horellou, C. 2011, MNRAS, 412, 2396
Heald, G., Braun, R., & Edmonds, R. 2009, A&A, 503, 409
Heesen, V., Brinks, E., Leroy, A. K., et al. 2014, AJ, 147, 103
Heiles, C. & Haverkorn, M. 2012, Space Sci. Rev., 166, 293
Horellou, C., Beck, R., Berkhuijsen, E. M., Krause, M., & Klein, U. 1992, A&A, 265, 417
Houde, M., Fletcher, A., Beck, R., et al. 2013, ApJ, 766, 49
Mao, S. A., McClure-Griffiths, N. M., Gaensler, B. M., et al. 2012, ApJ, 755, 21
Niklas, S. & Beck, R. 1997, A&A, 320, 54
Pavel, M. D. & Clemens, D. P. 2012, ApJ, 761, L28
Schleicher, D. R. G. & Beck, R. 2013, A&A, 556, A142
Shneider, C., Haverkorn, M., Fletcher, A., & Shukurov, A. 2014, A&A, 567, A82
Sokoloff, D. D., Bykov, A. A., Shukurov, A., et al. 1998, MNRAS, 299, 189
Sokoloff, D. D., Bykov, A. A., Shukurov, A., et al. 1999, MNRAS, 303, 207
Tabatabaei, F. S., Berkhuijsen, E. M., Frick, P., Beck, R., & Schinnerer, E. 2013, A&A, 557, A129
Tabatabaei, F. S., Krause, M., Fletcher, A., & Beck, R. 2008, A&A, 490, 1005

5

A 3D magnetic field model for NGC 6946

C. Shneider, M. Haverkorn, A. Williams, G. Heald

Astronomy & Astrophysics, 2015
To be submitted

Abstract

Context. Spiral galaxies generally host regular, large-scale magnetic fields in their disks, following spiral arms. For highly inclined galaxies, large-scale vertical magnetic field components are also usually observed above and below the disk, in the gaseous halo. These magnetic field lines in halos are generally observed to have an X-shape. This could indicate a helical magnetic field structure, naturally produced by a combination of poloidal and toroidal magnetic fields.
Aims. We would like to determine whether an X-shape magnetic field structure in the almost face-on galaxy NGC 6946 can explain observations of the degree of linear polarization (p) in this galaxy, at various wavelengths.
Methods. We construct a 3D divergence-free magnetic field model. The model contains axisymmetric spiral magnetic fields in the galaxy disk, and helical fields in the halo, which are symmetric about the mid-plane. Using suitable thermal electron and cosmic ray electron distributions, we simulate synchrotron emission from this galaxy. We use p as a diagnostic, and compare our findings to polarimetric observations at wavelengths from five radio

bands between 3.5 cm and 23 cm. We assume that wavelength-dependent depolarization is negligible at our shortest wavelength, and use the observations at this wavelength to determine the amount of wavelength-independent depolarization. The other wavelengths are then scaled by this amount. We simulate p maps for varying regular magnetic field strengths and use the reduced chi-square statistic to determine the best-fit regular field strength for the whole galaxy.
Results. An X-shape field is a feasible model for the 3D regular magnetic field configuration of NGC 6946. Our best-fit field model yields a $\sim 10\,\mu$G field strength in good agreement with earlier estimates that used radio synchrotron observations and equipartition arguments. The model approximately reproduces the azimuthal variation in polarized intensity in the inner galaxy, but still overproduces polarization at certain azimuths, possibly due to lack of turbulent fields in the models.

5.1 Introduction

Magnetic fields are important dynamical constituents of galaxies. They thread the interstellar medium (ISM) and influence virtually all interstellar matter, except for the densest interiors of molecular clouds, via the Lorentz force. Ion-neutral collisions ensure that even cold atomic clouds, with an ionization degree of $10^{-4} - 10^{-3}$, remain tightly coupled to charged particles and, consequently, to the magnetic field (Ferrière 2001). Moreover, magnetic fields affect the thermal conductivity of the ISM (Orlando et al. 2008), the propagation of cosmic rays (Strong et al. 2007; Yan 2015), and the dynamics of molecular clouds and star formation (Hennebelle & Falgarone 2012). Essentially, the magnetic field lines are mostly 'frozen-in' into the interstellar gas. As a consequence, their field geometry is subject to distortion by plasma flows such as from supernova remnants, H II regions, jets, and stars. Additionally, their field strength is varied - amplified, for example, by the combination of large-scale differential rotation and small-scale turbulent motions in galactic disks, as in the Milky Way (Steenbeck & Krause 1966; Parker 1971; Vainshtein & Ruzmaikin 1971), and locally diminished by magnetic reconnection. Turbulent motions are also responsible for the dramatic decrease in the (large-scale) magnetic field diffusion time (Parker 1979). Besides being present in the disks of galaxies, significant magnetic fields are also present in (gaseous) galactic halos where they provide pressure support against the gravity of the halo gas and, thereby, contribute to the hydrostatic balance of the ISM (Boulares & Cox 1990). They also play a role in the disk-halo interaction by transporting magnetic flux from the disk to the halo (Hanasz et al. 2009b), influencing superbubble break-out (Ferrière 2001; Heesen et al. 2009), and transferring charged particles from the galaxy into the intergalactic medium.

Diffuse synchrotron emission traces magnetic fields in galaxies yielding information on the integrated magnetic component perpendicular to the line-of-sight. Traditionally, galactic magnetic fields are divided into small-scale and large-scale fields (see for example Haverkorn (2014)). The term 'large-scale' fields (also called mean, average, global,

regular, uniform or coherent) indicates the component of the magnetic field that is coherent on length scales of the order of a galaxy. 'Small-scale' fields (also called random, tangled, or turbulent) describe the magnetic field component at the scale of ISM turbulence. A large-scale spiral field structure along the disk plane that is aligned with the optical or gaseous spiral arms is observed in nearby spiral galaxies (Krause 2014). Synchrotron emission from halos is more straightforward to study in edge-on galaxies than in face-on galaxies since emission from the disk and halo is not superimposed. From linear polarization studies of edge-on galaxies (e.g., Dahlem et al. (1997); Tüllmann et al. (2000); Krause (2009); Hanasz et al. (2009b); Heesen et al. (2009); Soida et al. (2011); Mora & Krause (2013)) we learned that many halos possess vertical magnetic field components, with field orientation fanning out from the center, forming an X-shape. Following the terminology used by other authors (Ferrière & Terral 2014, and refs. therein), we refer to such fields as 'X-shape'. Whether the X-shaped field is observationally attributable to either the regular field or to the anisotropic turbulent field (ordered field with randomly varying direction on small scales) remains open. Based on polarization data from the WSRT-SINGS (Braun et al. 2007) (Westerbork Synthesis Radio Telescope - Spitzer Infrared Nearby Galaxies Survey) (Kennicutt et al. 2003, SINGS) galaxy sample, Braun et al. (2010) modeled quadrupolar fields that can be interpreted as X-shape fields. An X-shape field is thought to be common in galaxies and its inclusion in the magnetic field models of the Milky Way by Jansson & Farrar (2012a,b) improved overall fits to the rotation measure (*RM*) data. Horizontal and vertical components of the regular magnetic field in the disks and halos of spiral galaxies have been included in earlier models (e.g., see Berkhuijsen et al. (1997); Fletcher et al. (2011) for the case of M51).

X-shaped magnetic fields may be caused by various physical processes. When the X-shape arises from a large-scale magnetic field it is most likely due to a galactic wind which transports the disk field into the halo where the galactic wind occurs in conjunction with dynamo action (Brandenburg et al. 1993; Hanasz et al. 2009a,b; Moss et al. 2010; Hanasz et al. 2013; Gressel et al. 2013). Magnetohydrodynamical (MHD) simulations also show that an X-shape field naturally develops from dynamo action (e.g., Kulpa-Dybeł et al. (2011)). However, simulations incorporating all relevant physics such as turbulence, cosmic rays, supernovae, superbubbles, and the multi-phase nature of the ISM are still to be performed (Gressel et al. 2013). As the magnetic field is coupled to the gas, these X-shape fields may be related to the bi-conical gas outflows in hydrodynamical (HD) simulations (e.g., Dalla Vecchia & Schaye (2008, 2012)).

In this chapter, we study a magnetic field with a vertical magnetic field component in a face-on galaxy. We construct a simple magnetic field model that describes the disk and halo fields of a spiral galaxy and compare with radio polarimetric observations. The aim is to test whether the observed synchrotron (de)polarization can be explained by an X-shaped field in the halo. We choose the grand-design, spiral galaxy NGC 6946 for several reasons: its proximity of 5.5 Mpc (Kennicutt et al. 2003) implies access to high-quality observations, it has one of the highest star-formation rates among spiral galaxies (Beck 2007) which may imply high star formation driven outflows that would contribute to an X-shape, a companion galaxy whose interaction could distort the X-shape is absent, and earlier observations by Beck (2007) and Braun et al. (2010) suggest the presence of a

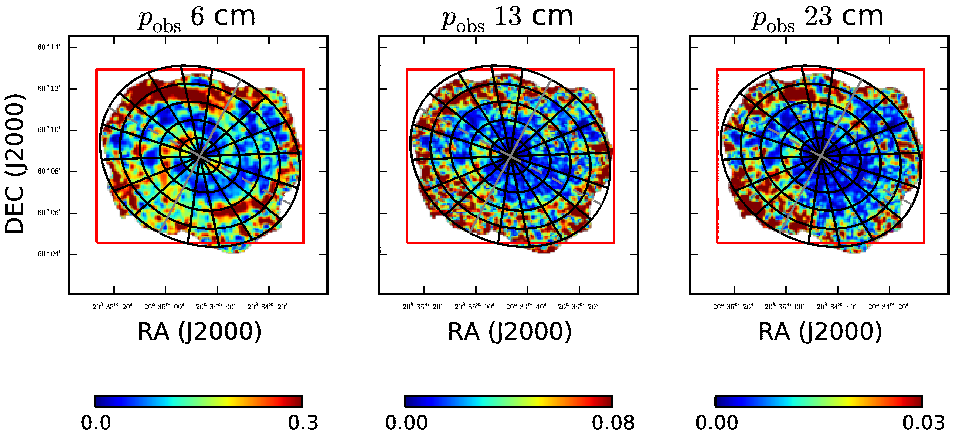

Figure 5.1: The observed degree of polarization $p_{\rm obs}$ maps are shown at 6 cm (left), 13 cm (center), and 23 cm (right). The red rectangle represents the size of the simulation box. The elliptical grid represents the partitioning of the galaxy into bins. The solid and dashed gray lines denote the minor and major axes, respectively, with the kinematically receding side of the galaxy towards the West.

vertical field.

This chapter is organized as follows: In Section 5.2 we present the data. In sections 5.3 and 5.4 we provide a description of the model. Results are presented in section 5.5 and discussed in section 5.6. Finally, we conclude and propose directions for future work in sections 5.7 and 5.8.

5.2 Observational data

We use continuum polarized and total synchrotron intensity observations of NGC 6946 (Williams & Heald 2015). These observations combine data from the Karl G. Jansky Very Large Array (VLA) and Effelsberg 100-m telescope at $\lambda\lambda\,3.5, 6$ cm by Beck (2007), WSRT at $\lambda\,13$ cm by Heald (2014), and the WSRT-SINGS survey at $\lambda\,23$ cm by Braun et al. (2010). The $\lambda\lambda\lambda\,13, 18$ and 23 cm data each have a $\sim$ 10 MHz bandwidth, consisting of 14, 11, and 15 channels, respectively, while the $\lambda\lambda\,3.5, 6$ cm are single channels, for a total of 42 maps. The WSRT data miss short spacing information. The largest detectable scales are 12.4′ at 13 cm, and 22′ at 23 cm. At the adopted distance to NGC 6946, the diameter of NGC 6946 is about 10′ along the major axis. There is thus no missing large-scale structure at 13, 23 cm since the largest angular scales probed correspond to distances much larger than NGC 6946.

The thermal radio emission at $\lambda\,6$ cm is determined and subtracted using an an H-alpha image by Ferguson et al. (1999) and the method described in Heesen et al. (2014, Section 3.2). This final total intensity map is then used to generate non-thermal emission maps at all other available frequencies by assuming two separate synchrotron spectral

index values of −0.7 and −1. These values of spectral index are representative of the spiral arms and interarm regions, respectively (Beck 2007; Tabatabaei et al. 2013).

Multichannel Stokes Q and U observations are first smoothed to a common 15″ beam resolution and then combined to arrive at polarized intensity (P) maps. In linear scale, 15″ corresponds to 400 pc. Subsequently, maps of observed degree of polarization ($p_{\rm obs}$) are obtained by taking P/I. A sample of three such maps is shown in Fig. 5.1 at $\lambda\lambda\lambda$ 6, 13 and 23 cm. The color scale is adjusted at each wavelength in Fig. 5.1 to bring out small scale features.

5.3 Model

5.3.1 Magnetic field

We model the magnetic field in NGC 6946 using a large-scale field. This approach is useful to expand the Braun et al. (2010) analysis to a more physically motivated magnetic field model. We would like to explore the effect of large scale field structures on the observables when varying the parameters of a realistic large-scale field configuration. We adopt an X-shape field as defined in model 'Dd' of Ferrière & Terral (2014, see their Fig. 3). This model is selected because it reproduces the observationally recognizable polarized synchrotron radiation pattern observed in the halos of edge-on galaxies. The model is composed of an axisymmetric (ASS) spiral field in the disk and an X-shape field in the halo. Our X-shape regular magnetic field is physical in that it is divergence-free. Also, we choose to avoid a pure dipole and/or quadrupole magnetic field geometry as modeled in Braun et al. (2010) for qualitative comparison of field configurations. Quantitatively, dipole or quadrupole fields are not realistic as there are cross-field electric currents flowing in the interstellar plasma enclosed by the galaxy. In galactocentric cylindrical coordinates (r, ϕ, z) the field is given by

$$\begin{aligned} B_r &= -\frac{1}{3}\,\frac{r_1^3}{r^2\,z}\left[\sqrt{\left(\frac{z_1}{z}\right)} - \frac{z}{z_1}\right] B_z(r_1, z_1), \\ B_\phi &= \cot\left\{p_\infty + (p_0 - p_\infty)\left[1 + \left(\frac{|z|}{H_{\rm p}}\right)^2\right]^{-1}\right\} B_r, \\ B_z &= \frac{r_1^2}{r^2}\, B_z(r_1, z_1), \end{aligned} \tag{5.1}$$

with the reference field

$$B_z(r_1, z_1) = B_1 \,\mathrm{sign}\, z_1 \,\exp\left(-\frac{r_1}{L_{\rm B}}\right), \tag{5.2}$$

and with

$$r_1 = \frac{3}{2}\, r \left[\sqrt{\left(\frac{z_1}{z}\right)} + \frac{1}{2}\,\frac{z}{z_1}\right]^{-1},$$

where, in the above relations, r_1 is the radius of field lines at the reference height $z_1 = |z_1| \operatorname{sign} z$ and where sign z ensures that the model is symmetric since z/z_1 is always positive. Since field lines bend away and do not cross the mid-plane, in order to avoid having a singularity at $r = 0$ while keeping the field divergence-free, two values of z_1 with a positive/negative value for field lines above/below the mid-plane have to be taken. The physical meaning of the various model parameters in Eqs. (5.1) and (5.2) is as follows: p_0 is the pitch angle of the magnetic field line at the mid-plane ($m = 0$ mode), p_∞ is the pitch angle of the magnetic field line at an infinite height above/below the plane, H_p is the height above the disk plane corresponding to the average value of the pitch angle between mid-plane and infinity, B_1 is the peak value of the reference field, and L_B is the exponential scale length of the reference field.

The pitch angle of the counter-clockwise directed 'magnetic spiral arms' has a positive sign and is given by $p_0 = +28^\circ$ which agrees well with the pitch angle of the optical spiral arms (Kennicutt 1981). Qualitatively, it may be expected that field lines become less tightly wound and thus have a larger pitch angle at higher latitudes since galactic differential rotation probably decreases with distance from the mid-plane (Ferrière & Terral 2014). Assuming that the magnetic spirals unwind at large vertical heights, $p_\infty = +90^\circ$.

The overall field morphology is affected by the parameters z_1, H_p and L_B. The parameter z_1 affects the degree to which the ASS disk field is extended by a quadrupolar morphology in the halo. Large values of H_p preserve the initial pitch angle at the mid-plane up to large vertical heights while too small values make the spirals unwind at small distances from the mid-plane. Moreover, the value of L_B regulates the spread of field lines with a value of $1 < L_\mathrm{B} < 5$ kpc keeping the field lines from becoming too congested in the center at low L_B values.

In the frame of the galaxy, but now in Cartesian coordinates, the total field is

$$B_x = B_r \cos(\phi) - B_\phi \sin(\phi), \tag{5.3}$$

$$B_y = B_r \sin(\phi) + B_\phi \cos(\phi), \tag{5.4}$$

$$B_z = B_z. \tag{5.5}$$

The position angle of the major axis is 242° (Boomsma et al. 2008). Choosing the origin of the coordinate system to coincide with the dynamical center of the galaxy, with the x- and y- axes labeling the major and minor axes, respectively, the receding side of the galaxy is then labeled by $\phi = 0^\circ$ and the approaching side by $\phi = 180^\circ$. The observer's frame (sky-plane) components are obtained for the inclination angle, l, of the galaxy from Eqs. (5.3)-(5.5) as (Braun et al. 2010)

$$B_{x'} = B_x, \tag{5.6}$$

$$B_{y'} = B_y \cos(l) - B_z \sin(l), \tag{5.7}$$

$$B_\parallel = B_y \sin(l) + B_z \cos(l), \tag{5.8}$$

where $(x', y', \parallel)$ are the major axis, minor axis, and line of sight, respectively. The inclination angle is taken as $l = 33^\circ$ (Heald et al. 2009).

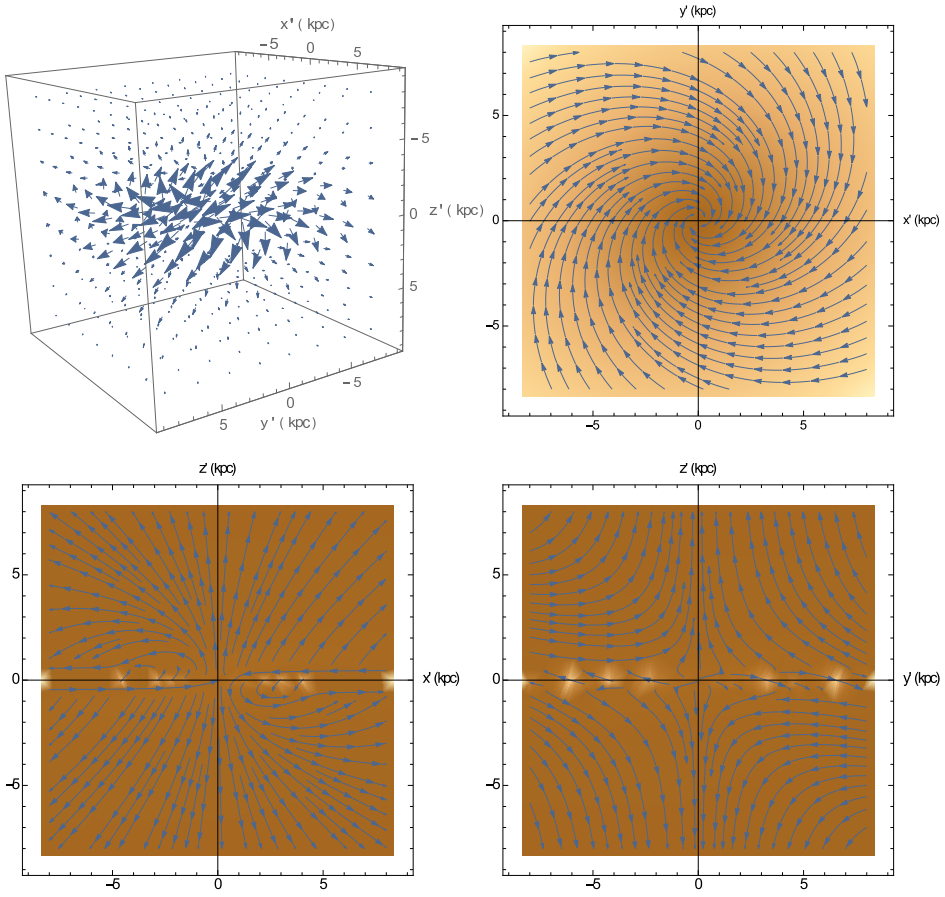

Figure 5.2: The regular magnetic field is shown using standard model parameters (see Section 5.4) viewed almost edge-on from an arbitrary angle. Top left: the 3D regular magnetic field vectors as simulated in a $16 \times 16 \times 16\,\mathrm{kpc}^3$ volume. The other panels show magnetic field components in slices through this cube in orthogonal directions. The direction of the slices are shown in the axes, and the slices are taken close to midway through the cube. The blue lines show the magnetic field direction in the plane of the slice, and the color scale shows the strength of the field component in that slice.

5.3.2 Densities

We focus on the diffuse ionized emission as this is more significant than H II regions for Faraday rotation, owing to its larger filling factor (Beck & Wielebinski 2013). Although both the warm ionized medium (WIM) component and the hot ionized medium (HIM) contribute to the thermal electron density (n_e), the HIM component has a negligible affect on depolarization. This is on account of the HIM being so dilute with $n_\mathrm{e} \sim 10^{-3}$ cm^{-3}

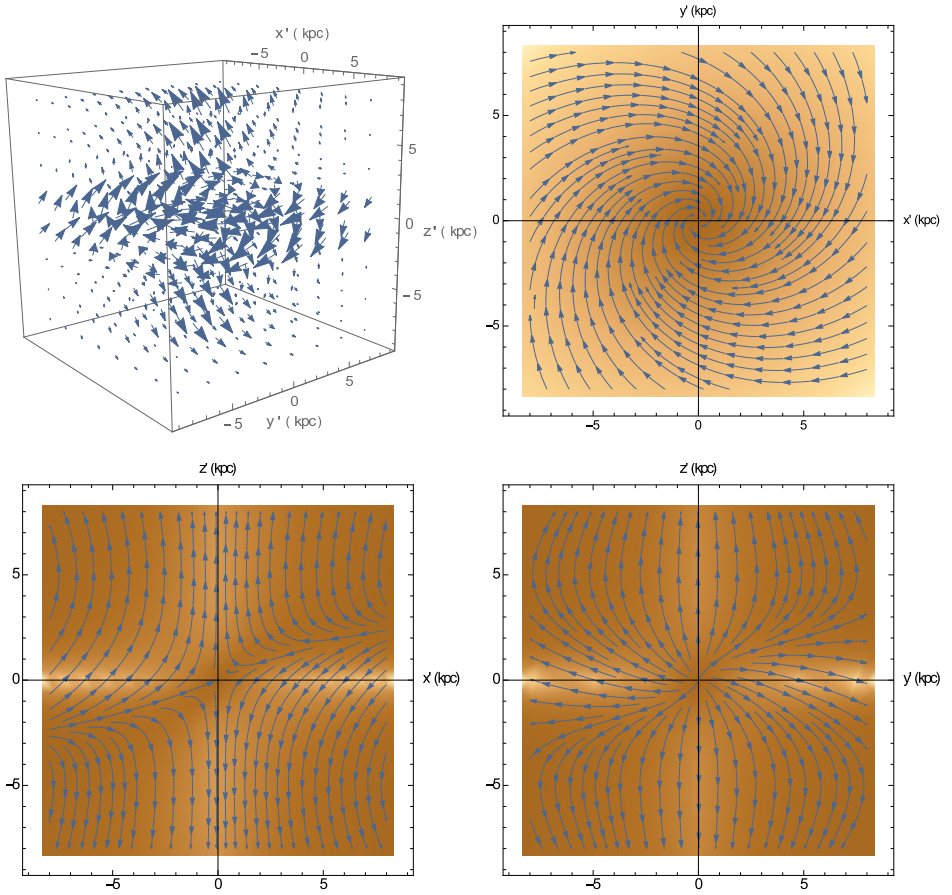

Figure 5.3: As in Fig. 5.2 but using best-fit model parameters (see Section 5.5).

(Haverkorn & Spangler 2013, Table 1).

In our model, cosmic rays are assumed to distribute homogeneously. Consequently, the synchrotron emissivity ε scales with the magnetic field as

$$\varepsilon(\boldsymbol{x}') = c\left(B_{x'}^2 + B_{y'}^2\right)(\boldsymbol{x}'), \tag{5.9}$$

with c a constant proportional to the cosmic ray electron density. This assumed quadratic dependence of emissivity on magnetic field is an observationally consistent scaling for disks and halos of galaxies (Sokoloff et al. 1998, 1999).

5.3.3 Stokes parameters

The degree of polarization p is the ratio of polarized intensity (P) to total intensity (I) and is given by

$$p = \frac{P}{I} \tag{5.10}$$

with $0 \leq p \leq p_0$ where $p_0 = 0.75$ is chosen as the maximum intrinsic degree of polarization. A synchrotron spectral index between -0.5 to -1.1 corresponds to an intrinsic polarization value of $70 - 76\%$. Since we are using -0.7, p_0 should in principle be closer to 70%. However, from the large errors both in the observations in the outermost pair of rings at all frequencies and from all observations at low frequencies, a p_0 of 0.75 is fine.

The Stokes parameters composing the polarized intensity and total intensity in Eq. (5.10) are given by

$$\begin{aligned}
I &= \int_0^{L_{\rm tot}} \varepsilon\,(\boldsymbol{x}')\; dz, \\
Q &= \int_0^{L_{\rm tot}} \varepsilon\,(\boldsymbol{x}') \cos\left[2\left(\psi_0 + 0.81\,\lambda^2 \int_{z'}^{L_{\rm tot}} n_{\rm e}\, B_{\parallel}\,(\boldsymbol{x}')\, dz''\right)\right] dz', \\
U &= \int_0^{L_{\rm tot}} \varepsilon\,(\boldsymbol{x}') \sin\left[2\left(\psi_0 + 0.81\,\lambda^2 \int_{z'}^{L_{\rm tot}} n_{\rm e}\, B_{\parallel}\,(\boldsymbol{x}')\, dz''\right)\right] dz', \\
P &= \sqrt{Q^2 + U^2},
\end{aligned}$$

with magnetic field defined in Eqs. (5.6) - (5.8), the emissivity in Eq. (5.9), and intrinsic polarization angle (Berkhuijsen et al. 1997, and Eq. (3.4) of Chap. 3)

$$\psi_0 = \tfrac{1}{2}\pi - \arctan\left[\cos(l)\tan(\phi)\right] + \arctan\left(B_{y'}/B_{x'}\right).$$

Magnetic field strengths are in μG, λ is the observing wavelength (m), dz'' and dz' are increments along the line of sight with positive direction pointing toward the observer, $L_{\rm tot} = 2\,L_d + 2\,L_h$ is the total path length (pc) with L_d and L_h the assumed scale heights of the thermal disk and thermal halo, respectively, and z' denotes the location of each emitting source along the line of sight with $z' = 0$ marking the location of the farthest source from the observer. In the model described above, the regular magnetic field strength and electron density vary along a line of sight. This causes wavelength-independent depolarization due to varying intrinsic polarization angles along the line of sight, and wavelength-dependent depolarization due to Faraday rotation (differential Faraday rotation). However, because turbulent fields are not modeled, wavelength-dependent depolarization due to internal Faraday dispersion is not described.

5.3.4 Simulated Volume

We simulate a representative galactic volume of $16 \times 16 \times 16\,\mathrm{kpc}^3$ centered on the galaxy. This physical volume is selected to cover the radial extent of the multi-armed spiral pattern of NGC 6946 which is well approximated by an 8 kpc galactocentric radius. The scale

Table 5.1: Model parameters.

	Description	Standard	Best-fit	Sample range
p_0 [°]	pitch angle of field at mid-plane	28*	28	
p_∞ [°]	pitch angle of field at infinity	90	n.a.	
z_1 [kpc]	model reference height	0.5	5	0.5 – 14
H_p [kpc]	reference height for pitch angle	5	∞	$2, 4, 8, 16, \infty$
L_B [kpc]	exp. scale length of ref. field	3	3	0.5 – 5
$n_{\rm e,disk}$ [cm^{-3}]	thermal electron density in disk	0.03*	0.03	0.03, 0.3
$n_{\rm e,halo}$ [cm^{-3}]	thermal electron density in halo	0.003*	0.03	0, 0.003, 0.03, 0.3
L_d [kpc]	scale height of thermal disk	0.5*	0.5	0.5
L_h [kpc]	scale height of thermal halo	5	5	5, 7.5
B_1 [μG]	peak value of the ref. field	0 – 50	37^{+5}_{-6}	0 – 100
$\langle B \rangle$ [μG]	average regular magnetic field		12 ± 2	

Notes: (*) Equal to literature values, see text.

height of the non-thermal emission at λ 20 cm is $\sim$ 4 kpc (Walsh et al. 2002), which is well contained in our model box. As it is the non-thermal emission that we use to fit the models, 8 kpc is a very reasonable vertical extent.

5.4 Method

We partition the $p_{\rm obs}$ maps into four radial rings, centered on NGC 6946's center, with ring boundaries every 1.6 kpc from 1.6−8.0 kpc. The 1.6 kpc incremental distance corresponds to four times the beam size. Every such ring is subdivided into 18 azimuthal sectors, each with an opening angle of 20°, see Fig. 5.1. The number of resolution elements per bin therefore ranges from 7 – 21 elements from the inner ring to the outer ring. This results in a total of 72 bins per map and provides a good sampling of the depolarization features. For each of the bins, the mean of $p_{\rm obs}$ is computed with the standard deviation of $p_{\rm obs}$ taken as the error.

To obtain a model of the degree of polarization ($p_{\rm mod}$), we take an initial 6D parameter space characterized by z_1, $H_{\rm p}$, $L_{\rm B}$, $n_{\rm e}$ in the disk and halo, and B_1. Next, we define a standard model by setting each of these parameters to a physically motivated constant with the exception of B_1 which is the only independent parameter. The standard model parameters are displayed in Table 5.1. The value of z_1 corresponds to the value of L_d, that of $H_{\rm p}$ corresponds to L_h, and the value of $L_{\rm B}$ is selected because it roughly reproduces the observed, approximately constant, profile of magnetic field strength with galactic radius along the disk as shown in Beck (2007, Fig. 5). The thermal electron density and path length through the disk and halo are not known and these values are roughly based on those found for the disk in the models of Ehle & Beck (1993) and Beck (2007) which assumed Milky Way parameters. The thermal electron density in the disk is consistent with

the thermal density of $n_{\mathrm{e,disk}} = 0.05$ cm^{-3} typically assumed for galactic disks (Ferrière 2001).

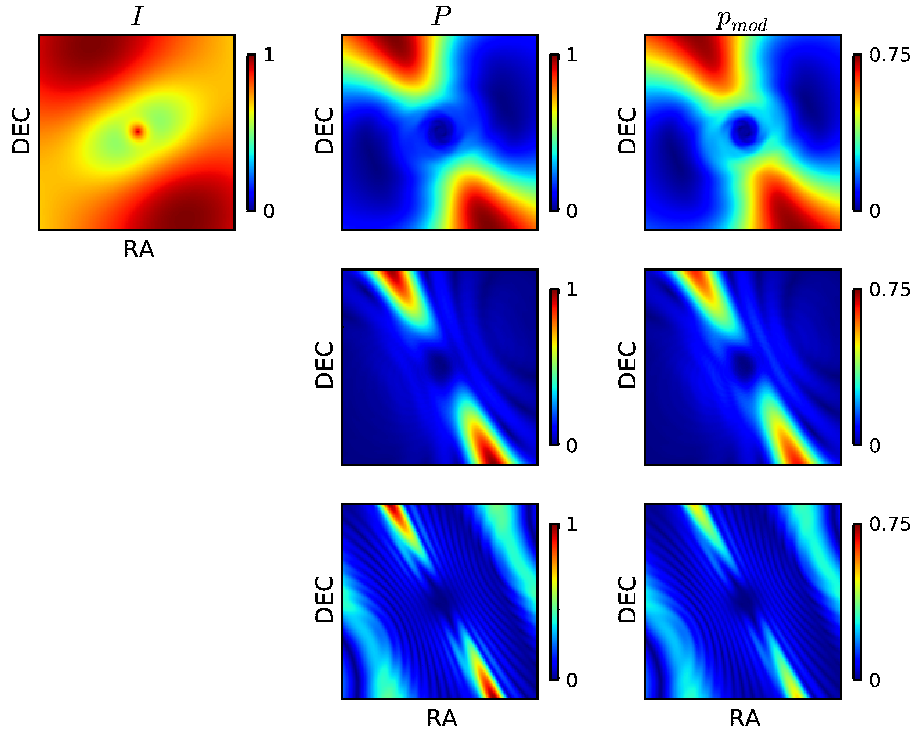

Figure 5.4: Proceeding from the left to right: model outputs of total intensity (I) which has been normalized, polarized intensity (P) which has also been normalized, and degree of polarization (p_{mod}). $I, P,$ and p_{mod} are presented for the best-fit model (see Section 5.5) with P and p_{mod} shown at 6 cm (top), 13 cm (middle), and 23 cm (bottom). The receding side of the galaxy is towards the West.

The standard model is shown in Fig. 5.2 with the full 3D field shown (top left). In the disk, the ASS field is even and points inward (top right), following the direction of the observed optical spiral arms. In the halo, the magnetic field is also even and points outward from the mid-plane, exhibiting a quadrupolar morphology (bottom two panels). These combined ingredients yield p_{mod} via the Stokes parameters which are then compared to p_{obs} to find the best-fit magnetic field strength B_1.

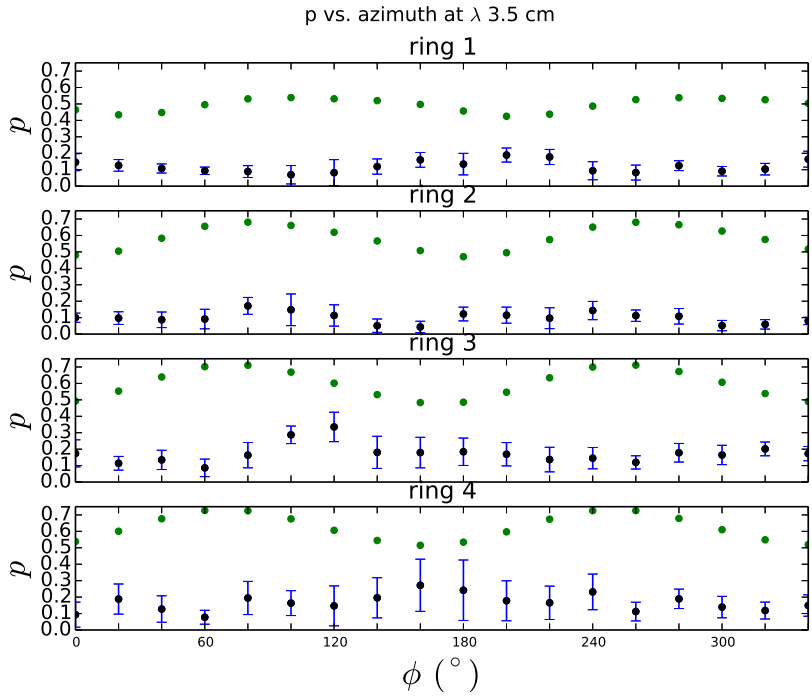

Figure 5.5: The azimuthal variation of the degree of polarization (p) is presented at the lowest observing wavelength of 3 cm in rings 1-4 proceeding from top to bottom. The mean value of the observed p are shown in solid blue points at every azimuthal bin in a ring with associated error bars given by the standard deviation of p in a given bin. The modeled p values without scaling by the factor A (see Section 5.5) are indicated with solid green points. The azimuthal angle (ϕ) is measured counter-clockwise from the receding side of the major axis.

5.4.1 Goodness of fit

A reduced chi-square statistic is computed using all the data bins simultaneously. The reduced chi-square statistic is given by

$$\chi^2_{\rm red} = \frac{1}{N} \sum_{\rm bins} \frac{(p_{\rm obs} - A * p_{\rm mod})^2}{\sigma_p^2}, \tag{5.11}$$

with $A = (p_{{\rm obs},\,\lambda 3.5{\rm cm}} / p_{{\rm mod},\,\lambda 3.5{\rm cm}})$ a parameter estimating the contribution of wavelength-independent depolarization, see Section 5.5. σ_p is the standard deviation of the measured p values per bin, the sum is taken over all bins, and N is the number of degrees of freedom given by (*# observing wavelengths*) $\times$ (*# bins*) $-$ (*# independent parameters*). With the regular field strength as the only independent parameter, the number of degrees of freedom is $N = 2951$.

We test the robustness of our best-fit B_1 value and estimate an uncertainty in this parameter using a bootstrap technique introduced in Chap. 4. Keeping all best-fit model parameters fixed, except for B_1, we again vary B_1 from $0-50\,\mu$G. However, at each value of B_1, we now discard 30% of all azimuthal p bins at random in each ring for all four rings for a fixed observing frequency and compute $\chi^2_{\rm red}$ for 50 independent trial runs. For our large number of degrees of freedom, the chi-square distribution approaches a normal distribution. Subsequently, the mean and standard deviation of $\chi^2_{\rm red}$ corresponding to the best-fit B_1 field strength, over 50 independent trials, is used to establish the range of all other admissible B_1 values and thus the error in the average best-fit regular magnetic field strength. The B_1 values which define the admissible range satisfy the condition that their mean $\chi^2_{\rm red}$ values fall within 1σ of the best-fit $\chi^2_{\rm red}$ mean value.

5.5 Results

The best-fit model has a 3D regular magnetic field configuration, with a reduced chi-square statistic of $\chi^2_{\rm red} = 8.5$, and its parametrization is given in Table 5.1. This model yields a mean regular magnetic field value of $12 \pm 2\,\mu$G in close agreement with estimates given in Beck (2007). This best-fit model was produced assuming a synchrotron spectral index of -0.7, characteristic of the optical spiral arms, which gives better results than the spectral index of -1.0 representative of the interarm regions (Section 5.2). The best-fit magnetic field configuration is shown in Fig. 5.3 and exhibits a pronounced vertical component above and below the central region which is in agreement with magnetic field configurations found in several edge-on spiral galaxies such as NGC 253 in Heesen et al. (2009, Fig. 16) and NGC 5775 in Soida et al. (2011, Fig. 12).

The model outputs of I and P, and p are shown in Fig. 5.4. As expected from the dependence of both I and P on the magnetic field component perpendicular to the line of sight ($B_\perp$), their pairs of maxima and minima occur at the locations of the minor and major axes respectively, though are slightly offset as a result of projection (Braun et al. 2010). However, the modeled Stokes I in Fig. 5.4 shows an increase in intensity in the direction of the minor axis which is not observed (Beck 2007, Fig. 1). We tried an alternative set of models in the range $1 \leq L_B < 3$ kpc with varying values of z_1 which did reproduce the observed radially decreasing intensity. These models, nonetheless, resulted in unbounded values for the regular magnetic field, suggesting that the best-fit magnetic field was higher than the (observationally motivated) field strengths that were probed. As a consequence of the increasing amount of depolarization at longer wavelengths, the value of the $p_{\rm mod}$ maps decrease with increasing wavelength.

Comparing the $p_{\rm mod}$ maps in Fig. 5.4 with the $p_{\rm obs}$ maps in Fig. 5.1 reveals differences in the modeled and observed depolarization patterns. Figure 5.5 shows a comparison between model and observations at $\lambda\,3.5$ cm for all bins. Clearly, the model greatly overestimates the polarization degree. This most likely results from the model not accounting for the turbulent component of the magnetic field, which depolarizes. As a first-order approach to correcting this, we include wavelength-independent depolarization only. We assume that all depolarization is wavelength-independent at $\lambda\,3.5$ cm (i.e. no significant

Faraday rotation at $\lambda\,3.5$ cm) and scale the modeled p at $\lambda\,3.5$ cm to the observed ones. This is done by the factor A in Eq. (5.11).

The best-fit model including wavelength-independent depolarization reproduces the observed azimuthal variation of p in the inner two rings but deviates in the outer two rings as shown in Fig. 5.6 for the innermost and outermost part of the galaxy. As expected on the basis of the above scaling by the factor A, $p_{\rm mod}$ coincides exactly with $p_{\rm obs}$ at the lowest observing wavelength of 3.5 cm in all four figures. In the inner galaxy, $p_{\rm mod}$ generally overestimates $p_{\rm obs}$, while in the outer galaxy, $p_{\rm obs}$ is mostly underestimated. Figure 5.7 shows the wavelength dependence of the depolarization for each bin in the innermost and outermost part of the galaxy. The general decrease with wavelength is reproduced well by the models, although the overestimation of $p_{\rm obs}$ in the inner galaxy is visible in this figure too. Also, the model shows increases of p with increasing wavelength in the outer galaxy for some azimuths, which are not observed. We discuss the discrepancy between observations and model in Section 5.6.

5.5.1 Sensitivity to input parameters

In order to efficiently sample the previously described 6D parameter space, we have made excursions from our standard parameter model, separately for each parameter, while varying B_1 from $0 - 50\,\mu$G. These sample ranges are presented in Table 5.1.

The B_1 value is a robust estimator of the best-fit regular field strength as it does not fluctuate too much when portions of the data are discarded at random (see Section 5.4.1). As Fig. 5.8 shows, the variance decreases for lower chi-square values at larger magnetic field values and the minimum chi-square plateau arising from 50 independent trials lies within the best-fit range determined in Section 5.5.

Our best-fit model is not very sensitive to the exact value of H_p as the sampled range of H_p in Table 5.1 yields similar $\chi^2_{\rm red}$ values of about 9. This trend was taken to indicate that the minimum $\chi^2_{\rm red}$ value would be achieved when the pitch angle would simply be fixed at its mid-plane value everywhere ($H_p = \infty$). This is not an unreasonable choice as p_0 is observed to remain fairly constant with galactic radius of up to 12 kpc in the disk of NGC 6946 (Ehle & Beck 1993). It is clear from the models tested that $n_{\rm e,disk} = 0.03$ cm^{-3} is a good value to use and that the presence of a thermal halo is required with a density equal to that of the disk. This would mean that the thermal electron density in the halo of NGC 6946 is higher than that of the Milky Way, which is estimated as $n_{\rm e} = 0.003$ cm^{-3}. The output values are most dependent on variation in the value of z_1. Figure 5.9 shows the dependence of $\chi^2_{\rm red}$ on the variation in z_1 and B_1. For an initial coarse sampling of B_1 in steps of $4\,\mu$G, Fig. 5.9 shows that $z_1 = 5$ kpc gives the best fit ($\chi^2_{\rm red} = 9.2$) for $B_1 = 36\,\mu$G consistent with the value $B_1 = 37^{+5}_{-6}\,\mu$G found with finer sampling of B_1 for fixed z_1.

5.6 Discussion

Our model explains part of the observations, but also contains features not in agreement with our data or earlier literature. We will discuss both similarities and differences accom-

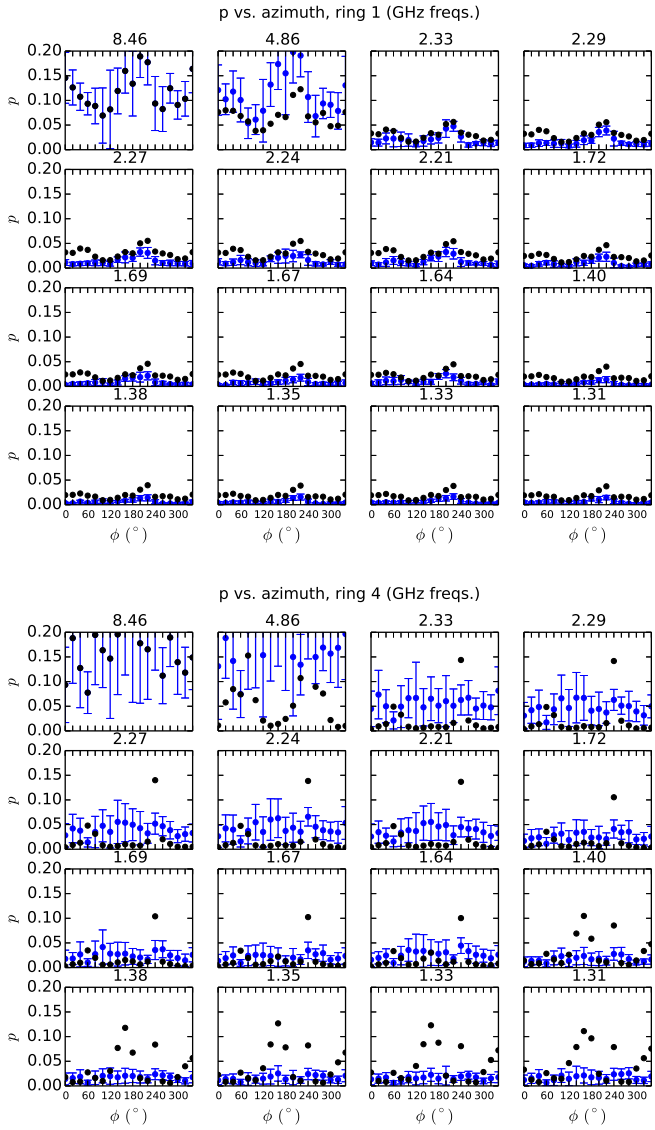

Figure 5.6: The azimuthal variation of the degree of polarization (p) is presented at the two lowest observing wavelengths of 3.5 and 6 cm (first two plots of the top row in both sub-figures) and subsequently at every third wavelength from 13 cm - 23 cm. The mean value of the observed p are shown in solid blue points at every azimuthal bin in ring 1 (innermost ring) in the top sub-figure and in ring 4 (outermost ring) in the bottom sub-figure with associated error bars given by the standard deviation of p in a given bin. The modeled p values are indicated with solid dark points.

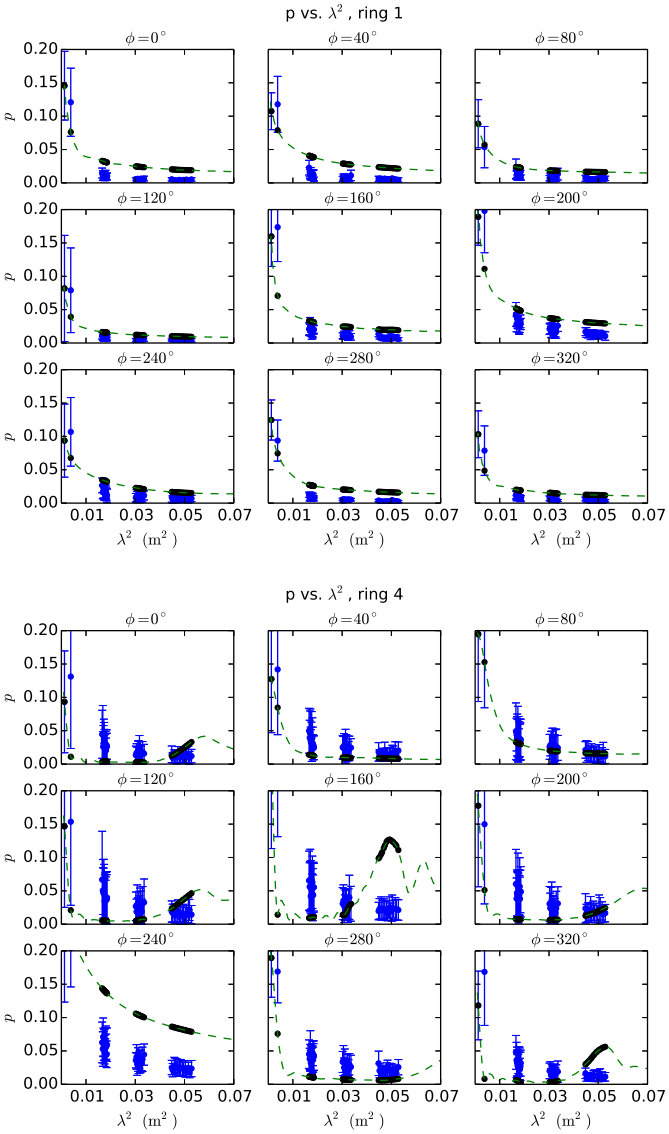

Figure 5.7: The variation of p with the square of the observing wavelength λ^2 (m^2) is presented for the 42 available wavelengths between 3.5 cm to 23 cm at every second of the 18 azimuthal bins ($0^\circ - 320^\circ$ in steps of 40°) comprising ring 1 (innermost ring) in the top sub-figure and ring 4 (outermost ring) in the bottom sub-figure. The mean value of the observed p are shown in solid blue points at every second azimuthal bin in rings 1 and 4 with associated error bars given by the standard deviation of p in a given bin. The modeled p values are indicated with solid dark points. The dashed green line simulates a continuous wavelength coverage spanning 3 cm - 26.5 cm.

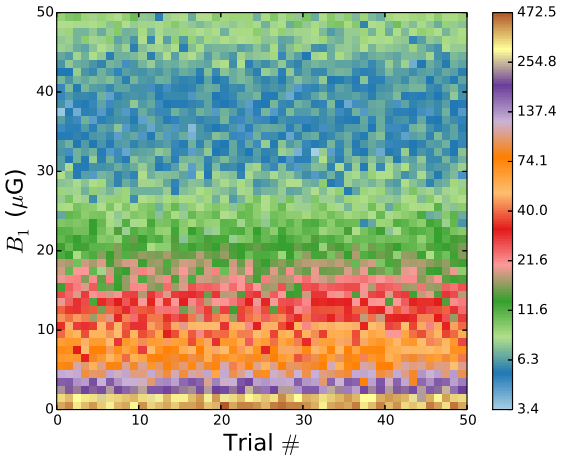

Figure 5.8: Map of reduced chi-square values obtained using the bootstrap technique (see Section 5.4.1) with 50 independent trial runs for each B_1 value.

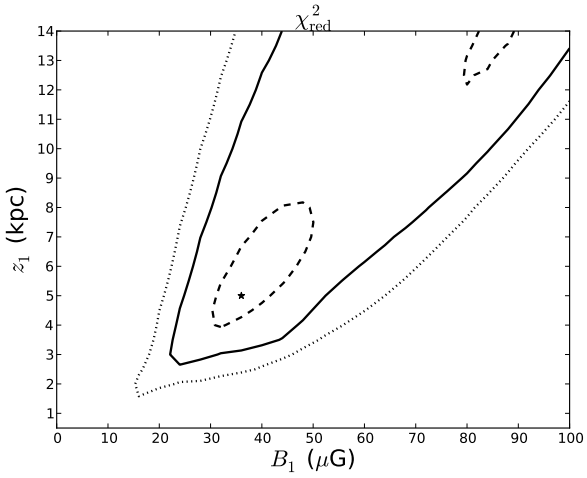

Figure 5.9: Contours of reduced chi-square values for regular magnetic field strength B_1 and height above the mid-plane z_1 for the entire modeled galaxy. The best-fit z_1 and B_1 combination is denoted by ★. The dashed, solid, and dotted contours represent $10, 50,$ and 100 percent increases in the minimum $\chi^2_{\rm red}$ value, respectively.

panied by a possible explanation or way to continue. Our model agrees with a number of galaxy observations (Urbanik et al. 1997; Heesen et al. 2009; Soida et al. 2011; Mora & Krause 2013) and models (Braun et al. 2010). Its features agree with helical magnetic

field models of M 83 and NGC 6946 by Urbanik et al. (1997), who conclude that an extended gaseous and magnetic halo is required, and that the azimuthal field could not be much stronger than the poloidal one. Our best-fit model shows similarities to some of the models described in Braun et al. (2010), in particular the axisymmetric disk field, X-shaped halo fields and a comparable magnetic field scale height.

Our model does not describe wavelength-dependent depolarization due to turbulence. However, no wavelength-dependent discrepancy is seen in $p_{\rm obs}$ in Fig. 5.7 which suggests that this effect can be neglected. The overestimation of $p_{\rm mod}$ in the inner galaxy and underestimation of $p_{\rm mod}$ in the outer galaxy indicates that $p_{\rm mod}$ decreases with radius faster than $p_{\rm obs}$. This could be the result if the magnetic field strength decreases faster as a function of radius in reality than in the model or if there is more turbulence in the inner galaxy than in the outer galaxy which would cause more depolarization in the inner galaxy.

The abrupt rise in $p_{\rm mod}$ at the longest observing wavelengths in the bottom sub-figure of Fig. 5.7 for particular values of the azimuth corresponds to the locations of the two 'secondary maxima' fringe regions (diagonally oriented and parallel to the two expected maxima) at $\lambda\,23$ cm in Fig. 5.4. These fringe regions arise from the interplay between Faraday depth and synchrotron intensity in a multilayer magneto-ionic medium. For the case of a medium consisting of two uniform layers, Chadderton (2011) have shown that complete depolarization will not occur (at any wavelength) if both the following two conditions are satisfied: the layer farthest from the observer must have a much higher Faraday depth than the layer closest to the observer and the layer closest to the observer must constitute some fraction of the total intensity. Although our model does not have a constant magnetic field as in the uniform-layer model, lines of sight that probe the magneto-ionic volume in the outer galaxy may satisfy such conditions at certain azimuths. Since these fringes disappear if the galaxy is taken to be exactly face-on ($l = 0°$), their apparent parallel alignment with the expected two maxima is a result of projection. Alternatively, the absence of these fringe features in $p_{\rm obs}$ may indicate their effective erasure by depolarization from isotropic turbulent magnetic fields or that our X-shape regular magnetic field model requires vertical fields originating at larger radii.

5.7 Summary and conclusions

We constructed a simple analytical model of a 3D regular magnetic field in spiral galaxy NGC 6946. This field model has a vertical field component as observed in a number of edge-on spiral galaxies, and is modeled divergence-free Ferrière & Terral (2014). This magnetic field model, combined with thermal and cosmic ray electron distributions, predicts a degree of polarization at radio wavelengths comparable with multi-frequency radiopolarimetric observations of NGC 6946 Williams & Heald (2015).

The model reproduces the observed azimuthal variation of polarization degree, especially in the inner galaxy. The best-fit average magnetic field strength is $12 \pm 2\,\mu$G, consistent with earlier estimates, and extends out to a vertical height of 5 kpc from the plane. However, the best-fit model shows an unexplained increase in Stokes I away from

the plane, which can only be mitigated with unphysically high magnetic field strengths. Also, at some azimuths, unobserved increases in polarization degree occur in the model. In summary, our magnetic field model including an out-of-plane, X-shaped magnetic field component can reproduce some of the main features of the radiopolarimetric observations, but needs additional complexity to fit the data well.

5.8 Future work

The first priority is finding the reason why the current model does not fit the data well enough. In particular, the model predicts an increase in Stokes I at larger distances from the plane and 'spokes' of high polarization at certain azimuths. Also, modeled RMs are higher than those observed by Beck (2007), which should be improved. Whether our proposed explanation for the absence of these features in the observations is valid and whether a closer agreement with the observations through parameter adaptation may be attained, remains to be demonstrated.

The modeling mechanism itself can be improved in a number of ways. Firstly, the error analysis could be performed in a more rigorous manner by determining the error in B_1 based on small variations in all other model parameters. Second, a more refined approach would be to dispense with rings and sectors altogether and compare model with data in each pixel individually. We could then follow smaller-scale trends in the data better with the model (e.g. distinguishing between spiral arms and interarm regions).

The current model for magnetic field and other galactic components is very simplified. The current magnetic field model could be refined by specifically adding a turbulent component of the field, based on appropriate estimates. Estimates of the total turbulent field such as in Tabatabaei et al. (2013) would be useful in this respect. Also, a low-amplitude quadrisymmetric mode ($m = 2$) to the axisymmetric mode ($m = 0$) in the disk as advocated by Beck et al. (1996); Rohde et al. (1999); Beck (2007) might improve correspondence of the model to the observations. Other possible model refinements would include a variable spectral index (e.g. in spiral arms and interarm regions), based on observational data, and/or a variable cosmic ray electron distribution.

Acknowledgements

CS and MH acknowledge the support of research program 639.042.915, which is partly financed by the Netherlands Organization for Scientific Research (NWO). CS and MH are thankful to Katia Ferrière for enlightening comments on galactic magnetic fields. The simulations were performed on the Coma Cluster at Radboud University, Nijmegen, The Netherlands.

Bibliography

Beck, R. 2007, A&A, 470, 539
Beck, R., Brandenburg, A., Moss, D., Shukurov, A., & Sokoloff, D. 1996, ARA&A, 34, 155
Beck, R. & Wielebinski, R. 2013, Magnetic Fields in Galaxies, ed. T. D. Oswalt & G. Gilmore, 641
Berkhuijsen, E. M., Horellou, C., Krause, M., et al. 1997, A&A, 318, 700
Boomsma, R., Oosterloo, T. A., Fraternali, F., van der Hulst, J. M., & Sancisi, R. 2008, A&A, 490, 555
Boulares, A. & Cox, D. P. 1990, ApJ, 365, 544
Brandenburg, A., Donner, K. J., Moss, D., et al. 1993, A&A, 271, 36
Braun, R., Heald, G., & Beck, R. 2010, A&A, 514, A42
Braun, R., Oosterloo, T. A., Morganti, R., Klein, U., & Beck, R. 2007, A&A, 461, 455
Chadderton, R. 2011, MSc Thesis Newcastle University
Dahlem, M., Petr, M. G., Lehnert, M. D., Heckman, T. M., & Ehle, M. 1997, A&A, 320, 731
Dalla Vecchia, C. & Schaye, J. 2008, MNRAS, 387, 1431
Dalla Vecchia, C. & Schaye, J. 2012, MNRAS, 426, 140
Ehle, M. & Beck, R. 1993, A&A, 273, 45
Ferguson, A., Wyse, R., & Gallagher, J. 1999, in Astronomical Society of the Pacific Conference Series, Vol. 170, The Low Surface Brightness Universe, ed. J. I. Davies, C. Impey, & S. Phillips, 196
Ferrière, K. & Terral, P. 2014, A&A, 561, A100
Ferrière, K. M. 2001, Reviews of Modern Physics, 73, 1031
Fletcher, A., Beck, R., Shukurov, A., Berkhuijsen, E. M., & Horellou, C. 2011, MNRAS, 412, 2396
Gressel, O., Elstner, D., & Ziegler, U. 2013, A&A, 560, A93
Hanasz, M., Otmianowska-Mazur, K., Kowal, G., & Lesch, H. 2009a, A&A, 498, 335
Hanasz, M., Wóltański, D., & Kowalik, K. 2009b, ApJ, 706, L155
Hanasz, M., Woltanski, D., & Kowalik, K. 2013, in IAU Symposium, Vol. 294, IAU Symposium, ed. A. G. Kosovichev, E. de Gouveia Dal Pino, & Y. Yan, 225–236
Haverkorn, M. 2014, ArXiv e-prints

Haverkorn, M. & Spangler, S. R. 2013, Plasma Diagnostics of the Interstellar Medium with Radio Astronomy, ed. A. Balogh, A. Bykov, P. Cargill, R. Dendy, T. Dudok de Wit, & J. Raymond, 407
Heald, G. 2014, in prep
Heald, G., Braun, R., & Edmonds, R. 2009, A&A, 503, 409
Heesen, V., Brinks, E., Leroy, A. K., et al. 2014, AJ, 147, 103
Heesen, V., Krause, M., Beck, R., & Dettmar, R.-J. 2009, A&A, 506, 1123
Hennebelle, P. & Falgarone, E. 2012, A&A Rev., 20, 55
Jansson, R. & Farrar, G. R. 2012a, ApJ, 757, 14
Jansson, R. & Farrar, G. R. 2012b, ApJ, 761, L11
Kennicutt, Jr., R. C. 1981, AJ, 86, 1847
Kennicutt, Jr., R. C., Armus, L., Bendo, G., et al. 2003, PASP, 115, 928
Krause, M. 2009, in Revista Mexicana de Astronomia y Astrofisica Conference Series, Vol. 36, Revista Mexicana de Astronomia y Astrofisica Conference Series, 25–29
Krause, M. 2014, ArXiv e-prints
Kulpa-Dybeł, K., Otmianowska-Mazur, K., Kulesza-Żydzik, B., et al. 2011, ApJ, 733, L18
Mora, S. C. & Krause, M. 2013, A&A, 560, A42
Moss, D., Sokoloff, D., Beck, R., & Krause, M. 2010, A&A, 512, A61
Orlando, S., Bocchino, F., Reale, F., Peres, G., & Pagano, P. 2008, ApJ, 678, 274
Parker, E. N. 1971, ApJ, 163, 255
Parker, E. N. 1979, Cosmical magnetic fields: Their origin and their activity
Rohde, R., Beck, R., & Elstner, D. 1999, A&A, 350, 423
Shneider, C., Haverkorn, M., Fletcher, A., & Shukurov, A. 2014a, A&A, 568, A83
Shneider, C., Haverkorn, M., Fletcher, A., & Shukurov, A. 2014b, A&A, 567, A82
Soida, M., Krause, M., Dettmar, R.-J., & Urbanik, M. 2011, A&A, 531, A127
Sokoloff, D. D., Bykov, A. A., Shukurov, A., et al. 1998, MNRAS, 299, 189
Sokoloff, D. D., Bykov, A. A., Shukurov, A., et al. 1999, MNRAS, 303, 207
Steenbeck, M. & Krause, F. 1966, Zeitschrift Naturforschung Teil A, 21, 1285
Strong, A. W., Moskalenko, I. V., & Ptuskin, V. S. 2007, Annual Review of Nuclear and Particle Science, 57, 285
Tabatabaei, F. S., Schinnerer, E., Murphy, E. J., et al. 2013, A&A, 552, A19
Tüllmann, R., Dettmar, R.-J., Soida, M., Urbanik, M., & Rossa, J. 2000, A&A, 364, L36
Urbanik, M., Elstner, D., & Beck, R. 1997, A&A, 326, 465
Vainshtein, S. I. & Ruzmaikin, A. A. 1971, AZh, 48, 902
Walsh, W., Beck, R., Thuma, G., et al. 2002, A&A, 388, 7
Williams, A. & Heald, G. 2015, in prep
Yan, H. 2015, in Astrophysics and Space Science Library, Vol. 407, Astrophysics and Space Science Library, ed. A. Lazarian, E. M. de Gouveia Dal Pino, & C. Melioli, 253

Nederlandse Samenvatting

– vertaald door Dr. Tjarda Boekholt, auteur van ***Chaotic Dynamics in N-body Systems***.

Kosmisch Magnetisme in het kort

Toen je jong was heb je misschien weleens gespeeld met koelkastmagneetjes of was je geïntrigeerd door een kompas. Je hebt vast weleens geëxperimenteerd met staafmagneten en ijzervijlsel, zodat Fig. 6.1 je bekend voor zou moeten komen.

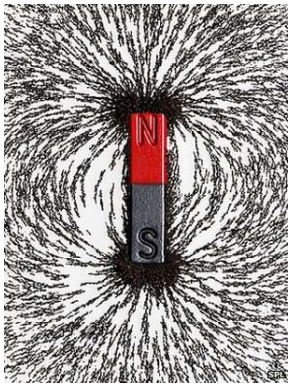

Figuur 6.1: Een staafmagneet met ijzervijlsel maakt de dipoolveldlijnen zichtbaar.
Bron: http://www.bbc.com/news/science-environment-25946734.

Deze figuur illustreert het dipool magnetisch veld. Deze veldconfiguratie functioneert als een simpele beschrijving van het magnetisch veld van de Aarde. Als we dit als een kompasnaald zouden beschouwen, dan zouden de 'N' en 'S' symbolen in Fig. 6.1 de richtingen van de magnetische noordpool en zuidpool aanwijzen. Echter, de 'N' en 'S' symbolen op het kompas corresponderen eigenlijk met respectievelijk de zuid- en noordpool van het kompasnaald zelf, omdat de tegenovergestelde polen elkaar aantrekken. Een dipoolveld is ook een veel voorkomende configuratie voor planeten (in het zonnestelsel) met een magnetisch veld. De aanwezigheid van een planetair magnetisch veld beschermt

ons tegen hoog-energetische straling uit de ruimte, die onze atmosfeer aan zou kunnen tasten, maar tevens ook de oorzaak is van spectaculaire lichtshows op Aarde - de Aurora Borealis/Australis, afhankelijk van of je op het noorderlijk of zuiderlijk halfrond bent. Het magnetisch veld van de zon, behalve dat het de buitenste lagen van de zon's atmosfeer verwarmt, draagt ook bij aan het weer in de ruimte door middel van de zonnewind, coronale massa ejecties (CME), en zonnevlammen die invloed hebben op ruimtemissies, radio- en satellietcommunicatiestoringen en overbelasting van elektriciteitsnetten. Hoewel bacteriën, geleedpotigen, weekdieren en een groot aantal gewervelde dieren reeds lange tijd zich al oriënteerden aan de hand van het magnetisch veld van de Aarde, was het pas in de 11^{e} eeuw dat de mens voor het eerst een magnetisch kompas gebruikte voor navigatie. Het jaar 1600 was een mijlpaal voor de studie van het aardmagnetisme, door de publicatie van William Gilbert's werk "Over de Magneet en Magnetische Lichamen, en de grote Magneet van de Aarde,"dat een experimenteel fundament legde voor de idee van de Aarde als een magneet. Aan het einde van de 17^{e} eeuw bracht Edmond Halley[1] grofweg de ruimtelijke variatie in het magnetisch veld weer, in een gebied van de Atlantische Oceaan tussen $+52^{\circ}$ en -52°. De uitbreiding van ons 'magnetisch universum' werd dramatisch versneld in de 20^{e} eeuw door ontdekkingen van onder meer zonne-magnetisme in 1908, galactisch magnetisme in 1949 en extra-galactisch magnetisme in 1972. Magnetische velden zijn alomtegenwoordig in het universum: op planeten (die een gesmolten kern hebben), sterren (waarvan inelkaar gestorte sterren de grootst bekende veldsterkte hebben in het heelal - ongeveer een miljard keer de sterkte van een MRI scan), accretieschijven, stralen van gas ook wel 'jets' genoemd, interstellaire wolken, overblijfselen van supernova explosies, het ijle gas tussen de sterren, sterrenstelsels, het zeer ijle gas tussen de sterrenstelsels in draadvormige structuren, clusters van sterrenstelsels, en de grootste schaal die clusters van sterrenstelsels met elkaar verbindt. Al deze studies van magnetische velden over een enorm bereik in ruimte en tijd, vallen samen onder de paraplu van *Kosmisch Magnetisme*. Voor meer informatie over Kosmisch Magnetisme verwijs ik de lezer naar ***Extreme Cosmos*** van Bryan Gaensler en 'the Square Kilometre Array Cosmic Magnetism' website: https://www.skatelescope.org/magnetism.

Magnetische velden in sterrenstelsels

In dit proefschrift concentreren we ons op de galactische magnetische velden die door het interstellaire gas zijn geregen. Hierdoor beïnvloedt het magnetisch veld de dynamica en distributie van het gas. De typische sterkte van dit veld is van de orde een micro-Gauss, μG, wat een paar duizend keer sterker is dan het veld in onze hersenen, maar miljoenen keren zwakker dan die van een koelkastmagneet. De structuur van de veldlijnen lijkt ook totaal niet meer op die van een geïdealiseerde dipool als weergegeven in Fig. 6.1. In grote lijnen kunnen magnetische velden geclassificeerd worden naargelang ze zich voordoen op grote schaal of op een relatief kleine schaal. Het magnetisch veld op grote schaal volgt meestal het gas in de spiraalarmen van een sterrenstelsel (zie Fig. 6.2), en reikt

[1] van komeet Halley.

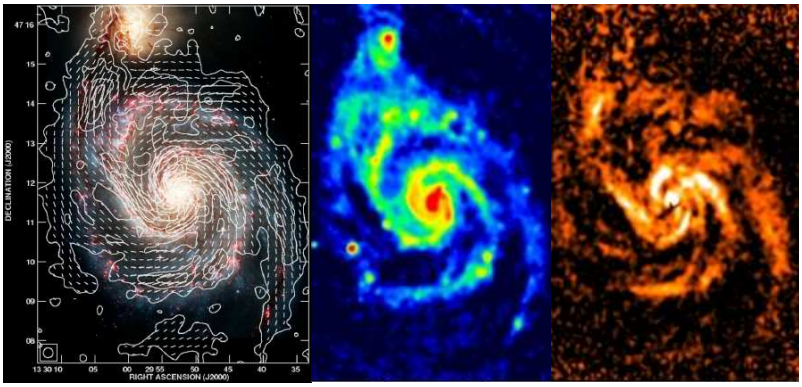

Figuur 6.2: Een spiraalstelsel met verschillende kleurcodering: optisch licht (links), totale radiostraling waarbij rood de hoogste intensiteit weergeeft (midden), en gepolariseerde radiostraling waarbij wit de hoogste intensiteit weergeeft (rechts). Deze afbeeldingen zijn gereproduceerd van de Atlas of Galaxies (MPIfR Bonn) beschikbaar op http://www.mpifr-bonn.mpg.de.

tot duizenden lichtjaren ver. In het linkerpaneel van Fig. 6.2 geven de kleine strepen de gemeten oriëntatie weer van het grootschalig magnetisch veld, die de spiraalarmen volgt zoals te zien is in de vergelijking met de afbeelding in het optisch licht. Aan de andere kant, een kleinschalig magnetisch veld bevindt zich in de turbulente omgevingen binnenin spiraalarmen, met een typische grootte van maximaal honderden lichtjaren. Deze schaal is nog steeds vrij groot als je bedenkt dat de afstand tussen de zon en de Aarde acht lichtminuten bedraagt[2]. Ontploffende sterren (supernovae) in spiraalarmen vormen de grootste leverancier van energie en kunnen zorgen voor krachtige, turbulente processen in het interstellaire gas. In analogie met een kosmische tsunami met een golf 200 miljard keer de diameter van de Aarde, wordt de energie verspreid op steeds kleinere schalen via wervelende, turbulente bewegingen in de golf, totdat een grootte van ongeveer tien keer de Aarde is bereikt, waarna de energie uiteindelijk afgevoerd wordt als schuim. Het kleinschalige magnetisch veld verwerft daarmee de afdruk van deze energieverdeling over ruimtelijke schalen of over het energiespectrum

Magnetische velden zijn onzichtbare krachtlijnen, hoe kunnen we dit fenomeen detecteren? Het antwoord ligt in de interactie tussen het magnetisch veld en hoog-energetische deeltjes, ook wel kosmische straling genoemd[3]. Wanneer zo'n deeltje een magnetisch veld treft, zal het een baan afleggen met een spiraalvorm rond de magnetische veldlijnen (zoals in Fig. 6.1), en zal hierbij een bepaald type straling uitzenden dat synchrotron-

[2]Een toeval in eenheden heeft een handige analogie tot gevolg: als de afstand zon-Aarde een inch zou zijn, dan correspondeert een lichtjaar met een mijl.

[3]Dit is geen gebruikelijke straling in de zin van fotonen met een variatie aan energie, zoals röntgenstraling of gammastraling die geen intrinsieke massa hebben, maar eerder deeltjes met een intrinsieke massa. Sommige van deze deeltjes kunnen ultra-hoge energieniveaus bereiken, waardoor hun impact vergelijkbaar is met die van een honkbal gegooid met een snelheid van 97 km/u.

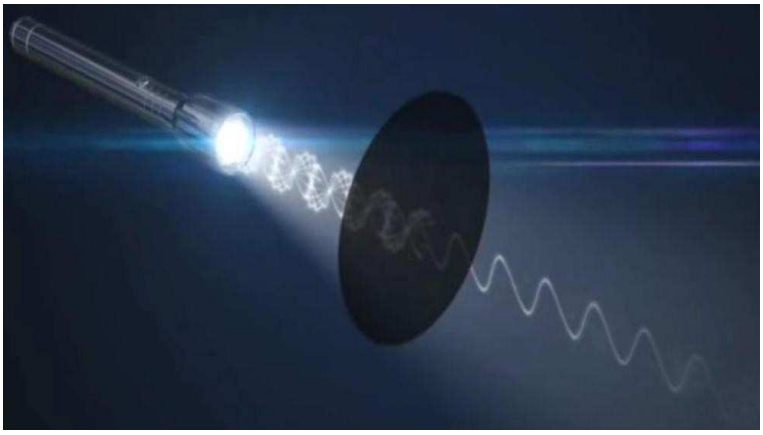

Figuur 6.3: Schematisch overzicht van polarisatie.
Dit is een snapshot van een animatie over gepolariseerd licht beschikbaar op 'the European Southern Observatory' op https://www.eso.org/public/videos/polarisedlight1, door ESO/L. Calçada.

straling genoemd wordt. Het middelste paneel in Fig. 6.2 geeft de sterrenstelsel weer in synchrotronlicht. Deze straling bevindt zich in de radio frequenties van het elektromagnetisch spectrum, met een frequentie hoger dan die van FM radio- en televisiesignalen, maar duizenden malen kleiner dan optisch licht[4]. *Radio-astronomie* is dus cruciaal voor de studie van kosmische magnetische velden.

Een belangrijk aspect van deze straling is dat het in hoge mate lineair gepolariseerd is, wat inhoudt dat de elektromagnetische golven oscilleren met een specifieke oriëntatie terwijl het beweegt langs een rechte lijn (oftewel niet in een cirkel). Zoals te zien is in Fig. 6.3, licht dat uit de zaklamp komt is niet gepolariseerd, omdat het is opgemaakt uit een som van elektromagnetische golven met een willekeurige bewegingsrichting. Echter, als er een filter (weegegeven door de donkere ovaal in de figuur) dat alleen maar verticaal gepolariseerd licht doorlaat, wordt geplaatst in het lichtpad, dan zal het licht daarachter recht naar boven en onder oscilleren zoals te zien in de afbeelding[5]. Vandaar dat de elektromagnetische oscillaties zich uitsluitend beperken tot de bewegingsrichting langs deze verticale vlak in de ruimte en in geen andere richting. Het licht is dus volledig gepolariseerd. Omdat de golf heen en weer beweegt heeft de lineaire polarisatie geen richting (bijv. naar boven of naar beneden) maar slechts een oriëntatie (naar boven en naar beneden). Dit is de reden dat in het linkerpaneel van Fig. 6.2 streepjes zijn weergegeven in plaats van vectoren. Stel dat de filter niet ideaal was en er een lek was zodat sommige andere oriëntaties door het filter konden dringen, dan zou de polarisatie 'vervuild' worden en dus gedeeltelijk gepolariseerd zijn. Dit fenomeen leidt tot het concept van de mate van

[4] Net zoals alle elektromagnetische golven reizen radiogolven met de lichtsnelheid.

[5] Eigenlijk wordt hier de elektrische oscillatie van het elektromagnetisch veld afgebeeld; de magnetische oscillaties staan altijd loodrecht op de elektrische oscillaties.

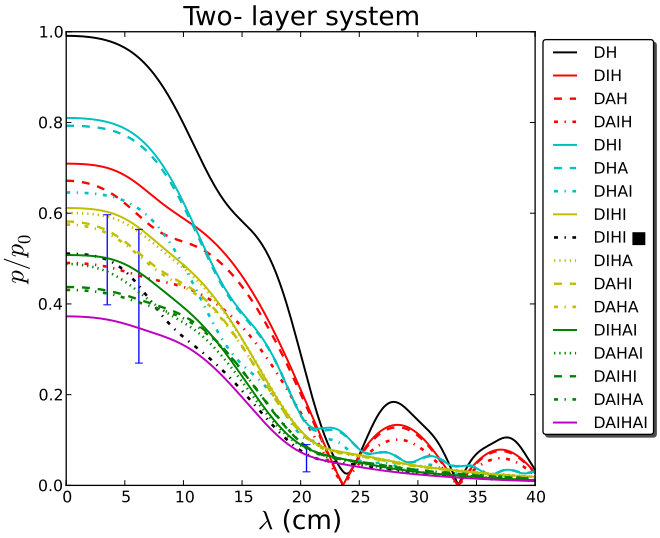

Figuur 6.4: Simulatie van de resulterende mate van polarisatie van synchrotronstraling als een functie van de waargenomen golflengte, voor alle mogelijke configuraties van het magnetisch veld, zoals het uit onze methode volgt.

polarisatie, wat aangeeft hoeveel polarisatie aanwezig is, oftewel, tot op welke hoogte het signaal gepolariseerd is. Terugkomend op de discussie over kosmische straling en magnetische velden, een grootschalig veld resulteert in synchrotronstraling van alle naburige kosmische stralen die nauw gesynchroniseerd zijn in hun oriëntatie, terwijl voor een kleinschalig veld, de naburige oriëntaties eerder willekeurig zijn. Uit deze beschouwing kunnen we al anticiperen op het feit dat een grootschalig magnetisch veld een hogere mate van polarisatie zal bezitten dan een kleinschalig veld. Als we het rechterpaneel van Fig. 6.2 nader bekijken, zien we dat er een hoge mate van polarisatie aanwezig is langs de spiraalarmen, wat overeenkomt met het grootschalig magnetisch veld.

Bovendien kunnen studies van magnetische velden in andere sterrenstelsels, waaronder sterrenstelsels met een zelfde morfologie als die van onze eigen Melkweg, zorgen voor een vogelperspectief op de globale structuur van galactische magnetische velden, die in- of uitgezoomde versies van de globale magnetische veldstructuur van de Melkweg kunnen zijn. Daarentegen, studies van de Melkweg zelf bieden vele malen hogere resolutie ongeëvenaard door elk ander sterrenstelsel.

Bijdragen van dit proefschrift

In dit proefschrift reconstrueren we de eigenschappen van magnetische velden in spiraalstelsels gebruikmakend van de polarisatie van synchrotronstraling. Het doel van dit

onderzoek is de structuur van het magnetisch veld te ontrafelen over diverse ruimtelijke schalen in onze Melkweg (zie Hoofdstuk 2), en de sterkte en structuur van magnetische velden in andere sterrenstelsels te karakteriseren (Hoofdstuk 3-5).

In Hoofdstuk 2 gebruiken we nieuwe simulatiemethoden om te bepalen wat de intensiteit is van zowel de totale synchrotronstraling als die van de gepolariseerde straling als een functie van diverse eigenschappen van het numeriek gegenereerde turbulente, magnetisch veld en interstellaire gas. Daarna vergelijken we de resulterende distributies in de structuur over verschillende resoluties van aan de ene kant de synchrotron-intensiteit met aan de andere kant het turbulente magnetisch veld. Uit dit experiment volgt dat de totale intensiteit het turbulente magnetisch veld volgt in termen van distributies van structuren, maar dat de onzekerheid in de observaties een voorspelling onzeker maken. Een voorspelling die we wel kunnen maken is dat voor zekere frequenties waarop waarnemingen gesimuleerd zijn, de polarisatie-intensiteit twee verschillende structuurdistributies kan aannemen, in plaats van een enkele. De karakteristieke schaal waar op deze splitsing optreedt is afhankelijk van de frequentie. Deze relatie kan gebruikt worden als een mogelijke indicator voor de bepaling van parameters die de turbulentie beschrijven.

In Hoofdstukken 3 en 4 concentreren we ons op het extraheren van informatie aangaande groot- en kleinschalige magnetische velden uit polarisatiekaarten voor een specifiek sterrenstelsel met meerdere waarnemingsfrequenties (oftewel, meerdere waargenomen golflengtes). We stellen een wiskundig raamwerk op die tegelijkertijd de invloed beschrijft van diverse belangrijke mechanismen voor de waargenomen mate van polarisatie van het synchrotronsignaal, Een eerste voorbereidingsstudie is uitgevoerd als een ‘proof of concept’ van onze methoden. Alle unieke combinaties van onze modellen zijn toegepast zoals te zien is in Fig. 6.4. Het diagram geeft de mate van polarisatie tegen de waargenomen golflengte (in centimeter). De legenda geeft de verschillende modellen weer. De blauwe, verticale lijnen staan voor de observaties samen met de onzekerheid in die observaties. De modelcurves die door alle datapunten gaan zijn meer plausibel dan de andere modellen. We modelleren een sterrenstelsel ook als een boterham met verschillende lagen, bestaande uit een variërend aantal interstellaire gaslagen. Vervolgens passen we onze modellen toe op de gehele sterrenstelsel zodat we voorspellingen kunnen maken voor de groot- en kleinschalige structuur van de magnetische veldsterkte.

In Hoofdstuk 5 modelleren we zogenoemde ‘X-vorm’ magnetische velden in sterrenstelsels die uitstekende multi-golflengte data beschikbaar hebben. Recent onderzoek heeft uitgewezen dat in de buitenste regionen van een sterrenstelsel een grootschalig, verticaal magnetisch veld aanwezig kan zijn, met een richting die uit het sterrenstelsel wijst. Men denkt dat dit fenomeen vaak voorkomt in spiraalstelsels en dus moet deze complexe structuur meegenomen worden. Ons ab-initio model geeft waarden voor de grootschalige magnetische veldsterkte die consistent is met literatuurwaarden, maar alleen als er extra complexiteit aan het model toegevoegd wordt.

English Summary

Cosmic Magnetism in brief

As a young person you may have displayed interest in fridge magnets and been intrigued by a compass. Perhaps you may also have tinkered with bar magnets and iron filings in which case 7.1 would be familiar.

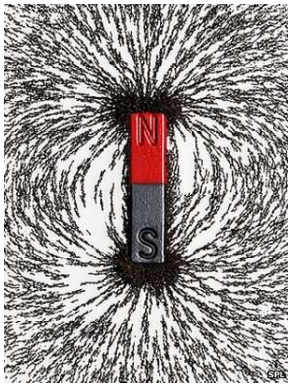

Figure 7.1: Bar magnet with iron filings tracing the dipole field lines.
Source: http://www.bbc.com/news/science-environment-25946734.

In fact, Fig. 7.1 illustrates a dipole magnetic field. Such a field configuration serves as a simple description of the Earth's magnetic field. If this were a compass dial, the 'N' and 'S' labels in Fig. 7.1 would indicate the direction of Earth's north and south magnetic poles. However, the 'N' and 'S' labels on the compass actually correspond to the south and north poles of the compass needle itself, respectively, as it is opposite poles that attract. A dipole field is also the dominant mode in planets (in the solar system) which have a magnetic field. The presence of a planetary magnetic field both shields us from high-energy radiation from space, thereby protecting our fragile atmosphere and, at the same

time, conducts the greatest light show on Earth - the Aurora Borealis/Australis, depending on whether one is in the northern or southern hemisphere. The sun's magnetic field, besides heating the outer atmosphere of the sun, contributes to our space weather through solar wind, the release of coronal mass ejections (CME), and solar flares which can affect space missions, disrupt radio and satellite communication, and overload power grids. Although bacteria, arthropods, mollusks, and a very large number of vertebrates had long obtained their bearings via Earth's magnetic field, it was not until the 11th century that a magnetic compass was first used for navigation by humans. Sixteen hundred was a landmark year for terrestrial magnetism with William Gilbert's treatise "On the Magnet and Magnetic Bodies, and on the Great Magnet the Earth" providing an experimental basis for the notion of 'Earth as a magnet'. At the close of the 17th century, Edmond Halley[1] boldly charted the magnetic spatial variation in a region of the Atlantic spanning 52° north and 52° south. The expansion of our 'magnetic universe' was dramatically accelerated in the 20th century by the discoveries, among notable others, of solar magnetism in 1908, galactic magnetism in 1949, and extra-galactic magnetism in 1972. Magnetic fields are ubiquitous throughout the universe: on planets (where there is a molten core), stars (of which collapsed stars have the highest known field strengths in the universe - about a billion times the strength of a medical MRI), accretion disks, jets, interstellar clouds, supernova remnants, the tenuous gas between stars, galaxies, the highly rarefied filamentary gas between galaxies, galaxy clusters, and at the largest scale of connecting galaxy clusters. Their study over these vast spatial and temporal scales comes under the umbrella term of *Cosmic Magnetism*. For further popular reading on Cosmic Magnetism please consult, for example, ***Extreme Cosmos*** by Bryan Gaensler and the Square Kilometre Array Cosmic Magnetism website: https://www.skatelescope.org/magnetism.

Magnetic fields in galaxies

In this PhD thesis we focus on galactic magnetic fields as they thread the interstellar gas. Magnetic fields are very important since they affect the dynamics of the gas as well as the gas distribution. The magnetic field strengths dealt with here (micro-Gauss, μG) are several thousand times stronger than those in our brain but still several million times weaker than a typical fridge magnet. The field's structure is also far from the idealized dipole field configuration shown in Fig. 7.1. Broadly speaking, magnetic fields are classified according to whether they occur on large scales or small scales. A large-scale field is a field that typically follows the spiral shape of the gaseous arms of a galaxy as in Fig. 7.2 and extends to at least several thousand light years. In the left-most panel of Fig. 7.2, the small dashes denote the measured orientation of the large-scale magnetic field which visually traces the orientation of the spiral arms of the galaxy. A small-scale magnetic field, on the other hand, is at spatial scales of turbulent processes that occur within the spiral arms, and extends over distances of at most several hundred light years. This distance is still quite vast when one considers that the Earth is located at only a bit over eight light

[1] Of Halley's Comet.

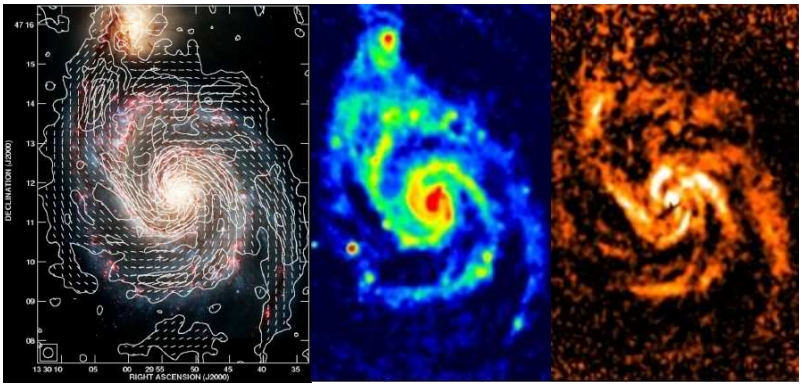

Figure 7.2: A spiral galaxy shown with a color scheme for (left) optical light, (center) total radio radiation with red denoting high intensity values, and (right) polarized radio radiation with white denoting high polarized intensity values. Images reproduced from the Atlas of Galaxies (MPIfR Bonn) available at http://www.mpifr-bonn.mpg.de.

minutes from the Sun[2]. Stellar explosions (supernovae) in the spiral arms yield the largest source of energy input and, consequently, stir up turbulent processes in the interstellar gas most vigorously. In analogy with a cosmic tsunami wave measuring 200 billion Earth diameters across, energy from a supernova is cascaded to ever smaller scales via whirling turbulent motions in the wave until about 10 Earth diameters is reached at which scale the energy is finally dissipated as froth. The small-scale magnetic field thus acquires the imprint of this energy distribution across spatial scales or energy spectrum.

Magnetic fields are invisible lines of force so how is it possible to detect their presence? The answer is provided by the interaction between the magnetic field and highly energetic particles called cosmic rays[3]. Upon encountering magnetic fields, cosmic rays begin to spiral around the field lines (e.g., as in Fig. 7.1), emitting a type of radiation known as synchrotron radiation in the process. The central panel of Fig. 7.2 reveals a galaxy in synchrotron radiation. This radiation occurs at the radio frequency range of the electromagnetic spectrum with frequencies typically higher than those carried by FM radio and TV signals but still many thousands of time smaller than the frequency of visible light[4]. Hence, *radio astronomy* is very important for the study of cosmic magnetic fields.

A key aspect of this radiation is that it is highly linearly polarized, meaning that the electromagnetic wave oscillates with a certain orientation as it moves along a straight path (i.e., not in a circle). As illustrated in Fig. 7.3, light streaming from the flashlight is unpolarized as it is composed of a sum of electromagnetic waves propagating in random

[2]A coincidence among units allows for a simple distance analogy: if the Earth-Sun distance is scaled to one inch, then the light year on this scale corresponds to one mile.

[3]These are not actual 'rays' which are names given to photons of different energies (e.g., X-rays) which have no intrinsic mass but are rather particles with an intrinsic mass. Some of these particles can achieve ultra high energy levels making their impact comparable to that of a baseball pitched at 60 mph (97 kph).

[4]Just as all electromagnetic waves, radio waves travel at the speed of light.

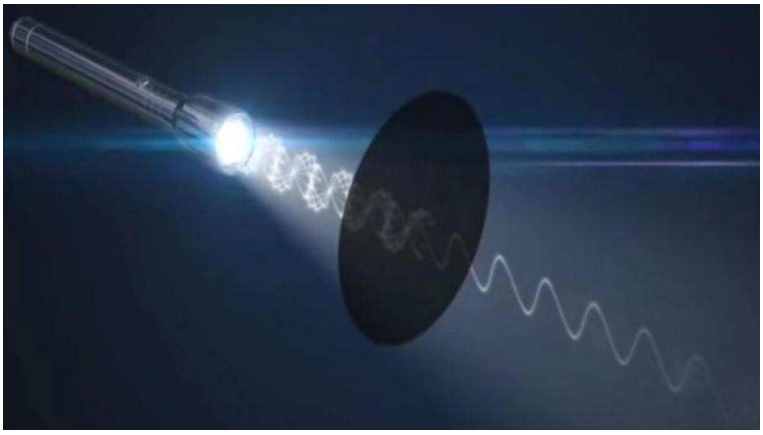

Figure 7.3: Schematic of polarization. Still from an animation on polarized light available from the European Southern Observatory at https://www.eso.org/public/videos/polarisedlight1. Credit: ESO/L. Calçada.

directions. However, when a filter (represented by the dark filled oval) that transmits only vertically polarized light is placed in the beam's path, the emerging light behind the filter oscillates straight up and straight down in the example shown here[5]. Hence, the electromagnetic oscillations are restricted to move only along this vertical plane in space and no other. This light is thus completely polarized. Since the orientation is both up and down there is no single 'direction' but rather a bi-direction. This is the reason for the dashes in the left-most panel of Fig. 7.2 instead of vectors. Were oscillations with a different orientation to hypothetically leak through the filter, the polarization would become 'diluted' and so partially polarized. This naturally leads to the notion of the degree of polarization which indicates how much polarization there is or, equivalently, to what extent or degree the signal is polarized. Returning to our discussion on cosmic rays and magnetic fields, a large-scale field would result in synchrotron emission from all neighboring cosmic rays which is closely synchronized in orientation, while for a small-scale field such neighboring synchrotron emission would already be randomly oriented. From this consideration we might already anticipate a higher degree of polarization from large-scale magnetic fields than from small-scale magnetic fields. Examining the right-most panel of Fig. 7.2 reveals a high degree of polarization tracing the spiral arms coinciding with the presence of the large-scale magnetic field.

Moreover, studies of magnetic fields in other galaxies, including galaxies that may be morphologically similar to our own Galaxy, provide a 'bird's eye view' of global magnetic field structures that may indeed be zoomed-out versions of the global magnetic field structure of the Milky Way. In contrast, studies of the Milky Way provide spatial detail that is unrivaled by any other galaxy.

[5]What is shown is actually the electric oscillations of the electromagnetic wave; the magnet oscillations are always perpendicular to the electric oscillations

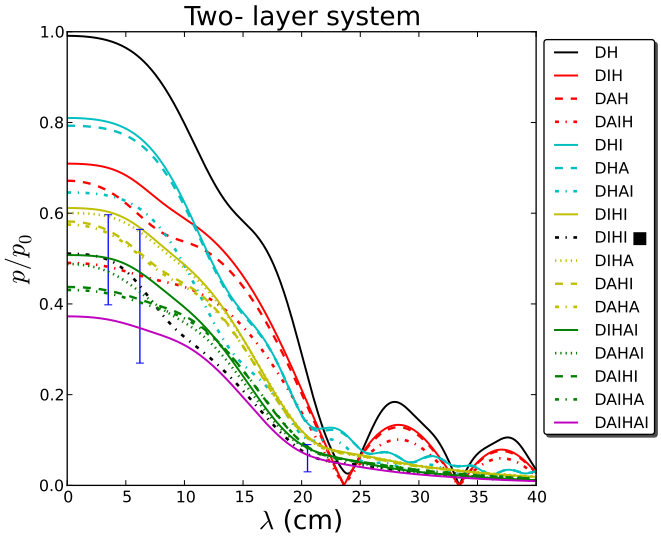

Figure 7.4: Simulation of the resulting degree of polarization of synchrotron radiation as a function of observing wavelength for all possible magnetic field configurations based on our approach.

Contributions of this thesis

In this thesis we reconstruct properties of magnetic fields in spiral galaxies by means of the polarization of synchrotron radiation. The goal of this research project has been to infer the structure of the magnetic field across various spatial scales in our own Galaxy (Chapter 2) and the strength and structure of the magnetic field in other galaxies (Chapters 3 - 5).

In Chapter 2, we use novel methods to simulate both total synchrotron intensity and polarized synchrotron intensity for our own Galaxy by varying certain properties of the numerically generated turbulent magnetic field and interstellar gas. We then compare the resulting distribution of structure across spatial scales between these synchrotron intensities on the one hand, and turbulent magnetic fields on the other. We find that total intensity traces the turbulent magnetic field in terms of such a distribution of structure but that uncertainties in the measurement make actual predictions unlikely. A further prediction of our model is that for certain frequencies at which observations are simulated, the polarized intensity acquires two different distributions of structure, instead of a single distribution. The scale at which the break occurs has a frequency dependence. This, in turn, can serve as a possible marker for establishing turbulence parameters.

In Chapters 3 & 4, we focus on extracting information on large- and small-scale magnetic fields from degree of polarization maps determined for a specific galaxy at several

observing frequencies (or, similarly, observing wavelengths). We, therefore, establish a mathematical framework for describing the simultaneous influence of several physically relevant mechanisms on the measured degree of polarization of the synchrotron signal as it propagates through this galaxy. A preliminary small region study was first performed as a proof of concept of our methods. All possible unique model combinations using our methods were applied as shown in Fig. 7.4. This figure is a plot of the degree of polarization on the y-axis versus the observing wavelength (in centimeters) on the x-axis. The legend displays the different models. The blue solid vertical bars denote the actual measured values along with the associated uncertainty in those measurements. Curves passing through all of the data are more plausible than the other models. We also model the galaxy as a multilayer sandwich composed of varying interstellar gas layers. Subsequently, we applied our methods to model the entire galaxy and were able to make robust predictions for large- and small-scale magnetic field strengths.

In Chapter 5, we model so called 'X-shape' magnetic fields in a galaxy for which excellent multiwavelength data are available. It has recently been realized that at the outskirts of galaxies there can be large-scale vertical magnetic fields that point away from the galaxy. As this configuration is thought to be common in spiral galaxies, the inclusion of such complex geometries is necessary. Our ab-initio model yields large-scale magnetic field strengths consistent with literature values but requires additional complexity to fit the data well.

Acknowledgements

Like in Xander's comparison of the PhD to "being on a boat that encounters a storm at sea which is then miraculously calmed," with reference to Rembrandt's 'The Storm on the Sea of Galilee', this PhD voyage, an Odyssey really, has, at times, made me feel like being able to walk on the moon's 'Sea of Tranquility'. I am so very grateful and fortunate to have overlapped paths with many genuinely kind, awesomely wonderful, and brilliant people during all of these 5+ years! It is really impossible to thank everyone properly here, thus I will try an abridged version. My most sincere apologies to anyone whose name may have been omitted.

I would like to begin by thanking my supervisor Marijke for hiring me as a PhD and for this 'quenching and toughening' PhD journey. It has been outstanding to receive your supervision at ASTRON during my first year and at Nijmegen during the past four years. And it is also so wonderful that you have become a proud mom of Tijn and Jochem!

Huub, thank you for being my formal promoter, for your great genuine support, and for your most kind hospitality, extending my time to be a guest of Leiden University in order for me to complete my PhD in the Netherlands. This extension has also relieved the enormous time pressure of finding a job right away. It had indeed been an 'ontzet'. Xander, thank you for so thoroughly monitoring my progress and for your sagacious guidance.

Remo, thanks for your most kind and helpful advice on my career path and scientific programming. Evelijn, you have been most wonderfully kind from the very first day of my becoming a member of the Sterrewacht Family and, all these years, you have made the Sterrewacht really feel like a good big Family. Muchisimas gracias para todo! Alexandra, thank you for being so kind and wonderful. Ogromnoye Vam spasibo za vashu teplotu! Yvonne, thank you for your most helpful assistance all these years, your great kindness, and most valuable advice! Hartelijk bedankt! A big thanks also to Remôn, Esther, and Liesbeth for your HR help. Many thanks to Anita, Debbie, Liesbeth, and Jacqueline for your help over the years including the PhD colloquia. One very big thank you to Jeanne Drost!

A special thanks to the following Faculty at the Sterrewacht: Koenraad, Vincent, Si-

mon, Joop, Ignas, Paul, Michiel, Walter, Anthony, Henk, Jarle, Bernhard, Matthew, Harm, Jan, Frank, Elena, George, Marijn, Richard, Ewine, Rudolf, Harold, Peter and Jet.

Erik, thanks for kindly sharing your computing expertise and experience. It was great fun to accompany you as Sinterklaas with Heather and myself as fellow Piets. David, thanks for your most kind assistance and patience with all possible computer queries. Aart, thanks for your great humor and for producing works of Aart. The 1 April purchase of a mini-notebook through the computing office was marvelously executed. Congratulations gentlemen!

To my friend and PhD colleague Marco, you are a trailblazer. Thanks for cheering me on and for your friendly encouragement. The many Karalis' pizzas and at Bocconi that we enjoyed were indeed delizioso! Of course, Carmen makes the best tiramisu. Congratulations to you and Carmen on becoming proud excellent parents of your little one, Lorenzo (di Medici)! Best wishes and warmest thanks to your parents Piero and Rosa for hosting me so generously when you invited me to visit you in Rome. Greetings to Alessandro and all your wonderful friends who I was privileged to meet in Rome and to your Leiden neighbor Riccardo C.

Irene, thanks for being such a warm and kind person (happy that you liked the bagel place in Leiden). Success to you with everything! Cameron, great meeting you and best of everything! Dave, great meeting you and congratulations to you and Vera with your wonderful boy Henry! Lauranne, it was delightful to do a bit of French-Russian tandem with the ageless 'The Little Prince'.

To my office mates at #404, by now we have all undergone a diaspora. You are all really amazingly awesome! Sebastiaan (Bas) Krijt, thanks for being such a great person and good friend. Thank you for most kindly always helping with questions and thinking along with me. You deserve a Ballon d'Or for excellence in the sciences and sports! Congratulations to you and Florie! Great success in Chicago and in all your endeavors! Caroline, with the best British accent that I can muster: thank you for being extraordinary. I do hope for many high teas in your fantastic future and an absolutely fabulous job. A cheery day to you. Paula, gracias para estar tan simpática. Es un placer estar tu compañero de oficina y recibir tus enormes abrazos. Buena suerte con todo! Bram, congratulations to you and Angélica on becoming proud and loving parents of your beautiful baby girl Jule! Great success at Johns Hopkins! Xiaohu, thanks for being a good friend! It was great to be a paranymph for your PhD defense! Thanks for good times discussing philosophy, playing ping pong, and for being always welcome at your home. Thanks to you and your wife for your hospitality and delicious cooking! Congratulations Xiaohu on your successes and the best of times to you and Changchun on becoming wonderful proud parents! Francisco, thanks for good times and jazz concerts. Success in Germany! Tjarda, thank you for your good thoughtful suggestions regarding computing and for most kindly translating the summary!

Thanks to all my QRAVEL tennis club colleagues for great tennis over the years!

It is a great pleasure to be able to express a big thanks to both present and 'old guard' Sterrewacht and Leiden University friends and colleagues: Ted vd A., Fritz V., Ali R. and Maryam S., Thibaut P., Yuri C., Daniel R., Atakan G., Raymond O., Rowin M., Jeroen B., Nadine W., Lars K., Stefania G., Liesbeth V., Ernst K., Edo L. and Alicia B. A.,

Jeanette B., Kalle T., Karoliina I., Joseph G., Sergio I., Freeke vd V., Olivera R., Ben O., Simone W., Moein M., Steven R., Isa O., Craig B., Arthur B., Umut Y., Edith F., Carina A., Rafael G., Karl J. R., Willem de P., Silvia T., Tjbaria P., Ainil A., Koen M., Tim v W., Gerard v H., Matteo B., Irene S. J. G., Berenice P. D., Jelte de J., Mattia F., Nicola C., Silvia V., Thanja L., Daniel H., Gilles O., Sascha Z., Babs B., Joris H., Mher K., Emanuele di G., Gleb F., Junfeng Z., Steven C., Nienke vd M., Jesse vd S., Renske S., Rob C., Daniel S., Remco vd B., Stefano V., Vicente A., Maria de J. O., Nikki Z., Jens H., Marco V., Gabriela R., Alex Rimoldi, Alex Richings, Noel G., Carmen B., Heather A., Monica T., Daniel P., Niels L., Stefanie H., Igone U. A., Margot B., Edwin vd H., Anna-Lea L., Julien S., Alex P., Pedro R., Jaya R., Mihkel K., Magnus P., Nadieh B., Tiffany M., Marissa R., Wendy W., Leah M., Alan H., Lucie J., Jean-Baptiste B., Anton W., Jeroen F., Henriette S., Andrew R-H., Josha v H., Pedro M., Mieke P., Edwin M., David C.

It's always amazing to see the 'Great Wall' of eminent Astronomers, Physicists, and Mathematicians that have presented the Colloquium Ehrenfestii, displayed in the Oort building. Thank you to the Mayor of Leiden, Henri J. J. Lenferink, and Director of the Museum De Lakenhal, Meta Knol, for the most wonderful Expat breakfast and curating the Gerrit Dou exhibit. Thank you to Mr. Wouter Kuiper, an extraordinary 80+ year young architect, painter, historian, and author for recounting for me a personal history of Paul Ehrenfest and Dutch architectural history, and for being an excellent special guide to the residence of Paul Ehrenfest. It has been historically amazing to meet the granddaughter of Adriaan Fokker[1], Evelien, who is a wonderful cello instructor.

It has been really great to be a part of the great Easter lunches, Paper cakes, and Christmas poems and dinners of the Radboud Astronomy Department! Esther, thanks for your wonderful cheerfulness, kindness, and your excellent advice to find where Sven works regarding my great interest in genetics and cancer research. Marja, thanks for your happy laughter and kindness! Great strength to you with everything! Cisca, thanks for your kind help!

A special thanks to the following Faculty Members at the Radboud Astronomy Department: Paul, Onno, Heino, Jan, Jörg, Gijs, Bram, and Elmar.

Thank you to the excellent colleagues at the Radboud Astronomy Department, both present and past, who I had the privilege to know: Sander ter V. (werewolf champion), Pim S., Sarka W., Sjoert v V., David C., Serena R., Thomas W., Marianne H., Satyendra T., Carlo A., Emilio E., Sweta S., Joke C., Christiaan B., Deanne and Rocco C., Sally M., Roque C., Payaswini S., Martha S., Johannes S., Monika M., Ester A., Laura R. and Antonio B.

In my first year of the PhD, I met many excellent people at ASTRON. Thus, A big thanks to: Michael G., Ger de B., Michiel B., George H., Michael W., John M., Roberto P., Manu O., Vibor J., Panos L., Vlad K., and Alex S.

I would also like to express a deep thanks to several amazing people at the Max Planck Institute for Radio Astronomy and the Argelander Institute for Astronomy, comprising the DFG research unit 1254 in Bonn (some have by now moved, though they will remain in my memory): Rainer B., Uli K., Elly B., Wolfgang R., Richard W., James A., Marita K.,

[1] Of the Fokker-Planck equation.

Dominic Schnitzeler, Aris N., Masaya K., Nadya B. B., Alice di V., Andreas H., Monica T., Carlos S., Charlotte S., David M., Amrita P., René G., Björn A., Carolina M., Jana K.

It has been absolutely great to meet the following people among the cosmic magnetism community: Cathy H., Katia F., Bryan G., Alexander S., Axel B, Kandu S., Detlef E., Katarzyna O-M., Krzysztof C., Dmitry S., Rodion S., Oliver G., Ralf-Jürgen D., David M., Andrew S., Paul B., Jo-Anne B., Fatemeh T., Volker H., Jongsoo K., Tony B., Anna S., Thorsten E., Mike B., Matthias H., Michael H., Dominik Schleicher, Ralf K., Harald L., Enno M., Alexii N., Niels O., Marcus B., Klaus D., Federico S., Franco V., Annalisa B., Rosita P., Gianfranco B., Francesco de G., Reinout v W., and Arpad M.

It has indeed been a pleasure and a great honor to be a research visitor at the School of Mathematics and Statistics at Newcastle University, hosted by Anvar and Andrew. My sincere thanks to all the wonderful people who I was most fortunate to meet there and to remember your friendly faces and our conversations, though a layer of memory dust sits on the names for the moment...Fred G., Andrew S., Irina M., Graeme S., Andrew B., Joy A., Holly A., Kavita G., Nur M., Michael B. (chess), Anthony Y., Donatello G., and Nikolaos P. Thank you! And, of course, the most deepest thank you for all your immense kindness, sea of wisdom and guidance, generosity of your time in closely working with me, and awesome hospitality, to my dearest co-authors and research supervisors who most kindly invited me to their magnificent castle, to you dear Anvar and Andrew, this PhD thesis owes a very great deal!

I would like to express a deep thanks to my Professors at Utrecht University: Bernard Q. P. J. de Wit, Cristiana de Morais Smith, Rembert Duine, Gleb Arutyunov, Peter Hoyng, John Heise, Jan Ambjørn, Heinz Hanßmann, Tomislav Prokopec. A deep thanks to my Professors at the University of Cambridge: Robert C. Kennicutt Jr., Wyn Evans, Michael R. E. Proctor, John D. Barrow, Anthony D. Challinor, Michael B. Green, Anne-Christine Davies, Orsola R. Spivack, Irena Borzym.

Thanks to enchanting Leiden and Universiteit Leiden that became my home for all these years, and to the loving house of Hans and Nelleke with their beautiful family and the warm times and Christmas dinners, while being their tenant on Rijnsburgerweg for the past 50 months. Thanks also to the warm and friendly people in the neighborhood: Linda and Jan, Amin, Kirsten, Joost and his mom, Andries Plu, Lucien K., Marieke and Elisabeth Dietz, Tiny, Elizabeth.

Thank you for everything to my close friends and outstanding colleagues from outside the aforementioned places: Bertram and Anne and Family, Martijn and Ninke, Martin and Ursula, Marco and Carmen, Anton K., Sasha P., Dima M., Andrei M., Jakob K., Brother Chris S. P. W. of one-happy-island Aruba, Irina and Amanda, Kalani, Han and Conny, Bas Kwaadgras and Marina, Jasper v. H., Joost de G., Stefanos K., Miriam L., Sam and Rosanne, Hedwig and Bas F. A., Sander W., Mathijs W., Kiril H., Alvaro O., Rao H. V., Lakshmi K., João Laia, Simon E. N., Nick Whitehead, Pooya S., Ivano C., Chervin L., Subrata R., Jacob A., Louis D., Berend E., Eric-Wubbo L., Marina B., Vivienne and Ted, Silvia L., and Linda W. and her artistically and musically talented friends.

To remarkable Mathilde A., with my deepest bow and most loving gratitude, forever thank you for sharing with me your warmth, beauty, and love for the precious time that we shared together. Thank you for inspiring me to pursue new avenues in life. Memories

of you are forever cherished in my heart and the Chaconne will always remind me of the Night of the Violin. Great success to you in breast cancer research and pathology. Greetings to your friends.

Thank You Prof. Niko Beerenwinkel for your most generous invitation to ETH, Basel and for considering me for a post-doc position in genetics and cancer research.

Thank You Prof. Bram van Ginneken and Sven Lafebre for hiring me. Looking forward to start as a scientific programmer and researcher with you!

Thank You dear Prof. Fröhlich for your continuing correspondence with me and, with your boundless kindness, always gifting me with your great Advice! Thank You to Ms. Rita G. P. for your absolutely wonderful correspondences and poetry. Thank You to Ms. Judith C. for your Cambridge correspondences.

A very big special thank you to George McCray and Yvonne and Shaka and beautiful Family for your Family love and great Christmas time in your home. Hope to see you soon! A very big special thank you to Mr. & Mrs. Rock 'n Roll René Shuman & Angel-Eye for coming down to Leiden to give a concert at the Leidse Schouwburg and meeting with me after so many years. Thank you for all those invitations to your great concerts. Perhaps the following quote from Elvis Presley is appropriate to describe you on the stage: "A live concert to me is exciting because of all the electricity that is generated in the crowd and on stage. It's my favorite part of the business, live concerts." Your fondness for Nikola Tesla is carried through your electric connection with the crowd, making your live concerts so recharging! I hope when my parents visit the Netherlands, we'll let the good times roll...

This thesis is dedicated to my loving Parents who have always been there with me at every moment throughout my whole life and their Guidance has made it possible for me to maintain the necessary focus to complete all the herculean tasks along this PhD journey. Thank You for making my childhood, teenage years, and adulthood so very special! Thank You for being so absolutely Happy for me and also to worry for me all these years. I do miss you very much!

I am very thankful to my Grandparents for their love, support, and infinite patience in waiting for my aperiodic phone calls. May again and again we shout "Hurrah, hurrah, hurrah!" together! To my maternal Grandpa: bisel glik, a bi gezunt! Es gezunterheyt! And with this thesis, I would like very much to honor the memory of my late Grandma, lovingly called Baba Rima (d. 2013), who always wished for me to achieve great things in life.

About the Author

When I was around 3 years of age, my grandparents, who, prior to my birth, had settled in Brooklyn, New York, traveled to Amsterdam, bringing back beautiful wooden miniature Dutch sail ships. I remember dreaming to see these in a real life. They recall the déjà vu feeling of seeing much of their beloved St. Petersburgs public squares, canals, and bridges appear right before their very eyes in Amsterdam. And as soon as I was born, the Netherlands / St. Petersburg 'looking-glass' became part of the Dutch thread that has always been running through my life, but allow me to start from the very beginning...

Indeed, Tsar Peter the Great had invited Dutch architects to make his great vision of a new port city real; a bright 'window to Europe'. Supervised by the Tsar himself, construction of St. Petersburg began on 27 May 1703 on Zayachy[1] Ostrov. The first Russian atlas, 'Atlas of Cruys'[2], was published in Amsterdam in 1703-1704.

In 1712, St. Petersburg became the capital of Russia and, with time, it blossomed into a great cultural center of art, classical music, literature, theater, ballet, and science. The Hermitage, Peterhof (Dutch for 'Peter's Court'), St. Isaac's Cathedral, the world-renowned Mariinsky Theater are among prime examples. In 1726, Peter the Great invited Professor Willem Jacob s Gravesande of Leiden University to set up the Academy of Sciences in St. Petersburg. Several years prior, the Tsar himself had traveled to the Netherlands where he lived and studied shipbuilding in Amsterdam and Zaandam. Tsar Peter's House, along with a monument, are to be found in Zaandam and a life-size statue of Peter the Great, in Rotterdam.

Two centuries later, this same city became a happy home for my paternal great-grandparents' family: a college mathematics pedagogue and his wife, a beautiful nurse with a Bachelor's degree, and their two young children, a son and a daughter - my grandmother who used to tell me so many fascinating stories about St. Petersburg. Stories about the birth of a marvel that began with the construction of a 'Petropavlovskaya Krepost', the citadel of St. Petersburg, named after the Apostles Peter and Paul, and designed to protect

[1] Russian for 'hare' or 'rabbit'.

[2] Cornelius Cruys (1655 1727) was a Dutch Vice Admiral of the Imperial Russian Navy and the first commander of the Russian Baltic Fleet.

the entrance of the river Neva's delta from constant attacks by the Swedish flotilla ('Trubetskoy', one of the bastions of the citadel, had a wind-mill), buildings whose facades were composed of muses and mythological figures, and how the city's 273 islands were, one by one, linked by beautifully decorated bridges and draw bridges, that allowed tall ships to continue their journey... My grandma would also tell me about her brave journey through WWII, how the war began and how suddenly she lost her father, then younger brother, and finally her beautiful mother and became a 15 year old Jewish orphan surviving in a frozen city through two and a half years of unbearable hunger during Leningrad's Blockade, known as the Siege of Leningrad, by the Nazis. (Saint Petersburg had been renamed to Leningrad in 1924 and then rechristened in 1991.)

Thanks to the great aid of the Dutch Consulate in Russia, my parents and grandparents on both sides of the family, unbeknownst to each other at the time, were able to leave Russia and emigrate to the US. They eventually settled in Brooklyn, New York in the historic Coney[3] Island area.

It is in Coney Island that my parents met. (It's puzzling that my parents had always resided near each other: my maternal grandparents' apartment were my mother lived, was located in a building that was a former residence of Peter Carl Faberge (famous for the eponymous eggs) and my father's Architectural and Construction Engineering college, where he earned a Bachelor's degree, were both located on the same street.)

Thus, I was born in Brooklyn, 338 years following the founding of The New Netherland settlement of Breuckelen in 1646, named after Breukelen in the Netherlands. Many avenues and streets bear Dutch names (Amsterdam Avenue in NYC, New Utrecht Avenue in Brooklyn, etc.) and this also holds for most of New York State. Growing up speaking English and Russian at home - two languages greatly influenced by the Nederlandse Taal - many common Dutch words were actually spoken. Herring and smoked Gouda cheese were culinary favorites. Reproductions of several paintings by Rembrandt (namely, the 'Jewish Bride' and 'Prodigal Son') and that of Frans Hals ('Portrait of an Officer') adorned the walls of both my grandparents homes. Throughout my childhood, during winter vacations, my parents would take me to Aruba, the Dutch Caribbean.

When I graduated summa cum laude (4.4/4.0) from High School with a standard diploma and an additional International Baccalaureate (IB) diploma, the Director of the IB program of my High School presented me with a Certificate of Achievement for earning straight 'A' marks in all subjects, every six week grading period during all four years of study. I was the only student able to do so in my graduating class of 2002, though that year our class had the second highest number of graduates with IB diplomas in all of North America. My higher level subjects were Physics, Mathematics, and English literature. I was also selected as a member of the National Honor Society, Spanish National Honor Society, and Mathematics Honor Society.

I received a scholastic scholarship to attend Rensselaer Polytechnic Institute (RPI) co-founded in 1824 in New York by Stephen van Rensselaer III, a descendant of an important Dutch family. The results of my IB exams and additional Advanced Placement and Scholastic Aptitude Test II exams enabled me to start university at the second year of

[3]Coney is derived from the Dutch word for 'rabbit' and also refers to 'hare'.

study. There are many Dutch traditions at RPI, the 'Dutchman's Shoes' football trophy, Dutch medieval graduation garments, as well as the scepter that the President of the University carries during important ceremonies. Following the first two years at RPI, I won the RPI-ETH scholarship to study Physics and Mathematics for two semesters at ETH, Zurich starting in Autumn 2004. The summer right before starting at ETH, Professor Ingrid Wilke most kindly worked with me at RPI and I was, thus, able to receive a research scholarship to work for three months as a research assistant in Professor Wilke's Terahertz laboratory, where Dr. Ricardo Ascázubi was my kind mentor.

In 2005, ETH was the center of the Centennial Celebrations of Einstein's Annus Mirabilis. It is during this occasion that many Nobel Prize Laureates, together with a Fields Medalist, most kindly autographed for me a large and beautiful poster-portrait of Einstein, resulting in an awesome signed document for future posterity to acknowledge, maybe in the next 100 years, that such a wonderful gathering of distinguished scientists had taken place at ETH. They were all very friendly, kind and even praised me for the idea.

Subsequently, I completed my fourth year at RPI, graduating in 2006 with a Master's degree in Applied Mathematics, a Bachelor's degree in Physics (cum laude), a Bachelor's degree in Pure Mathematics (cum laude), and a minor degree in German language, which may be a record of special achievement at RPI in the sciences. Knowledge of the German language would help me to understand the Dutch language at a faster pace. I was also inducted into the Sigma Pi Sigma National Physics Honor Society.

Professor Jürg Fröhlich of the ETH most kindly advised me on the excellent tradition of statistical mechanics in the Netherlands and I matriculated to Utrecht University in the year of the 400th anniversary of Rembrandt's birth. I received the Utrecht Excellence Scholarship and after two years of study earned a Master's degree in Theoretical Physics in 2008 with a thesis in the subject of String Theory/Quantum Gravity under the supervision of Professor Jan Ambjørn. The Academic building, where the graduation ceremony took place, was the site where the Union of Utrecht was signed on 23 January 1579.

During a gap year, visiting my parents and grandparents, I became interested in turbulence and in cosmic magnetic fields. Hence, I matriculated to the University of Cambridge in 2009 and was a member of St. Catharines College. I entered Part III of the Mathematical Tripos during the 800th anniversary celebrations of the university and earned the degree of Master of Advanced Study.

Following this, in August 2010, I commenced my PhD research at Leiden University under the supervision of Dr. Marijke Haverkorn. The results of this research comprise this thesis. (Historically, many of the US Pilgrim Fathers lived in Leiden and worked at Leiden University. John Quincy Adams, the 6th President of the US (1825 - 1829), studied at Leiden University during his father's[4] diplomatic mission to the the Netherlands.)

During my PhD, I attended conferences in the Netherlands, Germany (Bonn, Hamburg, Mainz, Munich - Ringberg Castle), Italy (Bologna), UK (Dublin, Newcastle upon Tyne) and also established an enduring close collaboration with Professor Anvar Shukurov and Dr. Andrew Fletcher, both of Newcastle University, UK. With the kind aid of Profes-

[4] John Adams, 2nd President of the US (1797 - 1801).

sor Anvar, my impromptu presentation at the DFG Research Unit 1254 Summer School 2011 at Ringberg Castle to address Professor Uli Klein's request for a proof of Cowling's anti-dynamo theorem, helped secure this collaboration which proved absolutely essential and, thus, during the second and third year of my PhD, I was a visiting researcher at Newcastle University for a total of over 3 months.

At the time of writing, I have accepted a position at the Diagnostic Image Analysis Group, a division of the Department of Radiology and Nuclear Medicine of Radboud University Medical Center.

And in August of this year, 2015, I did see a most beautiful display of real size Dutch wooden sail ships that, like a beautiful mirage, all appeared in Amsterdam - an event that takes place only once in 5 years. And standing there, I remembered a little boy, het dappere snijdertje, who has been dreaming of such a magical day...

"All grown-ups were once children - although few of them remember it" wrote Antoine de Saint-Exupéry. Being a snijder in 17th century Leiden was a very important profession. Would you wonder with me, how, 400 years later, this Carl Shneider van Brooklyn fairs in the 21st century...